Title
Engineering of Iron Gallium and Hafnium Oxide Interfaces for Magnetoelectric Applications

Author
Acosta, Adrian

Publication Date
2022

Peer reviewed|Thesis/dissertation

UNIVERSITY OF CALIFORNIA

Los Angeles

Engineering of Iron Gallium and Hafnium Oxide Interfaces for Magnetoelectric Applications

A dissertation submitted in partial satisfaction of the

requirements for the degree Doctor of Philosophy

in Chemical Engineering

by

Adrian Acosta

2022

ABSTRACT OF THE DISSERTATION

Engineering of Iron Gallium and Hafnium Oxide Interfaces

for Magnetoelectric Applications

by

Adrian Acosta

Doctor of Philosophy in Chemical Engineering

University of California, Los Angeles, 2022

Professor Jane Pei-Chen Chang, Chair

This work focuses on the engineering and tailoring the interfaces of both ferromagnetic multilayer films based on Iron Gallium (FeGa) as well as the surfaces of ferroelectric Hafnium Oxide (HfO_2) for applications toward magnetoelectric applications, which offer the promise of efficient control of magnetism at the nanoscale. In this work, two key materials challenges of the respective ferromagnetic and ferroelectric materials toward integration in composite magnetoelectric devices are discussed: development of ferromagnetic materials with strong magnetomechanical coupling and ferroelectric materials with robust ferroelectric properties at the nanoscale. First, while FeGa is a well-known magnetostrictive material that could be a candidate for integration for strain-mediated magnetoelectric devices, the challenge remains that it is lossy at high frequencies. On the other hand, while ferroelectric HfO_2 has gained interest due to its emergent and ferroelectricity at the nanoscale that circumvents traditional limitations of

ferroelectric materials and is CMOS compatible, it remains a challenge to fully understand how to stabilize the ferroelectric phase.

To address the former, this work investigated how the influence of an underlayer and a multilayering structure can be used to enhance the soft magnetic properties of FeGa films. It was found that a NiFe underlayer serves to influence the microstructure of the FeGa films, resulting in a smaller grain size and enhanced texture, which yielded a smaller coercivity while retaining a strong magnetostriction. It was also observed that the saturation magnetostriction is maintained for the FeGa films. Furthermore, a multilayering strategy that uses NiFe as an interlayer to form FeGa/NiFe bilayers was investigated to achieve a composite with a further decrease in coercivity and lower high frequency losses – specifically for a multilayer consisting of ten bilayers of FeGa (10 nm) / NiFe (2.5 nm). Additionally, the multilayering strategy combined with an insulating interlayer was shown to be a useful strategy to achieve a composite with an even lower coercivity meets the necessary criteria of magnetic softness and low loss necessary for integration in magnetoelastic and high frequency antenna devices.

To address the latter, density functional theory was used to understand the relationship between the ferroelectric polarization and the surface composition to stabilize the orthorhombic ferroelectric phase of HfO_2. It was found that the surface composition plays a critical role in the ferroelectric stability of orthorhombic HfO_2 thin films, which can enable stable polarization without a critical thickness limit under an open-circuit boundary condition. It was found that a relatively oxygen-rich positively polarized surface can effectively screen the polarization to stabilize the orthorhombic phase. In contrast, stoichiometric HfO_2 surfaces that cannot screen the polarization lead to an ionic depolarization towards a nonpolar monoclinic phase. This highlights the importance of controlling the surface composition for the stability of ferroelectricity in HfO_2

and points towards control of the surface composition as a mechanism for optimizing the ferroelectric performance of HfO_2-based thin films.

This work provided two routes for the development and engineering of ferromagnetic and ferroelectric materials that can overcome key material challenges for the integration toward magnetoelectric devices with robust and efficient performance.

The dissertation of Adrian Acosta is approved.

Gregory P. Carman

Samanvaya Srivastava

Dante A. Simonetti

Jane Pei-Chen Chang, Committee Chair

University of California, Los Angeles

2022

TABLE OF CONTENTS

Chapter 1 Introduction 1

1.1 Motivation 1

1.2 Magnetoelectric Coupling 2

1.3 Material Challenges for Magnetoelectric Devices at the Nanoscale 6

1.4 Scope and Organization 17

Chapter 2 Experimental and Computational Methods 19

2.1 Experimental Methods 19

2.2 Superconducting Quantum Interference Device (SQUID) Magnetometry 26

2.3 Stripline Permeability Measurement 29

2.4 Computational Methods 37

2.5 Summary 45

Chapter 3 Underlayer Effect on the Soft Magnetic Properties of FeGa Thin Films 46

3.1 Effect of underlayers on the static magnetic properties of FeGa thin films 46

3.2 Effect of underlayers on the microstructure of FeGa thin films 50

3.3 Magnetoelastic properties of FeGa thin films with NiFe and Cu underlayers 55

3.4 Summary 56

Chapter 4 Process development of FeGa/NiFe multilayer composite 57

4.1 Influence of Multilayering on Magnetic Hysteresis 58

4.2 First order reversal curves 60

4.3 Influence of Multilayering on High Frequency Properties 64

4.4 Summary and Outlook 70

Chapter 5 Influence of the ferroelectric polarization on the stability of HfO_2 surfaces 71

5.1 Surface structures of HfO_2 models 71
5.2 Surface energies 77
5.3 Surface bader charges 82
5.4 Interpreting surface stability via electrostatic potential and projected DOS profiles 85
5.5 Summary & outlook 91
Chapter 6 Effect of the surface composition and thickness on the stability of ferroelectric polarization in HfO_2 thin films 93
6.1 Influence of composition on the ferroelectric stability of HfO_2 slabs 94
6.2 Influence of thickness on the ferroelectric polarization of HfO_2 slabs 101
6.3 Extending results to $Hf_{0.5}Zr_{0.5}O_2$ 107
6.4 Summary & outlook 114
Chapter 7 Summary 115
Appendices 117
Bibliography 137

LIST OF FIGURES

Figure 1.1 Number of publications on multiferroics or magnetoelectricity per year. Sourced from: http://webofknowledge.com, October 24, 2021. 2

Figure 1.2 Venn diagram showing the relation between different magnetically and electrically polarizable materials. Adapted from: *(Eerenstein 2006).* 3

Figure 1.3 Examples of macroscopic magnetic properties that can be manipulated by via the converse ME effect. Adapted from: *(Song 2017)* 4

Figure 1.4 Examples of dielectric materials that have been used to interface with ferromagnetic materials to form a magnetoelectric composite. The solid shapes indicate the type of coupling mechanism possible for each type of interface. Adapted from: (Chu 2018). 5

Figure 1.5 Schematics explaining both the mechanisms of magnetoelectric coupling and examples of possible magnetoelectric response enabled through modulation of (a) spin-polarized electron densities, (b) strain, and (c) exchange coupling. Adapted from: (Chu 2018) and (Vaz 2012). 6

Figure 1.6: Plot of saturation magnetostriction versus coercivity for the ferromagnetic thin films listed in Table 1.2. The dashed line is a linear fit to the materials plotted with a solid square. ... 11

Figure 1.7: Schematic illustrating thickness dependence of the polarization (P) and depolarizing field (D) have a thickness dependence, resulting in the minor influence of the depolarizing field on polarization in the high thickness range and a suppression of polarization at low thicknesses. Adapted from *(Nordlander 2018).* 14

Figure 1.8: Schematic illustration of different types of ferroic domain walls. (a) Ising type, showing a gradual magnitude variation but no rotation of the order parameter. (b) Bloch type, showing a gradual rotation, and no change in magnitude. (c) Néel type, showing an in-plane rotation and no change in magnitude. (d) Mixed Ising-Néel type, showing both in-plane rotation and decrease of the magnitude. A mixed Ising-Bloch type would be similar, with an out-of-plane rotation. Adapted from (Lee 2009). 15

Figure 1.9: (a) Atomic structure of the thinnest domain for $PbTiO_3$ and variation of the polarization along the direction perpendicular to the domain walls. (b) Energy along the path of polarization switching of $PbTiO_3$ starting from a uniformly polarized structure. Adapted from (Lee 2020). . 16

Figure 1.10: (a) Atomic structure of the thinnest domain for HfO_2 and variation of the polarization along the direction perpendicular to the domain walls. (b) Energy along the path of polarization switching of HfO_2 starting from a uniformly polarized structure. Adapted from (Lee 2020). 16

Figure 2.1: Schematic of a sputtering deposition chamber used to deposit films on a substrate by bombardment of a target by ionized gas. 20

Figure 2.2: Schematic of the working principle of XPS. 22

Figure 2.3: XPS survey scan of a $Fe_{75}Ga_{25}$ film grown on a Si substrate. Major peaks are identified. 23

Figure 2.4: (left) Individual XPS spectra of Fe 2p and Ga 2p regions. (right) Binding energies and RSF values for Fe 2p, Ga 2p photoelectrons used to calculate the relative stoichiometry. 23

Figure 2.5: Schematic of the working principle of XRD. 24

Figure 2.6: XRD spectra of a 100 nm FeGa film grown on a Silicon substrate. 26

Figure 2.7: Schematic of the working principle of a SQUID magnetometer. 27

Figure 2.8: (left) Magnetic hysteresis loop obtained for a sputter deposited 100 nm FeGa thin film. (right) Values of the main properties of interest highlighted on the plot on the left panel. 29

Figure 2.9: Schematic of the stripline set-up used to measure RF absorption of ferromagnetic thin films. 29

Figure 2.10: (a) Schematic depicting the placement of the stripline housing from Figure 2.9 between two Helmholtz coils with a feedthrough of the microwave coaxial cable coming from the vector network analyzer shown in (b). A picture of the actual stripline housing used is shown in (c). 30

Figure 2.11: Raw uncorrected data for S_{11} absorption parameter of a 100 nm FeGa film on a 2.5 nm NiFe underlayer on a Si substate. 31

Figure 2.12: S_{11} absorption parameter with background subtracted from Figure 2.9. 31

Figure 2.13: Cross section of the absorption as a function of the magnetic field from Figure 2.11 at a frequency of 9.6 GHz. Arrows depict measurement of FWHM. 32

Figure 2.14: Schematic of the set-up used to measure the cantilever deflection and the relative directions of the constant saturating bias field and perpendicular AC magnetic field during the measurement. 33

Figure 2.15: Measured deflection and calculated stress and magnetostriction as a function of magnetic field for 100 nm FeGa sputtered directly on Si using the set-up shown in Figure 2.14.34

Figure 2.16: Schematic illustration of the strategy of using a thin underlayer as a buffer between an FeGa film and the underlying substrate. 35

Figure 2.17: Schematic of multilayering approach that builds on the underlayer effect. The cumulative thickness of the FeGa film in the structure is kept constant at 100 nm and additional 2.5 nm interlayers are inserted through the thickness of the films. The label above each multilayer structure corresponds to the total number of bilayer pairs. 36

Figure 2.18: Schematic of the strategy to add insulating interlayers of Al_2O_3 (2.5 nm thickness) after each FeGa/NiFe bilayer. The case of a 10 FeGa/NiFe bilayer sample is shown. 36

Figure 2.19: Structure of the bulk four-formula-unit supercell of (a) the nonpolar tetragonal ($P4_2/nmc$) phase and (b) the polar orthorhombic ($Pca2_1$) HfO_2 phase. The polarization vector is along the c axis [001] direction, as indicated by the overlaid arrow. Hf and O atoms are shown as green (large) and red (small) spheres, respectively. Total energy for the bulk four-formula-unit orthorhombic HfO_2 structure as a function of the (b) *k*-point density in a Monkhorst-Pack grid using a 1000 eV planewave kinetic energy cutoff and (c) the planewave kinetic energy cutoff using a 10x10x10 *k*-point density in a Monkhorst-Pack grid. The total energy convergences are both ~0.01 meV/atom for the 4×4×4 relative to the 10×10×10 *k*-point mesh and for the 800 eV relative to the 1000 eV kinetic energy cutoff. 39

Figure 2.20: Profile view of nonpolar tetragonal (left) and polar orthorhombic (right) slab models consisting of 9 layers constructed from the bulk phases shown in Figure 2.19(a) and (b). P+ and P- labels denote the directions of polarization for the polar slab. Green atoms: Hf, red atoms: O. 40

Figure 2.21: (a) Top and bottom surface views of the unrelaxed nonpolar tetragonal 2.0-O/2.0-O slab, profile is rotated compared to the same slab in Figure 2.19(a). (b) top and bottom surface views of the unrelaxed polar orthorhombic 2.0-O/2.0-O slab, profile is rotated compared to the same slab in Figure 2.19(b). The nomenclature refers to the composition of the surface termination per surface-formula-unit. Legend (right) is used to show the perimeter of a single surface cell. Outermost atoms are circled in (a) and (b) as noted in the legend. 41

Figure 3.1: Normalized in-plane magnetic hysteresis loops of 100 nm FeGa sputtered on a Si substrate with different underlayer materials. 47

Figure 3.2: FMR absorption spectra as a function of both frequency (100 MHz - 6 GHz) and magnetic bias (0 - 600 Oe) for 100 nm FeGa sputtered on the following: (a) Si only, (b) Si + 2.5 nm Ta underlayer, (c) 2.5 nm Cu underlayer, (d) Si + 2.5 nm NiFe underlayer. 49

Figure 3.3: FMR absorption spectra as a function of magnetic bias field at 6 GHz for 100-nm FeGa films sputtered on a 2.5 nm underlayer of different materials (Ta, ... 50

Figure 3.4: XRD spectra of the main bcc (110) FeGa peak when grown on different underlayer materials. Solid lines are the best Voigt fit of the data in circles. Vertical dashed lines are used to highlight the shift in the (110) peak across samples. 52

Figure 3.5: XRD spectra of a Si substrate alone and the following films (~100 nm thickness) on Si: Ta, Cu, NiFe, FeGa. Highlighted area is used to show close lattice match of main Cu & NiFe diffraction peaks to FeGa. 53

Figure 3.6: AFM of ~100 nm FeGa films grown (a) directly on Si, (b) with a 2.5 nm Ta underlayer, (c) with a 2.5 nm Cu underlayer, (d) with a 2.5 nm NiFe underlayer 54

Figure 3.7: (Left axis) Cantilever deflection calculated for ~100 nm FeGa sputtered directly on Si and on NiFe and Cu underlayers as a function of the AC magnetic field (along the short axis of cantilever sample). (Right axis: b) Stress calculated from the cantilever deflection. An initial bias field of 100 Oe was applied to saturate the magnetization along the long axis of the cantilever sample and held constant during the measurement. (Right axis: λ) Stress calculated from the

cantilever deflection. An initial bias field of 100 Oe was applied to saturate the magnetization along the long axis of the cantilever sample and held constant during the measurement. 55

Figure 4.1: Normalized in-plane magnetic hysteresis loops comparing a single FeGa film (N=0) to multilayer FeGa/NiFe samples (N=1, 2, 4, 10). N refers to the total number of FeGa/NiFe bilayers, where the total volume of FeGa remains constant and the thickness of the individual NiFe layers is fixed at 2.5 nm..... 59

Figure 4.2: Normalized in-plane magnetic hysteresis loops comparing a 10 bilayer stack of FeGa/NiFe before and after the addition of a thin 2.5 nm Al_2O_3 interlayer insertion in each bilayer. N = 10 refers to the same sample in Figure 4.1 consisting of a stack of 10 bilayers of (10 nm FeGa/ 2.5 nm NiFe). N = 10 + Al_2O_3 refers to the multilayer stack consisting of 10 trilayers of (10 nm FeGa/ 2.5 nm NiFe/ 2.5 nm Al_2O_3)..... 60

Figure 4.3: A set of FORC curves for a 100 nm FeGa film grown directly on a Si substrate..... 61

Figure 4.4: A set of FORC curves for a 10 bilayer multilayer film stack of (10 nm FeGa)/(2.5 nm NiFe) on a Si substrate..... 62

Figure 4.5: FORC diagram for the 100 nm FeGa film grown directly on a Si substrate shown in Figure 4.3. 63

Figure 4.6: FORC diagram for a 10 bilayer multilayer film stack of (10 nm FeGa)/(2.5 nm NiFe) on a Si substrate. 64

Figure 4.7: FMR spectra as a function of both frequency (100 MHz – 20 GHz) and magnetic bias (0 – 1200 Oe) for a single FeGa film (N=0) and multilayer FeGa/NiFe samples (N = 1, 2, 4, 10). 65

Figure 4.8: FMR linewidth as a function of frequency for a single FeGa film (N=0) and multilayer FeGa/NiFe samples (N = 1, 2, 4, 10) shown in Figure 4.7. Linear fit is shown as a dashed line. 67

Figure 4.9: (left) FMR spectra as a function of both frequency (100 MHz – 20 GHz) and magnetic bias (0 – 1200 Oe) for a 10 trilayer stack of (10 nm FeGa/ 2.5 nm NiFe/ 2.5 nm Al_2O_3). (right) cross section of FMR absorption at 9 GHz..... 68

Figure 4.10: FMR linewidth as a function of frequency for the N = 10 multilayer sample in Figure 4.7 and the 10 bilayer stack of FeGa/NiFe/Al_2O_3 (N = 10 + Al_2O_3) in Figure 4.9. Linear fit is shown as a dashed line..... 69

Figure 5.1: Relaxed structures for compositionally (a) symmetric and (b) asymmetric nonpolar tetragonal HfO_2 supercell slabs. Profile views are shown only for the most stable compositionally symmetric and asymmetric slabs among all compositions studied. Top and bottom views of the slabs are shown for the most stable configuration for a given composition. The composition of the outermost layers in terms of atoms per surface unit cell is labeled for the top and bottom layer above each structure. The fainter atoms are farther away from the viewer. Outermost atoms are circled within a 1 × 1 lateral unit cell that contains 2 f.u. (purple-dashed box) 75

Figure 5.2: Relaxed structures for most stable compositionally (a) symmetric and (b) asymmetric orthorhombic HfO_2 supercell slabs. Profile views are shown only for the most stable compositionally symmetric and asymmetric slabs among all compositions studied. Top and bottom views of the slabs are shown for the most stable configuration for a given composition. The composition of the outermost layers in terms of atoms per surface unit cell is labeled for the top (P+) and bottom (P−) layer above each structure. To disambiguate the nomenclature for the compositionally asymmetric slabs, we use P+ and P− to refer to the composition of the positively and negatively polarized surfaces, respectively. The fainter atoms are farther away from the viewer. Outermost atoms are circled within a 1 × 1 lateral unit cell that contains 2 f.u. (purple-dashed box). 76

Figure 5.3: Plot of surface energy as a function of (a) temperature from 100 to 1100 K and (b) pressure from 10^{-12} to 10^{2} bar for compositionally symmetric and asymmetric tetragonal HfO_2(110) slabs. 81

Figure 5.4: Plot of surface energy as a function of (a) temperature from 100 to 1100 K and (b) pressure from 10^{-12} to 10^{2} bar for compositionally symmetric and asymmetric orthorhombic HfO_2(001) slabs. To disambiguate the nomenclature for the compositionally asymmetric slabs, we use P+ and P− to refer to the composition of the positively and negatively polarized surfaces, respectively. 81

Figure 5.5: Layer-by-layer Bader charge deviation for (a) nonpolar tetragonal and (b) polar orthorhombic HfO_2 slabs for three different compositions. The values correspond to the average Bader charge deviation per atom for each Hf and O half-layer relative to their respective bulk phase. Note that the left- and right-hand sides of the plots correspond respectively to the bottom and the top of the slabs. In the surface nomenclature, the composition of the top surface is given first. 84

Figure 5.6: Plane-averaged electrostatic potential comprised of the ionic and Hartree potentials (blue) and the z-averaged potential (red), calculated along the surface normal for the tetragonal(110) surface with (a) symmetric 1.0-O/1.0-O composition and orthorhombic(001) surfaces with (b) symmetric 1.0-O/1.0-O, (c) symmetric 1.5-O/1.5-O, and (d) asymmetric P+:1.5-O/P−:1.0-O compositions. The potentials are referenced to the Fermi level. The horizontal dashed lines mark the positions of the vacuum level for each surface. The difference in the work functions ($\Delta\Phi$) is the difference in the vacuum potentials of the two surfaces multiplied by a unit of elementary charge e = 1. Note that the left- and right-hand sides of the plots respectively correspond to the bottom and the top of the slabs. In the surface nomenclature, the composition of the top surface is given first. 86

Figure 5.7: Layer-by-layer projected densities of states (pDOS) for the tetragonal HfO2(110) surface with (a) symmetric 1.0-O/1.0-O composition and orthorhombic (001) surfaces with (b) symmetric 1.0-O/1.0-O, (c) symmetric 1.5-O/1.5-O, and (d) asymmetric P+:1.5-O/P−:1.0-O compositions. The electronic energies reference to the valence-band edge or the Fermi level (dashed vertical lines mark Energy = 0 eV). The top O layer of the polar orthorhombic slab corresponds to the P+ surface and the bottom O layer corresponds to the P− surface. Hf half-layer spin up/down: green/light green; O half-layer spin up/down: red/pink. The values are shifted so

that the pDOS of the top and bottom layers correspond respectively to the top-most and bottom-most curves 88

Figure 6.1: Profile view (after ionic relaxation) of 11-Hf-half-layer thick HfO_2 supercell slabs constructed with symmetric (1.0-O/1.0-O) or asymmetric (P+:1.5-O/P−:1.0-O) surface terminations. Green spheres are Hf whereas red spheres are O. 97

Figure 6.2: (a) Optimized atomic structure of bulk monoclinic ($P2_1/c$) phase looking down the [001] and [010] axis (left and right, respectively). The optimized lattice parameters are a = 5.148 Å, b = 5.198 Å, c = 5.331 Å, α = 90.00°, β = 99.70°, γ = 90.00°. The parameters are close to the experimental values, namely, a = 5.12 Å, b = 5.17 Å, c = 5.29 Å, α = 90.0°, β = 99.1°, γ = 90.0°. (b) Two profile views (after ionic relaxation) of the symmetric (1.0-O/1.0-O) 11-Hf-half-layer thick HfO_2 supercell slab. Green spheres are Hf whereas red spheres are O. Compare the similarity of the two profiles (rotated by 90° about the c-axis) to that of the bulk monoclinic phase in (a). Note that an orthorhombic-like layer exists at the phase boundary between monoclinic-like units [outlined in the left panel of Figure 6.1] and is present in symmetric slabs with odd number of Hf layers that cannot accommodate a full monoclinic unit cell. (c) Plots of the interlayer distances of each Hf half-layer to the next (left) and intralayer distances between the two O planes within each O half-layer (right) as illustrated in (b) along the direction of the surface normal for the symmetric (1.0-O/1.0-O) 11-Hf-half-layer thick HfO_2 supercell slab. The N^{th} half layer begins at the bottom of the slab. Dashed purple and orange lines show the values from the bulk monoclinic phase in (a) for reference. 99

Figure 6.3: (a) Interlayer spacing from one Hf half-layer to the next for asymmetrically terminated slabs along the direction of the surface normal. The N^{th} Hf half-layer begins at the bottom P− surface of the slab as illustrated in Figure 6.1. Dashed purple line shows the bulk value for reference. (b) Intralayer spacing between O planes within each O half-layer for asymmetrically terminated slabs along the direction of the surface normal. Each O half-layer is partitioned into two O planes of two O atoms each and we use the distance of the average z-coordinate of the two O in each plane. Illustration of the measure for this displacement is shown via dashed lines for N = 1 and N = 2 in part (a) of Figure 6.1. Dashed purple line shows the bulk value for reference. 100

Figure 6.4: Planar-averaged electrostatic potential and planar-integrated electron density (bottom panel) for (a) symmetrically and (b) asymmetrically terminated slabs along the direction of the surface normal, before and after ionic relaxation. The z-coordinate tracks the distance from the middle of the vacuum to the bottom of the slab (P−) surface to the top of the slab (P+) surface and back to the middle of the vacuum. The potentials in the top panels reference to the Fermi level. 100

Figure 6.5: (a) Displacement between the two O planes within each O half-layer for asymmetrically terminated polar orthorhombic HfO_2 slabs, $\Delta z_{O,N}$, with varying thickness along the direction of the surface normal [see Figure 6.1(a) for the definition of $\Delta z_{O,N}$]. Dashed purple line shows the bulk value for reference. (b) Average value of the polar displacements of O across the slabs plotted in (a). Dashed purple line provides a comparison to the bulk polar displacement. Inset figures show profile view of 11- and seven-Hf-layer thick slabs (green spheres are Hf whereas red spheres are O). At three Hf layers (labeled “critical thickness”) the asymmetric HfO_2 structure.

Consequently, we do not plot its average O displacement. In its place, the average polar displacement is plotted for the symmetric slab (whose orthorhombic phase is stable at a three-Hf-layer thickness). 102

Figure 6.6: Net electrostatic potential as measured by the difference in flat electrostatic potential in the vacuum region of the P− and P+ surfaces as a function of total slab thickness for symmetrically and asymmetrically terminated orthorhombic HfO_2 slabs, before (dark cyan) and after (pink) ionic relaxation. 104

Figure 6.7: Three Hf layer optimized structures for the asymmetric (left) and asymmetric (right) HfO_2 slab structures. 106

Figure 6.8: Layer-by-layer projected densities of states (pDOS) for a three-Hf-half-layer thick HfO_2 supercell slab with a symmetric (1.0-O/1.0-O) surface composition (a) before and (b) after ionic relaxation. The electronic energies are referenced to the Fermi level (dashed vertical lines denote Energy = 0 eV). The top O layer of the polar orthorhombic slab corresponds to the P+ surface and the bottom O layer corresponds to the P− surface. Hf half-layer spin up/down: green/light green; O half-layer spin up/down: red/pink. The values on the vertical axes are shifted so that the pDOS of the top and bottom layers correspond to the top-most and bottom-most curves 106

Figure 6.9: Profile views that highlight the resemblance of (a) a supercell of the asymmetric three-Hf-half-layer thick HfO_2 slab shown in Figure 6.1 and (b) the bulk rhombohedral (*R*3) phase of HfO_2 looking down the [010] axis. Green spheres: Hf, red spheres: O. The predicted lattice parameters of the *R*3 phase shown in (b) are $a = b = 7.19$ Å, $c = 9.106$ Å and $\alpha = \beta = 90.0°$, $\gamma = 120.0°$. 107

Figure 6.10: (a) Profile views of the relaxed structures for orthorhombic $Hf_{0.5}Zr_{0.5}O_2$ supercell slabs. The composition of the outermost layers in terms of atoms per surface unit cell is labeled for the top and bottom layer above each structure. The middle three Hf/Zr and two O half-layers for all slabs are fixed to their bulk-like arrangement with the polarization direction normal to the surface as labeled. The fainter atoms are farther away from the viewer. Plots of the surface energy as a function of (b) temperature from 100 to 1100 K and (c) pressure from 10^{-12} to 10^{2} bar corresponding to the slabs in (a). See SM for the bulk optimized orthorhombic structure of $Hf_{0.5}Zr_{0.5}O_2$ 109

Figure 6.11: (a) Average value of the polar displacements of O for $Hf_{0.5}Zr_{0.5}O_2$ (a). Dashed purple line provides a comparison to the bulk polar displacement. Inset figures show profile view of 11- and seven-layer thick slabs (green spheres are Hf, dark cyan spheres are Zr, and red spheres are O). At three layers (labeled “critical thickness”) the asymmetric $Hf_{0.5}Zr_{0.5}O_2$ structure (shown in bottom panel (b)) deviates significantly from the bulk orthorhombic phase. Thus, as for the case of $Hf_{0.5}Zr_{0.5}O_2$, we do not plot its average O displacement. In its place, the average polar displacement is plotted for the symmetric slab (top panel (b)). Three-layer optimized structures for the symmetric (top panel) and asymmetric (bottom panel) $Hf_{0.5}Zr_{0.5}O_2$ slab structures. 111

LIST OF TABLES

Table 1.1 Classification of ME devices. Adapted from *(Cheng 2018)*..... 7

Table 1.2: Properties of select ferromagnetic materials. Where available, data for thin film material properties is used..... 9

Table 1.3: Summary of recent studies on FeGa/NiFe ferromagnetic composites 12

Table 1.4: A comparison of the most common ferroelectric thin film materials to HfO_2-based ferroelectrics. Adapted from (Mikolajick 2021)..... 13

Table 1.5: Summary of recent studies on ME composites that incorporate a HfO_2-based ferroelectric for the voltage control of magnetism. 17

Table 2.1: Sputter deposition parameters for the targets used to deposit the various thin films sputter deposited in this work. An ULVAC JSP 8000 sputter system with a base pressure of 2×10^{-7} Torr at room temperature was used for the depositions in this work..... 21

Table 2.2: Constants in the Shomate equations used to evaluate the enthalpy (H) and entropy (S) of O_2 over various temperature ranges. These constants correspond to units of kJ/mol and J/K-mol for H and S, respectively, using the equations in the main text, where T is in K..... 44

The effective Gilbert damping coefficient, α_{eff}, was calculated by fitting the FMR linewidth of the absorption as a function of frequency for the entire FMR spectra in Figure 3.2 as described in Chapter 2. The values are listed in Table 3.1. The FeGa films deposited with Cu and NiFe underlayers show a significant decrease (∼75%–78%) in their effective Gilbert damping coefficient compared to an FeGa film without an underlayer. 48

Table 3.2: Table Summary of in-plane coercivity, normalized remnant magnetization (M_r/M_s), Gilbert damping coefficient (α), relative change in 110 peak intensity *(*ΔI_{110}), and average grain width (D) for 100-nm FeGa grown on different underlayer materials on a Si substrate. 54

sssTable 4.1: Summary of the gilbert damping coefficient and inhomogeneous linewidth extracted from Figure 4.8 and Figure 4.10. Error bars represent 1 standard deviation to the linear fit parameters. 69

ACKNOWLEDGEMENTS

This one goes out to my family that has sacrificed and supported me throughout my entire education.

To Yissel who has been by my side.

To the blend of friends, colleagues, and collaborators. Gary – it has been a pleasure working alongside you and I wish you the absolute best in your future career. Taylor, Brian, Coco, and Owen – you are all brilliant and I have no doubt you will do great the rest of your time at UCLA. Eric, Roxanne, and Abdullah – it's been real from day one, we're all going to make it. To everyone in TANMS, from the leadership to the students – it has been a very unique team to be a part of. To Prof. Carter and Mark, it has been wonderful working with your group and doing good science.

Lastly, this work would not be possible without the immense support and guidance from my advisor, Prof. Chang. She has instilled a strong work ethic to always take great care in everything I do.

VITA

2017-2022	Graduate Student Research Department of Chemical & Biomolecular Engineering University of California, Los Angeles Los Angeles, CA
2017	B.S., Chemical Engineering The University of Arizona Tucson, AZ

AWARDS

2020	UCLA Graduate Council Diversity Fellowship
2017	TANMS Engineering Research Center Doctoral Fellow

PUBLICATIONS AND PRESENTATIONS

Acosta, A., Martirez, J. Mark, Lim, N., Chang, J. P., Carter, E. A., 2021. Relationship between ferroelectric polarization and stoichiometry of HfO_2 surfaces. *Phys. Rev. Mater.*, *5*(12), p.124417.

Guevara De Jesus, M., Xiao, Z., Goiriena-Goikoetxea, M., Chopdekar, R.V., Panduranga, M., Shirazi, P., Acosta, A., Chang, J. P., Bokor, J., Carman, G. P., Candler, R., Lynch, C., 2021. Magnetic State Switching in FeGa Microstructures. *Smart Mater. Struct.*, *31*(3), p.035005.

Acosta, A., Fitzell, K., Schneider, J.D., Dong, C., Yao, Z., Sheil, R., Wang, Y.E., Carman, G.P., Sun, N.X. and Chang, J.P., 2020. Underlayer effect on the soft magnetic, high frequency, and magnetostrictive properties of FeGa thin films. *J. Appl. Phys.*, 128(1), p.013903.

Acosta, A., Fitzell, K., Schneider, J.D., Dong, C., Yao, Z., Wang, Y.E., Carman, G.P., Sun, N.X. and Chang, J.P., 2020. Enhancing the soft magnetic properties of FeGa with a non-magnetic underlayer for microwave applications. *Appl. Phys. Lett.*, *116*(22), p.222404.

Acosta, A., Martirez, J.M.P., Lim, N., Chang, J.P., Carter, E.A., Influence of Thickness and Surface Composition on the Stability of Ferroelectric Polarization in Ultrathin HfO_2 in 2022 MRS Spring Meeting, Honolulu, HI, 2022.

Acosta, A., Chang, J.P., Optimizing magneto-elastic coupling in multilayer FeGa and NiFe thin films for magnetoelectric applications in AVS 68th International Symposium, Oct 2021.

Acosta, A., Fitzell, K., Dong, C., Zurbuchen, M., Sun, N.X. and Chang, J.P., Effect of Interlayer and Underlayers on the Microstructure and Magnetic Softness in FeGa-based Ferromagnetic Composites in AVS 66th International Symposium, Columbus, OH, 2019.

Chang, J., Acosta, A., and Chang, J.P., Multiferroic Integration of Undoped Ferroelectric HfO_2 and Ferrimagnetic $CoFe_2O_4$ Thin films by Radical-Enhanced Atomic Layer Deposition in AVS 65th International Symposium, Long Beach, CA, 2018.

Chapter 1 Introduction

Magnetoelectric materials and devices offer the prospect of a leap in enhancement in the control of magnetism. The background on the magnetoelectric effect is first reviewed with a focus on composite magnetoelectric materials. Two key challenges for materials toward integration in magnetoelectric composite materials and devices are discussed: development of ferromagnetic materials with strong magnetomechanical coupling and ferroelectric materials with robust ferroelectric properties at the nanoscale.

1.1 Motivation

Magnetoelectricity – a characteristic of materials that exhibit a coupling between their electric and magnetic properties – has drawn increasing attention over the last several decades. By circumventing traditional methods of controlling magnetic and electric polarization at the micro- and nanoscale, magnetoelectric materials offer the potential to allow next-generation electronic devices to meet the size and energy demands of society. For example, it has been estimated that in the rising era of the internet of things (IoT), the annual production of sensors will inevitably exceed one trillion as soon as the next decade posing major problems will arise in terms of environmental, resource, and labor costs (Bogue 2014).

The recent rise in theoretical and experimental investigations in the field of magnetoelectric materials, driven by both the demand for better performance and need to understand the mechanisms involved, can be seen in the increasing number of publications on multiferroics and magnetoelectricity as shown in Figure 1.1.

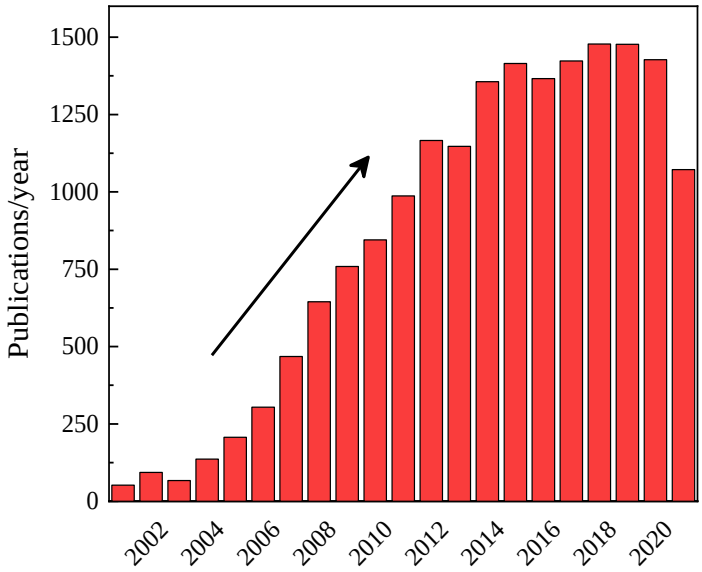

Figure 1.1 Number of publications on multiferroics or magnetoelectricity per year. Sourced from: http://webofknowledge.com, October 24, 2021.

The focus of this chapter is to introduce the origins and descriptions of magnetoelectric phenomena and highlight the material development and needs for magnetoelectric devices.

1.2 Magnetoelectric Coupling

Magnetoelectric materials lie at the intersection of materials that are both magnetically and electrically polarizable. While nearly all materials are observed to exhibit a magnetic or electric response, only a smaller subset can have a net magnetic or electric polarization, and an even smaller subset exhibit a coupling between both their magnetic and electric orderings. The subset of multiferroic magnetoelectric materials is of particular interest due to their spontaneous reversible and non-volatile electrical and magnetic polarization. This relationship is summarized in Figure 1.2.

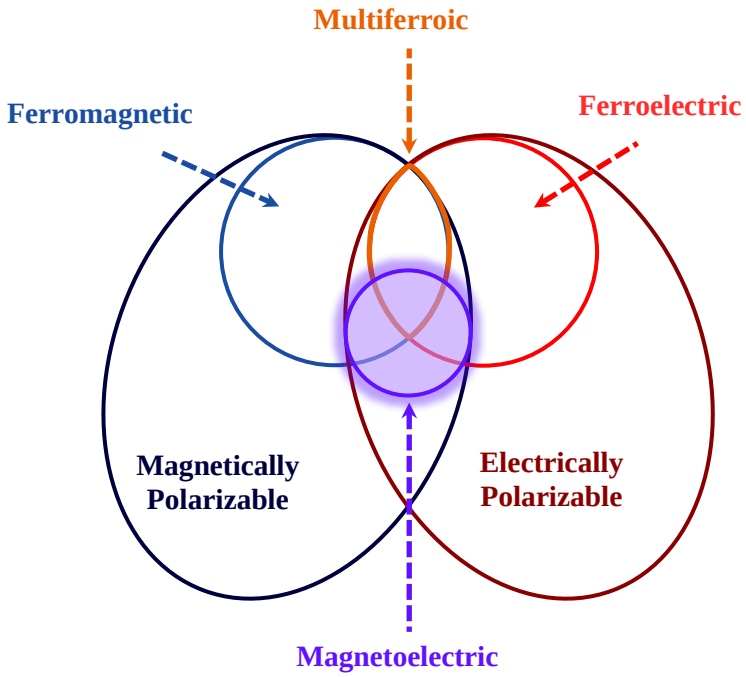

Figure 1.2 Venn diagram showing the relation between different magnetically and electrically polarizable materials. Adapted from: *(Eerenstein, Mathur et al. 2006)*.

For a single phase magnetoelectric material, beyond just the electric susceptibility (χ^e) and magnetic susceptibility (χ^v) that describe the respective electrical (P) and magnetic (M) polarization response to an electric or magnetic field, the linear magnetoelectric susceptibility (α_{ij}) describes a linear response of the electric polarization to a magnetic field, and vice versa (Fiebig 2005) as follows:

$$P_i(\vec{E},\vec{H}) = P_i^S + \epsilon_0\chi_{ij}^e E_j + \alpha_{ij}H_j + \frac{1}{2}\beta_{ijk}H_jH_k + \gamma_{ijk}H_iE_j + \cdots$$

$$M_i(\vec{E},\vec{H}) = M_i^S + \mu_0\chi_{ij}^e H_j + \alpha_{ij}E_i + \beta_{ijk}E_iH_j + \frac{1}{2}\gamma_{ijk}E_jE_k + \cdots$$

The spontaneous polarization is given by P^S and M^S. The higher order magnetoelectric effects are denoted by the coefficients, β_{ijk} and γ_{ijk}, but are typically ignored when referencing the magnetoelectric effect (ME) as most of the research is usually focused on the linear ME response.

There are many different macroscopic properties that can be modulated with the application of a magnetic field in the direct ME effect and vice versa for the converse ME effect. Several examples are shown in Figure 1.3 for the case of the converse magnetoelectric effect which include modulation of magnetization (M_s), coercivity (H_c), magnetic anisotropy, exchange bias field, and magnetoresistance.

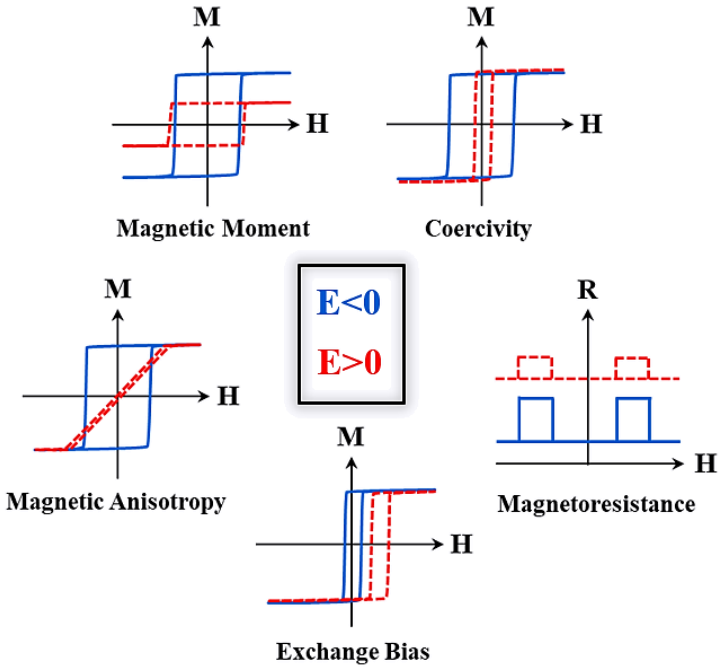

Figure 1.3 Examples of macroscopic magnetic properties that can be manipulated by via the converse ME effect. Adapted from: *(Song, Cui et al. 2017)*

It remains a challenge to develop single-phase magnetoelectric materials with strong large magnetic/electrical polarization and a strong magnetoelectric coupling between them at room temperature. As an alternative, composites combining both materials with both magnetic/electrically polarizable materials have been investigated and provide excellent routes for developing strongly magnetoelectric materials (Wang, Hu et al. 2010).

In general, magnetoelectric coupling in composites and heterostructures relies on the interplay among the spin, orbit, charge, and lattice degrees of freedom across the interface rather

within one crystal lattice. This is highlighted in Figure 1.4. The direct ME effect in heterostructures has so far only been observed to occur through one single mechanism: magnetic-field-induced strain is transferred to a piezoelectric layer across the interface, and then such strain modulates the electric polarization through the piezoelectric coupling. In contrast, the converse magnetoelectric coupling can occur through multiple mechanisms (indicated by the solid ellipses in Figure 1.4) depending on the functionality of the constituent dielectric material. For example, if the constituent dielectric layer is purely dielectric (the outermost circle in Figure 1.4), the converse magnetoelectric coupling can occur through electric field modulation of spin polarized electron densities. If the constituent dielectric layer is also a piezoelectric or ferroelectric, the number of possible ME coupling mechanisms could also include the strain transfer as a coupling mechanism.

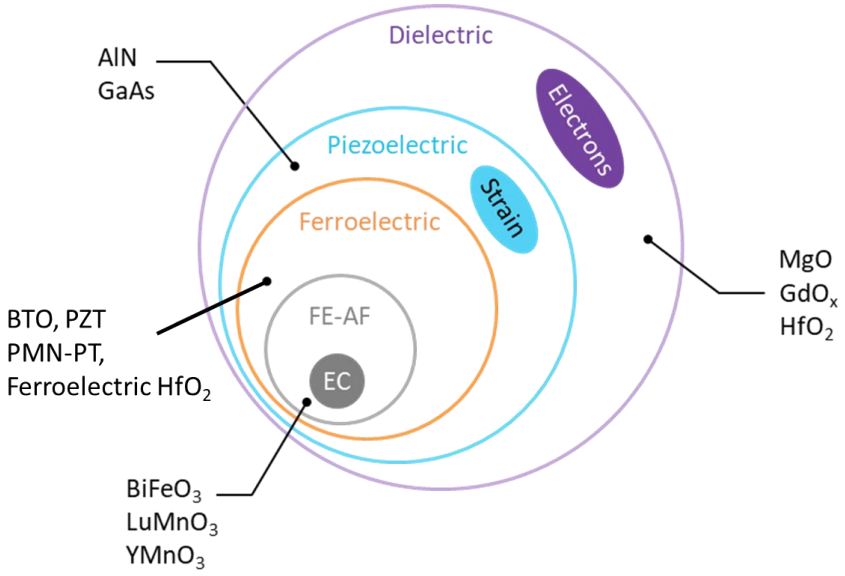

Figure 1.4 Examples of dielectric materials that have been used to interface with ferromagnetic materials to form a magnetoelectric composite. The solid shapes indicate the type of coupling mechanism possible for each type of interface. Adapted from: (Chu, Pourhosseini et al. 2018).

The mechanism for the different possible ME couplings from the solid ellipses in Figure 1.4 is further highlighted in Figure 1.5, with examples of typical magnetoelectric responses that

can be observed for each mechanism. In Figure 1.5(a), the change of electron densities with an electric field shifts the Fermi level (E_F) and hence the local density of states (LDOS). In Figure 1.5(b), strain can be transferred across the ferromagnetic/piezoelectric interface in response to an electric or magnetic field via the piezoelectric or magnetostrictive effect, respectively. In Figure 1.5(c), for a single antiferromagnetic (AF) domain with perpendicular magnetization (shown by the arrows in the bottom layer), the exchange coupling arises from the Heisenberg-type exchange interaction between the uncompensated surface magnetization and the local magnetization at the bottom of the magnet.

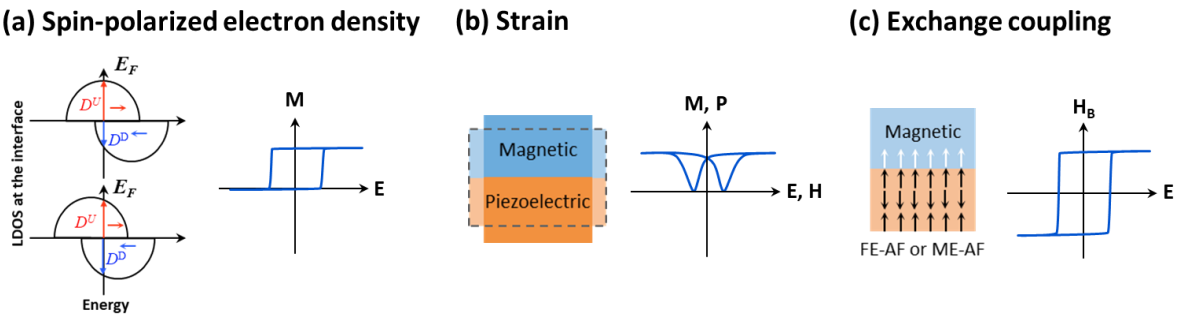

Figure 1.5 Schematics explaining both the mechanisms of magnetoelectric coupling and examples of possible magnetoelectric response enabled through modulation of (a) spin-polarized electron densities, (b) strain, and (c) exchange coupling. Adapted from: (Chu, Pourhosseini et al. 2018) and (Vaz 2012).

1.3 Material Challenges for Magnetoelectric Devices at the Nanoscale

Based on the type of magnetoelectric coupling and the mechanisms used to control the electric or magnetic ordering, a variety of applications have been proposed, including but not limited to magnetic field sensors, energy harvesters, antennas, memory devices, voltage tunable inductors, and high-frequency signal processing devices. This is summarized in Table 1.1.

Table 1.1 Classification of ME devices. Adapted from *(Cheng, Peng et al. 2018)*

ME coupling	Mechanism	Device examples
Direct coupling	H-field controls electric polarization	Field sensors, energy harvesters, antennas
Converse coupling	E-field controls magnetization	Random access memory (MeRAM)
	E-field controls permeability	Voltage tunable inductors
	E-field controls spintronics	Bandstop filters, tunable resonators

At the nanoscale, several material challenges arise for the integration of ferromagnetic and ferroelectric thin films toward magnetoelectric devices. This is due to the fact the ferromagnetic and ferroelectric properties of materials are highly dependent on the microstructure which is itself influenced by the deposition method and conditions. In the following sections, two challenges in the materials design are presented and discussed: ferromagnetic materials with strong magnetoelastic coupling, and ferroelectric materials with robust ferroelectric polarization at the nanoscale.

1.3.1 Ferromagnetic Materials with High Magnetoelastic Coupling and Low Losses

One of the key materials challenge for strain-mediated ME devices is the need for a ferromagnetic material with high magnetostriction and low magnetic loss to achieve a strong magnetomechanical coupling. This presents a considerable challenge from a materials design perspective due to the fact that the origin of magnetostriction is rooted in the magnetocrystalline anisotropy (MCA) which in turn contributes to magnetic loss.

An overview of previously studied ferromagnetic thin films, along with key relevant properties (FMR linewidth, coercivity, saturation magnetostriction, and resistivity) is presented in Table 1.2.

Table 1.2: Properties of select ferromagnetic materials. Where available, data for thin film material properties is used.

Material	FMR LW (Oe)	H_c (Oe)	λ_s (ppm)	M_s (emu/cc)	$d\lambda/dH$ (ppm/Oe)	Resistivity ($\mu\Omega$-cm)	Ref.
Fe	65	<30	<5	1600	-	40	[1-5]
Ni	180	35	41	520	0.17	20	[6-10]
$Tb_xDy_{1-x}Fe_2$	1200	2300	880	700	2.4	60	[11-13]
$Ni_{80}Fe_{20}$	30	<3	<3	795	-	40	[14-16]
$Fe_{65}Co_{35}$	110	120	~30	1800	-	15	[17-20]
$Fe_xCo_{1-x}Al_y$	>50	15	-	1550	-	-	[21]
FeCoN		5	44	1500-1800	-	45	[22, 23]
FeCoB	15-50	<2	40-50	1500-1800	~1.4	115	[20, 23, 26, 27]
FeCo/NiFe	-	~10	-	-	-	-	[18]
FeCo/Cu	-	~12	-	-	-	-	[18]
FeCoN/NiFe	-	<1	40	-	-		[28, 29]
FeCoB/NiFe	-	<1	17	1700	~0.7	34.7	[30]
$Fe_{80}Ga_{20}$	137	65	20-100	1150	0.9-2	140	[14, 31-34, 37]
FeGaB	16	<1	70	915	6	180	[31, 34]
FeCo/NiFe Multilayers	-	5	58	1500-1700	~3.6	-	[35]
FeGa/NiFe Multilayers	164	5	40	1050	~8	-	[14, 37]
FeCo/Ag Multilayers	-	3	70	-	-	-	[36]

[1] (Kuanr, Camley et al. 2004) [2] (Kim and Oliveria 1993); [3] (Grössinger, Turtelli et al. 2014); [4] (Abe, Kawai et al. 2018); [5] (Aldridge and Raeburn 1976); [6] (Bailey and Vittoria 1973); [7] (Heavens 1991); [8] (Gontarz, Ratajczak et al. 1964); [9] (Danan, Herr et al. 1968); [10] (Avery, Mason et al. 2015); [11] (Panduranga, Lee et al. 2018); [12] (Gao, Pei et al. 2008); [13] (Cook, Harringa et al. 2000); [14] (Rementer, Fitzell et al. 2017); [15] (Klokholm and Aboaf 1981); [16] (Mayadas, Janak et al. 1974); [17] (Cooke, Gibbs et al. 2001); [18] (Jung, Doyle et al. 2003); [19] (Kim, Kim et al. 2004); [20] (Hida, Falub et al. 2018); [21] (Ariake, Kanada et al. 2017); [22] (Sun, Wang et al. 2000); [23] (Lu-Ran, Hua et al. 2012); [23] (Kohmoto, Munakata et al. 2004); [24] (Xing, Liu et al. 2011); [26] (Platt, Minor et al. 2001); [27] (Díaz, Quirós et al. 2012); [28] (Sun, Wang et al. 2000); [29] (Sun and Wang 2002); [30] (Ito, Okamoto et al. 2005); [31] (Lou, Insignares et al. 2007); [32] (Clark, Wun-Fogle et al. 2001); [33] (Wang, Huang et al. 2010); [34] (Gao, Yang et al. 2009); [35] (Rengarajan, Yun et al. 1997); [36] (Lafford, Gibbs et al. 1994); [37] (Shi, Wu et al. 2019)

One of the most successful magnetostrictive materials is the $Tb_xDy_{1-x}Fe_y$ (x = 0.27-0.30, y = 1.9-3), also known as Terfenol-D. This alloy exhibits a large room temperature magnetostriction up to 2000 ppm in bulk form (Clark, Teter et al. 1988). The constraint of Terfenol-D for commercial development is the high cost and shortage of the rare-earth elements, Tb and Dy. For implementation in the development of a strain-mediated magnetoelectric antenna, the drawback is the low piezomagnetic coefficient and high field required for magnetic saturation. As such, a more recently developed is the $Fe_{1-x}Ga_x$ alloy (or Galfenol) that is rare-earth-free, inexpensive, yet still exhibits moderate magnetostriction (up to ~400 ppm in bulk form) under a very low magnetic field of 100 Oe at room temperature (Atulasimha and Flatau 2011).

It can be seen that both Terfenol-D and FeGa have values of their coercivity and magnetostriction that follow a similar trend to conventional ferromagnetic materials as plotted in Figure 1.6. This is due to the fact that the origin of magnetostriction is rooted in the magnetocrystalline anisotropy (MCA) which itself contributes to the coercivity. Successful ways of engineering materials toward the top left of this material space (high magnetostriction, low coercivity) have been to start with ferromagnetic material with at least modest magnetostriction and disrupt the microstructure to effectively reduce the MCA. Two methods that have been explored that are highlighted in Figure 1.6 have been to add small dopants (e.g., FeGa → FeGaB; FeCo → FeCoN, FeCoB) and multilayering (e.g., FeGa → FeGa/NiFe; FeCo → FeCo/Ag).

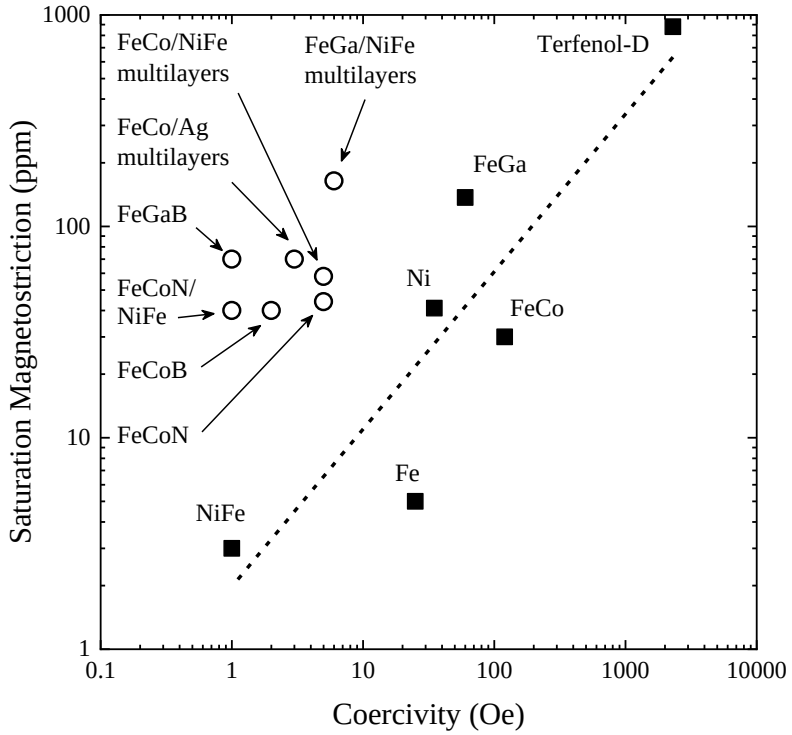

Figure 1.6: Plot of saturation magnetostriction versus coercivity for the ferromagnetic thin films listed in Table 1.2. The dashed line is a linear fit to the materials plotted with a solid square.

Multilayering of FeGa/NiFe thin films has been of recent increasing interest and several recent studies by various researchers are summarized in Table 1.3. In general, the addition of NiFe interlayers leads to a reduction in the coercivity of FeGa thin films which is also well below the expected volumetric average of the two magnetic phases. Of particular note is the report by Wu *et al.* that integrated FeGa/NiFe multilayers as the ferromagnetic phase on a piezoelectric AlN substrate in a ME device to find a 4-fold increase in the ME coupling coefficient over a single phase FeGa magnetic material (Shi, Wu et al. 2019).

Table 1.3: Summary of recent studies on FeGa/NiFe ferromagnetic composites

Material	Findings	Reference
FeGa/NiFe multilayer nanowires	Composite displays soft magnetic properties, though no comparison to single phase FeGa nanowires	(Lupu, Chiriac et al. 2008)
FeGa/NiFe multilayer thin films	Smaller coercivity than single phase FeGa and as well as below the average of individual NiFe and FeGa phases	(Rementer, Fitzell et al. 2017)
FeGa/NiFe multilayer thin films	8-fold increase in piezomagnetic coefficient and 4-fold increase in ME coefficient when integrated in a ME device over a single FeGa phase	(Shi, Wu et al. 2019)
FeGa/NiFe bilayer thin films	FeGa/NiFe bilayers show different microstructural and magnetic properties depending on the order of deposition	(Wang, Wang et al. 2020)

Furthermore, insulating layers have been used by various researchers to enhance the efficiency of ferromagnetic materials at high frequency. Examples of demonstrations of insulating interlayers in ferromagnetic materials include composites of: FeGaB with Al_2O_3 (Imran, Ge et al. 2018), FeCoB with Al_2O_3 (Xing, Liu et al. 2011), Fe with Al_2O_3 (Takakura, Ikeda et al. 2001), and NiFe with NiFeO (Xu, Dai et al. 2015). Additionally, there have seen successful demonstrations of the performance of FeGaB with Al_2O_3 for application for high frequency magnetic and magnetoelectric inductors. This enhancement is attributed to reduced eddy current losses across the thickness of the ferromagnetic film with an insulating interlayer.

1.3.2 Ferroelectric Materials with Robust Ferroelectricity at the Nanoscale

1.3.2.1 Experimental Comparisons

Ferroelectric materials for ME devices based on the voltage control of magnetism have traditionally been based on ABO_3 perovskite oxides. A comparison of common ferroelectric thin film materials is shown in Table 1.4. Ferroelectricity in HfO_2 was discovered in HfO_2 in 2011 (Böscke, Müller et al. 2011) and has gained increasing interest due its advantages over conventional perovskite ferroelectrics which are discussed in the following sections.

Table 1.4: A comparison of the most common ferroelectric thin film materials to HfO_2-based ferroelectrics. Adapted from (Mikolajick, Slesazeck et al. 2021)

Material	$Pb(Zr, Ti)O_3$	$SrBi_2Ta_2O_9$	$BiFeO_3$	HfO_2-based
P_r ($\mu V/cm^2$)	10-40	5-10	90-95	10-40
E_c (kV/cm)	50-70	30-50	100-1500	2000-5000
k	~400	~200	~50	~25
Synthesis method	Sol-gel, sputtering	CVD	PLD	CVD, sputtering
Minimum physical thickness (nm)	>50	>25	>10	~1
CMOS compatibility?	No	No	No	Yes

1.3.2.2 Experimental comparisons from literature

Conventional perovskite ferroelectrics have several key shortfalls at the nanoscale both in terms of thickness of the film and width of ferroelectric domains. With decreasing thickness, depolarization field effects due to the polarization charges at the surface have an increasingly larger influence. Ferroelectricity becomes unstable due to depolarizing field effects from polarization charges at the surface and below a critical thickness, the ferroelectric polarization vanishes (see illustration in Figure 1.7).

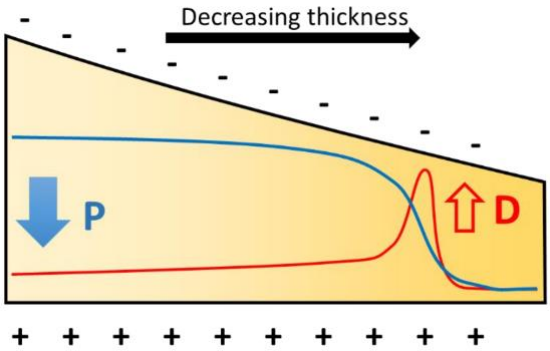

Figure 1.7: Schematic illustrating thickness dependence of the polarization (P) and depolarizing field (D) have a thickness dependence, resulting in the minor influence of the depolarizing field on polarization in the high thickness range and a suppression of polarization at low thicknesses. Adapted from *(Nordlander, De Luca et al. 2018).*

Conventional perovskite ferroelectrics also face a limitation in their domain wall size. The transition between two ferroelectric domains with antiparallel out-of-plane domains is generally observed to occur over a transition region and can generally occur over relatively short scale of a few nanometers. The transition of such antiparallel ferroelectric domain walls in perovskite ferroelectrics with out-of-plane polarization are predominantly Ising-like, i.e., with no in-plane component associated with polarization rotation [see Figure 1.8(a)], although other wall characteristics have been described and observed as shown in Figure 1.8(b-d) (Lee, Behera et al. 2009, Guyonnet 2014).

In contrast, studies on ferroelectric HfO_2-based thin films have been found ferroelectricity to be stable down to ~ 1 nm thickness (Cheema, Kwon et al. 2020) with polarization increasing with decreasing thickness. The differences in the fluorite structure of HfO_2 compared to the perovskite structure ferroelectrics that allow for enhanced stability of ferroelectricity at the nanoscale is discussed in later sections.

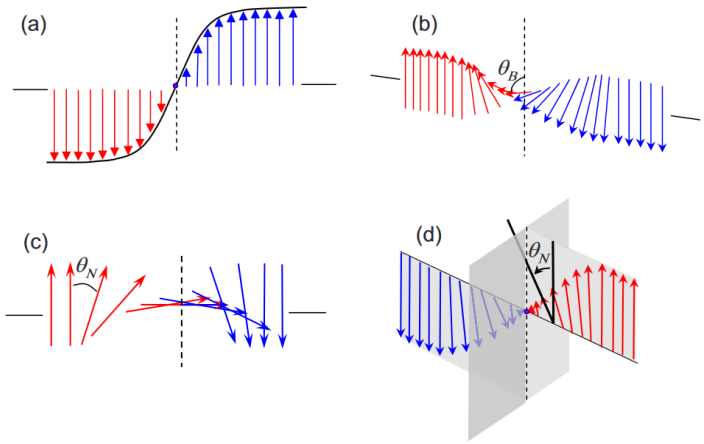

Figure 1.8: Schematic illustration of different types of ferroic domain walls. (a) Ising type, showing a gradual magnitude variation but no rotation of the order parameter. (b) Bloch type, showing a gradual rotation, and no change in magnitude. (c) Néel type, showing an in-plane rotation and no change in magnitude. (d) Mixed Ising-Néel type, showing both in-plane rotation and decrease of the magnitude. A mixed Ising-Bloch type would be similar, with an out-of-plane rotation. Adapted from (Lee, Behera et al. 2009).

Figure 1.9(a) shows an example for the case of $PbTiO_3$ studied using density functional theory (DFT) by Lee *et al.*, the polarization becomes substantially suppressed inside a switched single-unit-cell domain (Lee, Lee et al. 2020). The switched domain is only marginally stable, and the polarization of the neighboring antiparallel domains is also diminished. Additionally, it was pointed out that the marginal stability to switch the polarization in a single-unit-cell domain in $PbTiO_3$ leads to spontaneous expansion to a wider domain [Figure 1.9(b)].

Lee *et al*. also identified the ferroelectric switching behavior of orthorhombic HfO_2 to be in sharp contrast to that of the perovskite structure $PbTiO_3$. Switching a single-unit-cell domain in HfO_2 is marginally more thermodynamically stable than a uniformly polarized structure (Figure 1.10). The unit cell of HfO_2 is partitioned into a half-unit cell that resembles the parent nonpolar tetragonal phase and half that is polar from the displacements of the O atoms, and it is the nonpolar half-unit cell that insulates neighboring domains to reduce depolarization effects. Thus, a switched

ferroelectric domain has equally strong polarization to its antiparallel neighboring domains. The ferroelectric stability of a single-unit-cell-domain in HfO_2 would allow for high density of devices < 1 nm in lateral width.

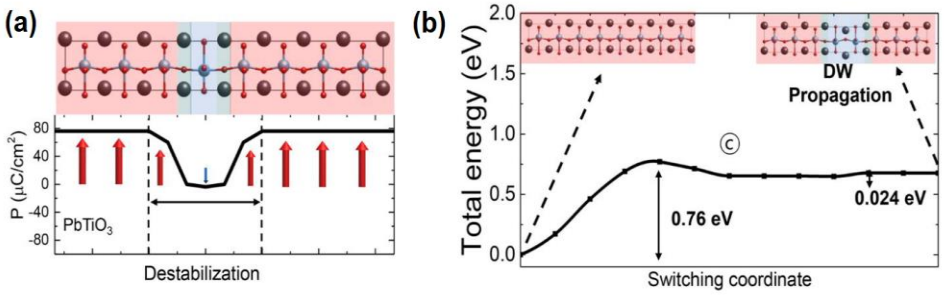

Figure 1.9: (a) Atomic structure of the thinnest domain for $PbTiO_3$ and variation of the polarization along the direction perpendicular to the domain walls. (b) Energy along the path of polarization switching of $PbTiO_3$ starting from a uniformly polarized structure. Adapted from (Lee, Lee et al. 2020).

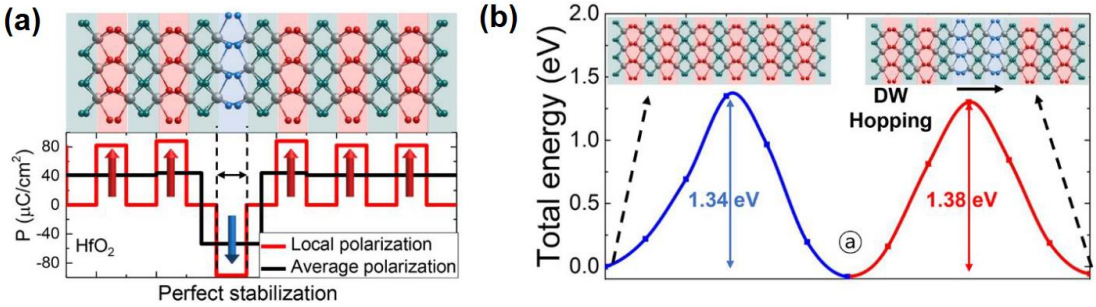

Figure 1.10: (a) Atomic structure of the thinnest domain for HfO_2 and variation of the polarization along the direction perpendicular to the domain walls. (b) Energy along the path of polarization switching of HfO_2 starting from a uniformly polarized structure. Adapted from (Lee, Lee et al. 2020).

The advantages discussed thus far for ferroelectric HfO_2 over conventional perovskite ferroelectrics makes it a promising material for nanoscale ferroelectric applications. Indeed, several researchers have used theoretical and experimental methods to explore and demonstrate the use of HfO_2-based materials for the ferroelectric control of magnetism in a magnetoelectric composite and these are reviewed in Table 1.5. In general, at the interface the ferroelectric

switching between polar states can be used to control the magnetic anisotropy and allow for the modulation of the remnant magnetization, magnetic moments, and magnetic coercivity of the magnetic phase at the interface.

Table 1.5: Summary of recent studies on ME composites that incorporate a HfO_2-based ferroelectric for the voltage control of magnetism.

ME composite	Exp. or Theoretical?	Findings	Reference
HfO_2 (6.5 nm) /Co (0.45 nm)/Pt (5 nm)	Exp.	Modulation of M_r by ~41%	(Vermeulen, Ciubotaru et al. 2019)
$Hf_{0.5}Zr_{0.5}O_2$ (10 nm) /Ni (1.5 nm)	Both	Modulation of magnetic moments of Ni at interface by up to 0.27 μB	(Dmitriyeva, Mikheev et al. 2021)
$Hf_{0.5}Zr_{0.5}O_2$ (10 nm) /PtCoRu (5 nm)	Exp.	Modulation of Mr (~20%) and coercivity (~50%)	(Zhang, Li et al. 2021)
HfO_2/Ni	Theoretical	Modulation of magnetic moments of Ni at interface by up to 0.25 μB interface	(Yang, Tao et al. 2019)

1.4 Scope and Organization

This work is focused on addressing two key issues in the two material systems discussed in Section 1.3.1 and Section 1.3.2 As pointed out, both FeGa/NiFe multilayer composite films and ferroelectric HfO_2 are promising materials with demonstrated application toward integration in magnetoelectric composite devices. However, there remains key challenges for each respective material system.

For the case of FeGa/NiFe multilayers: it is not well understood what the influence of NiFe on FeGa is that leads to an enhancement of the soft magnetic properties of FeGa. While prior studies in Table 1.3 have suggested that it is the result of exchange coupling between the soft and

hard magnetic phases (NiFe and FeGa, respectively), this is at odds with prior studies of exchange coupling between hard/soft magnetic composites. For example, in several prior studies of hard/soft composites, it is described that at the interface the soft magnetic domains become pinned to the hard magnetic domains as a result of exchange coupling resulting in a composite that maintains the high coercivity of the hard magnetic phase (Kneller and Hawig 1991, Liu, Luo et al. 1998, Fullerton, Jiang et al. 1999, Camley, Celinski et al. 2015). Thus, the unexpected enhancement of the soft magnetic properties of the FeGa/NiFe multilayers cannot be explained via exchange coupling. In Chapter 3 we identify the origin of the improvement in the soft magnetic properties of FeGa as arising from the underlayer effect. In Chapter 4, we optimize the magnetomechanical coupling of FeGa/NiFe multilayers by identifying the optimal multilayer configuration that minimizes the coercivity. Additionally, we explore the influence of Al_2O_3 insulating interlayers and their effect to improve the efficiency of FMR absorption for high frequency applications.

For the case of ferroelectric HfO_2: despite the wide range of studies on processing conditions and various factors (e.g. strain, dopants, applied, E-fields) that can promote the orthorhombic ferroelectric phase in HfO_2, the influence of the surface composition on the surface energy as a stabilizing factor has not been fully explored. Recent experimental studies have pointed to the composition of the interface with HfO_2 as having a significant effect on the phase fraction of the ferroelectric orthorhombic phase of HfO_2 over nonpolar phases after annealing (Lomenzo, Takmeel et al. 2015, Hamouda, Pancotti et al. 2020, Szyjka, Baumgarten et al. 2020, Fields, Smith et al. 2021, Yadav, Kashir et al. 2021). Thus, given that the surface plays an outsized role at the nanoscale, it is important to isolate the influence of the surface composition on the surface energy to stabilize the ferroelectricity in HfO_2 thin films to advance the integration and application toward

nanoscale devices such as magnetoelectric devices for efficient control of magnetism. This is covered in Chapter 5 and 6.

Chapter 2 Experimental and Computational Methods

To study the influence of the interface and deposition parameters on the soft magnetic properties of FeGa thin films, thin films were synthesized using a physical vapor deposition (PVD) sputtering process. Structural and magnetic characterization of the synthesized thin films was performed using X-ray photoelectron spectroscopy (XPS), X-ray diffraction (XRD), Superconducting Interference Device (SQUID) magnetometry, and ferromagnetic resonance (FMR) spectroscopy.

For the case of HfO_2, computational chemistry – in this case, density functional theory (DFT) – can provide us with further insights into the structural and electronic properties of a system that are often not accessible using experimental techniques. The implementation of DFT described herein is used to isolate the effect of the surface composition and its influence on the surface energy to stabilize the ferroelectricity in HfO_2 thin films.

2.1 Experimental Methods

2.1.1 Sputtering deposition for synthesis of thin films

In a PVD sputtering process, atoms are ejected from a target source by means of bombardment with high energy particles that can be supplied by plasma. Argon, nitrogen and oxygen are common choices for generating the plasma in a low-pressure environment. The accelerated free electrons ionize the gas molecules or atoms forming positively charged ions.

These ions are attracted to the negatively charged source, and in turn bombard the surface with high energy, ejecting particles from source. The ejected particles are directed at a substrate by the incident angle of the high energy particles and form a thin film on a substrate. A schematic of the PVD sputtering process is shown in Figure 2.1. Operating procedure can be found in the appendices.

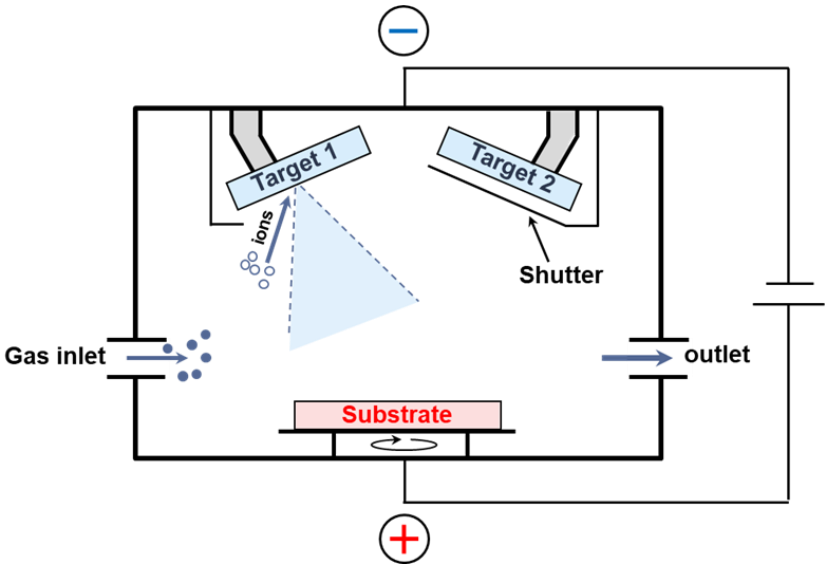

Figure 2.1: Schematic of a sputtering deposition chamber used to deposit films on a substrate by bombardment of a target by ionized gas.

The target in the sputtering chamber is held in a cathode, made of a material with very low resistance that attracts the positively charged argon ions. Oxygen or nitrogen gases are typically used in reactive sputtering, where the atoms ejected from the target react with the plasma. Argon, which is used in this work, is the more common choice for sputtering metals. Depending on the properties of the material, either a direct current (DC) or radio frequency (RF) bias is used. An RF bias would be necessary in the case of materials, such as oxides or nitrides, where charge build-up would cause the positively charged sputtering ions to be repelled from the target.

The following parameters can be controlled during sputtering: sputtering power, gas flow rate, and operating pressure of the system. The parameters used in this work are listed in Table 2.1. In both RF and DC systems, an increase of sputtering power results in a higher sputtering yield, and therefore a higher growth rate. Gas flow rate, power, and sputtering pressure parameters need to be optimized as they can affect the composition and stress of the sputtered films which in turn affect the magnetic and magnetostrictive properties. Additionally, magnetron sputtering is used to increase the ionization of argon by trapping electrons near the surface of the target, accomplished with a permanent magnet placed behind the cathode, which draws in the positive argon ions and allow for a higher sputtering rate.

Table 2.1: Sputter deposition parameters for the targets used to deposit the various thin films sputter deposited in this work. An ULVAC JSP 8000 sputter system with a base pressure of 2×10^{-7} Torr at room temperature was used for the depositions in this work.

Target	Sputtering Power	Ar pressure
$Fe_{80}Ga_{20}$	200 W (DC)	0.5 mT
$Ni_{80}Fe_{20}$	100 W (DC)	0.5 mT
Cu	100 W (DC)	0.5 mT
Ta	100 W (DC)	0.5 mT
Al_2O_3	300 W (RF)	0.5 mT

For this work, an ULVAC JSP 8000 magnetron sputtering system in the Integrated Systems Nanofabrication Cleanroom of the California NanoSystems Institute at UCLA is used. This system can hold up to four different sputtering targets, which can be opened at separate times during the deposition process. This enables us to sequentially deposit multiple metallic films without breaking vacuum and compromising the interface.

2.1.2 X-Ray Photoelectron Spectroscopy (XPS)

XPS is a highly surface-sensitive technique that is used to determine the elemental composition and oxidation state of atoms in a material. A schematic of this process is shown in Figure 2.2.

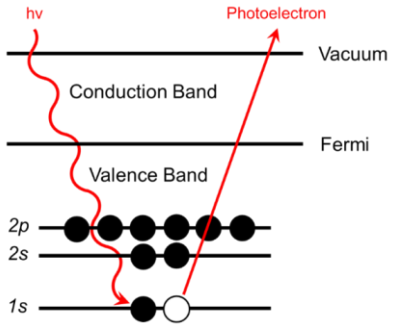

Figure 2.2: Schematic of the working principle of XPS.

The technique involves a sample being bombarded with X-rays, which causes electrons to be ejected from the core shells of atoms in the material. By measuring the kinetic energy of the ejected photoelectrons, the binding energy of the electron can be calculated from the following equation:

$$\boldsymbol{E_b = hv - E_k - \phi} \tag{2.1}$$

where E_k is the kinetic energy of the detected electrons, *hv* is the kinetic energy of the incident x-rays, and *v* is the work function that represents the energy required to remove an electron from the atom. By comparing the binding energy of the detected electrons to standard values of different materials, the identity of the elements and their environment can be determined as well as the relative composition by the proportion of the different detected elements. Because the mean free path of the ejected photoelectrons is only a few nanometers, this technique is highly sensitive to the surface composition of the material.

An example of an XPS survey spectra obtained for an FeGa film is shown in Figure 2.3.

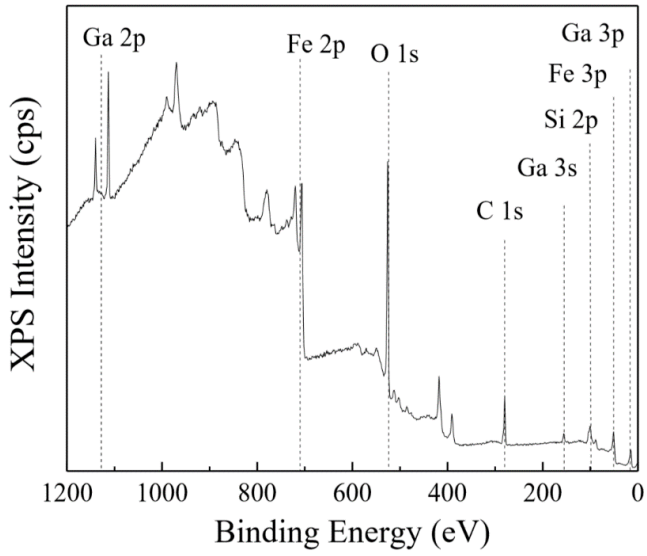

Figure 2.3: XPS survey scan of a $Fe_{75}Ga_{25}$ film grown on a Si substrate. Major peaks are identified.

The elemental composition of a sample can be calculated from the relative proportion of photoelectrons ejected from each element represented by the integrated area of each peak at their binding energy. The integrated areas must also be corrected by dividing by a relative sensitivity factor (RSF) specific to each element before making direct comparisons between peaks.

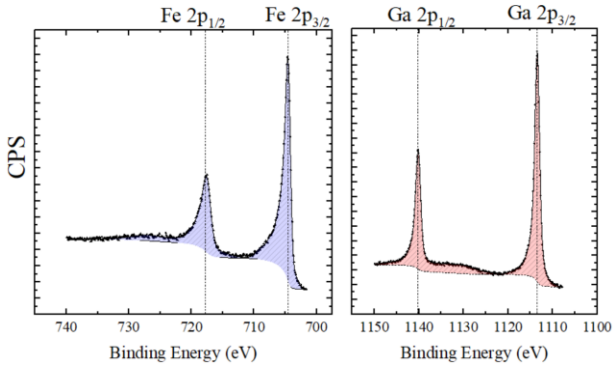

Element	Binding Energy (eV)	RSF
Fe 2p	706.7	2.957
Ga 2p	1115.5	5.581

Figure 2.4: (left) Individual XPS spectra of Fe 2p and Ga 2p regions. (right) Binding energies and RSF values for Fe 2p, Ga 2p photoelectrons used to calculate the relative stoichiometry.

In the case of the data shown in **Error! Reference source not found.** for an Fe-Ga alloy t hin film, the relative ratio of the Fe 2p and Ga 2p peaks can be calculated with the RSF values shown in Figure 2.4 (right panel) to obtain a 3:1 ratio corresponding to $Fe_{75}Ga_{25}$.

2.1.3 X-Ray Diffraction (XRD)

XRD is a technique that can be used to characterize the crystallographic nature of a material. Figure 2.5 shows a schematic of the working principle of this technique.

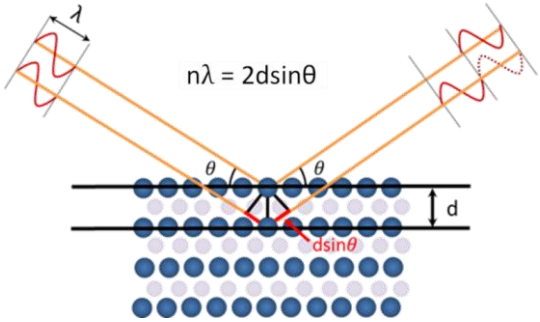

Figure 2.5: Schematic of the working principle of XRD.

During XRD, x-rays with wavelengths shorter than the lattice spacing irradiate a sample surface at a sweeping angle. Constructive interference occurs if the photon path difference is equal to an integral number of wavelengths. Using Bragg's law ($n\lambda = 2d\sin\theta$; θ is the diffraction angle, λ is the incident x-ray wavelength, and n is an integer number order of reflection) the crystal structure and lattice parameter can be determined based on the angle of the detected diffraction peak at the given angle, and the lattice parameters can be extracted. A map of the peaks at all the angles where the constructive interference occurs allows us to uniquely identify the crystal structure of the entire material.

Further analysis of XRD diffraction peaks can be done by examining the diffraction peak to obtain the average size of coherently reflecting crystallites in the sample, often termed as the grain size. This is done using the Scherrer equation:

$$\boldsymbol{\tau = \frac{K\lambda}{\beta \cos\theta}} \tag{2.2}$$

where τ is the averaged grain size for a certain crystalline phase, K is a dimensionless shape factor (set to 0.9 for assumed cubic crystallites), λ is the wavelength of the incident X-ray, and β is the integrated breadth of the XRD peak of interest after subtracting the instrumental broadening, and θ is the peak angle. The Scherrer equation is often misused, and generally would only allow us to make conclusions based on the trends observed. This is because the shape factor can vary, the full width at half max is often used instead of the integral breadth which can vary specially if the peak shape does not follow a Gaussian distribution, the instrumental broadening is not subtracted, and the equation does not account for strain or defects in the grains, or if the coherently reflecting regions consist of domains (Kaufmann 2006).

An example of an XRD spectra for a 100 nm sputtered polycrystalline FeGa film grown on a Si (100) substrate is shown in Figure 2.6. Several phases in the primarily disordered Fe A2 polycrystalline matrix can be identified.

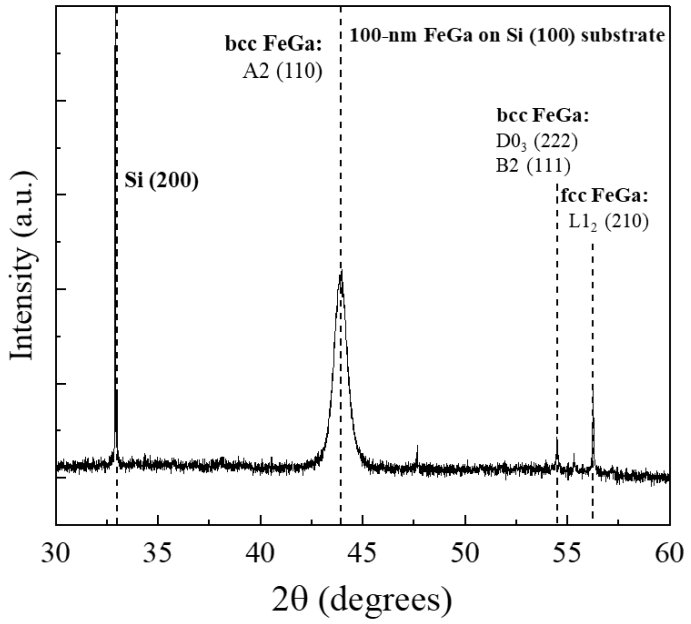

Figure 2.6: XRD spectra of a 100 nm FeGa film grown on a Silicon substrate.

Using bragg's law from Figure 2.5, we can calculate the lattice parameter of the main A2 phase in Figure 2.6 to be $d = \lambda/(2\sin\theta) = 0.206$ Å.

2.2 Superconducting Quantum Interference Device (SQUID) Magnetometry

SQUID Magnetometry is a technique that is very sensitive to detect small magnetic moments and is ideal for measuring the static magnetic properties of thin ferromagnetic films. In this work, an MPMS3 tool by Quantum Design is used which is capable of applying magnetic films of up to ±5 Tesla and detect magnetic moments as low as 6×10^{-7} emu at room temperature. A schematic of the working principle is shown in Figure 2.7. Operating procedure can be found in the Appendices.

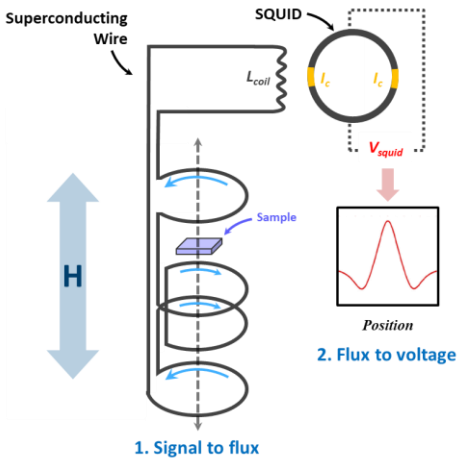

Figure 2.7: Schematic of the working principle of a SQUID magnetometer.

The set-up uses a combination of superconducting looped wire inductively coupled to a superconducting SQUID loop that itself is separated by two Josephson junctions. During operation, a sample moves through a set of superconducting wire loops. In response to the changing magnetic flux due to the sample through the loops, a current is induced in the superconducting wires. The SQUID must be shielded away from the magnetic field of the Helmholtz coils that apply a magnetic field to the sample, so it is located away from the sample, but it is inductively coupled via a transformer to the superconducting wire carrying the induced current by the changing magnetic flux of the moving sample.

The SQUID itself operates based on the Josephson Effect where the two parts of the superconducting loop are separated by a thin non-superconducting layer that electrons can tunnel through it without losing energy. There are several key ideas that explain the operation:

i. When a current, I, is applied to one side of the loop, it is split between the two branches of the loop equally, termed I_c.

ii. When a small magnetic flux goes through the SQUID loop from the inductively coupled wire, a screening current, I_s, is generated to cancel this because the

superconducting material expels any magnetic field. This current adds to the current in one branch and subtracts from the current in the other. These are termed: $\boldsymbol{I_1 = \frac{I_c}{2} - I_s}$ and $\boldsymbol{I_2 = \frac{I_c}{2} + I_s}$

iii. The magnetic flux generated by the screening current must me quantized. So, if the applied magnetics flux through the SQUID (from the inductively coupled wire) exceeds $\boldsymbol{\phi_0/_2}$, it is energetically favorable to *increase* screening current to induce an opposing flux up to the next integer multiple of $\boldsymbol{\phi_0}$. Similarly, if the magnetic flux through the SQUID is less than $\boldsymbol{\phi_0/_2}$, it is more energetically favorable to de*crease* screening current to induce an opposing flux down to the nearest integer multiple of $\boldsymbol{\phi_0}$.

iv. From (i)-(iii), the SQUID generates and oscillating screening current in response to an increasing magnetic flux through the SQUID loop as the screening current either increases or decreases to generate the nearest quantum magnetic flux.

v. If a constant bias current is maintained in the SQUID magnetometer, an oscillating voltage can be detected across the two junctions. These oscillations are counted and are correlated to a magnetic flux that is applied to the sample by the equation: $\boldsymbol{\Delta V = \frac{R}{L_{coil}} \Delta \phi}$, where L_{coil} is the inductance of the superconducting coil and R is the shunt resistance (Lueken 2012).

SQUID magnetometry will also pick up the diamagnetic or paramagnetic response of the substrate in response to an applied magnetic field which can be eliminated by subtracting the linear non-ferromagnetic response in the raw data. For materials like FeGa this correction is often unnecessary as the magnetic response from the film is much greater than the background linear

response. An example of a magnetic hysteresis loop obtained with SQUID magnetometry is shown in Figure 2.8 for an FeGa film deposited on a Si substrate.

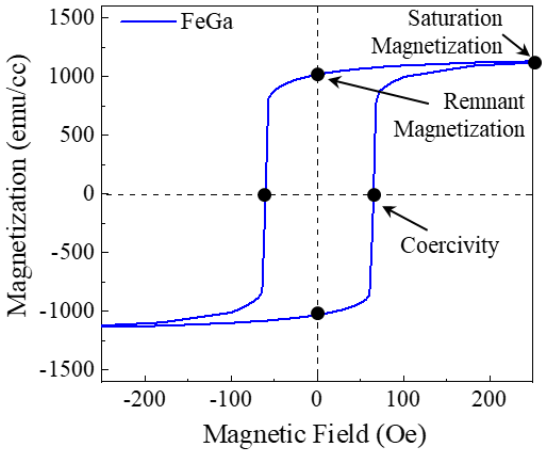

Coercivity	81 Oe
Remnant magnetization	1020 emu/cm^3
Saturation magnetization	1190 emu/cm^3

Figure 2.8: (left) Magnetic hysteresis loop obtained for a sputter deposited 100 nm FeGa thin film. (right) Values of the main properties of interest highlighted on the plot on the left panel.

2.3 Stripline Permeability Measurement

To obtain the permeability as a function of EM frequency of our ferromagnetic materials, a stripline measurement system is used. A schematic of the set-up is shown in Figure 2.9 and Figure 2.10.

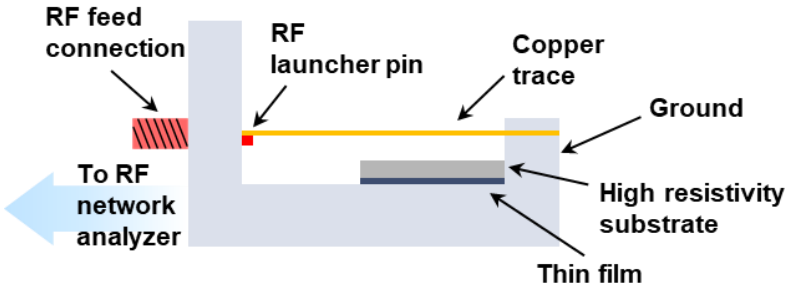

Figure 2.9: Schematic of the stripline set-up used to measure RF absorption of ferromagnetic thin films.

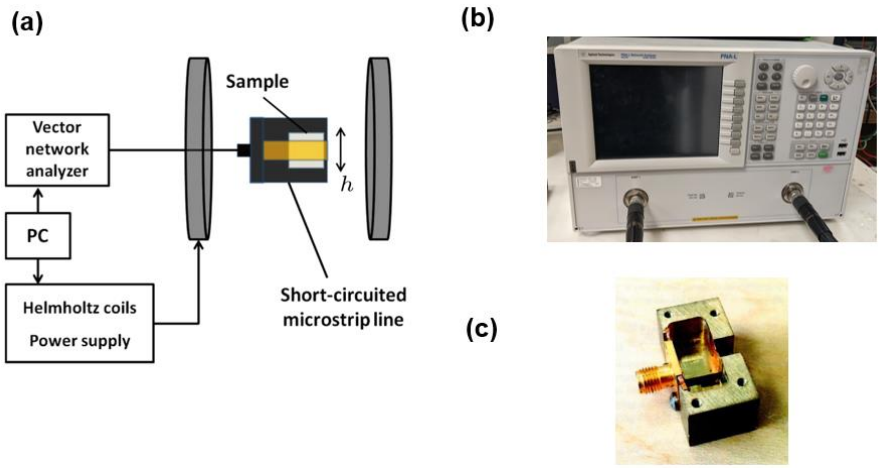

Figure 2.10: (a) Schematic depicting the placement of the stripline housing from Figure 2.9 between two Helmholtz coils with a feedthrough of the microwave coaxial cable coming from the vector network analyzer shown in (b). A picture of the actual stripline housing used is shown in (c).

This technique works by creating a short circuit on the stripline setup, where the EM wave is shorted to the ground. The RF network analyzer is calibrated with an empty cavity to assess the background scattering parameters (s-parameter) of the cavity which provide a measure of the reflected or absorbed input signal. This is then repeated for the bare substrate (highly resistive silicon) and then the substrate with the thin ferromagnetic film.

An example of the s_{11} scattering absorption parameter of a 100 nm FeGa ferromagnetic film grown on 2.5 nm NiFe underlayer on a resistive silicon substrate is shown in Figure 2.11. The raw data from after background subtraction is converted to absorption and this is depicted in Figure 2.12. The MATLAB script used to process the raw data collected from the vector network analyzer tool shown in Figure 2.10 can be found in the Appendices.

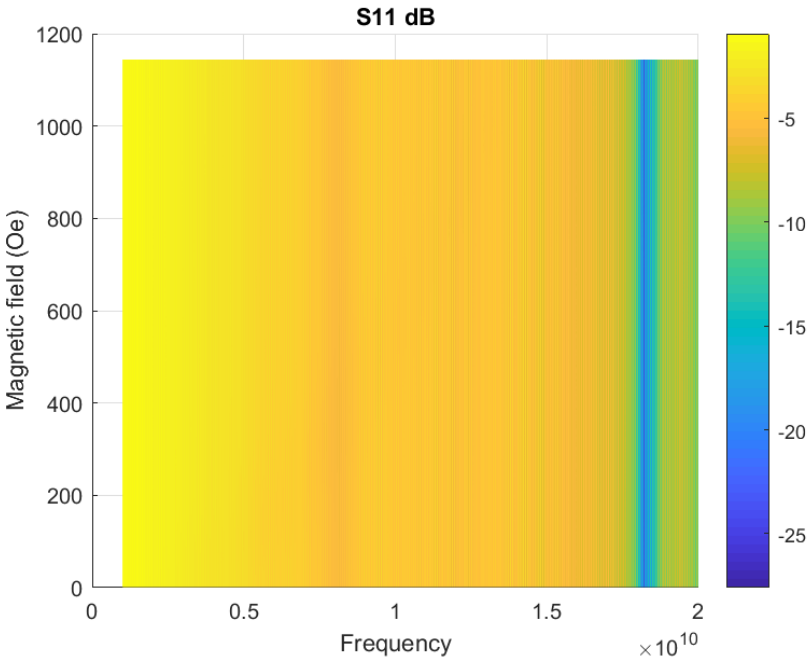

Figure 2.11: Raw uncorrected data for S_{11} absorption parameter of a 100 nm FeGa film on a 2.5 nm NiFe underlayer on a Si substate.

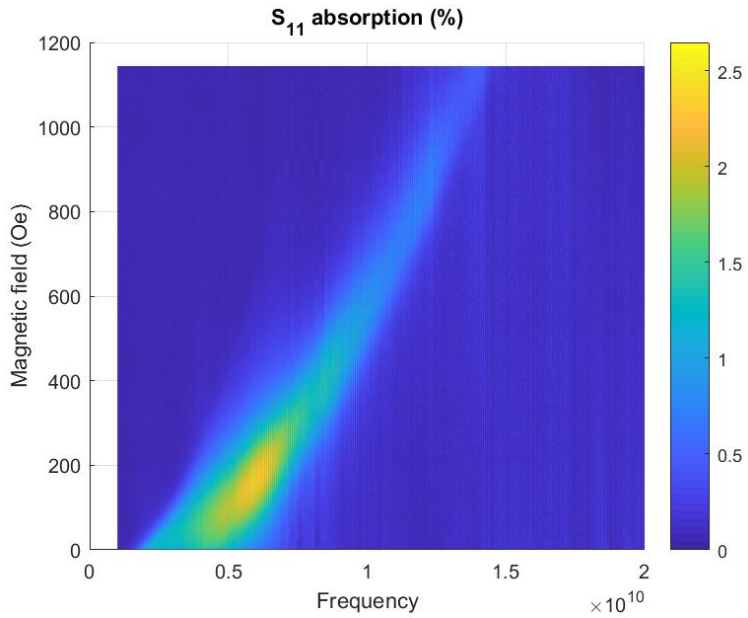

Figure 2.12: S_{11} absorption parameter with background subtracted from Figure 2.9.

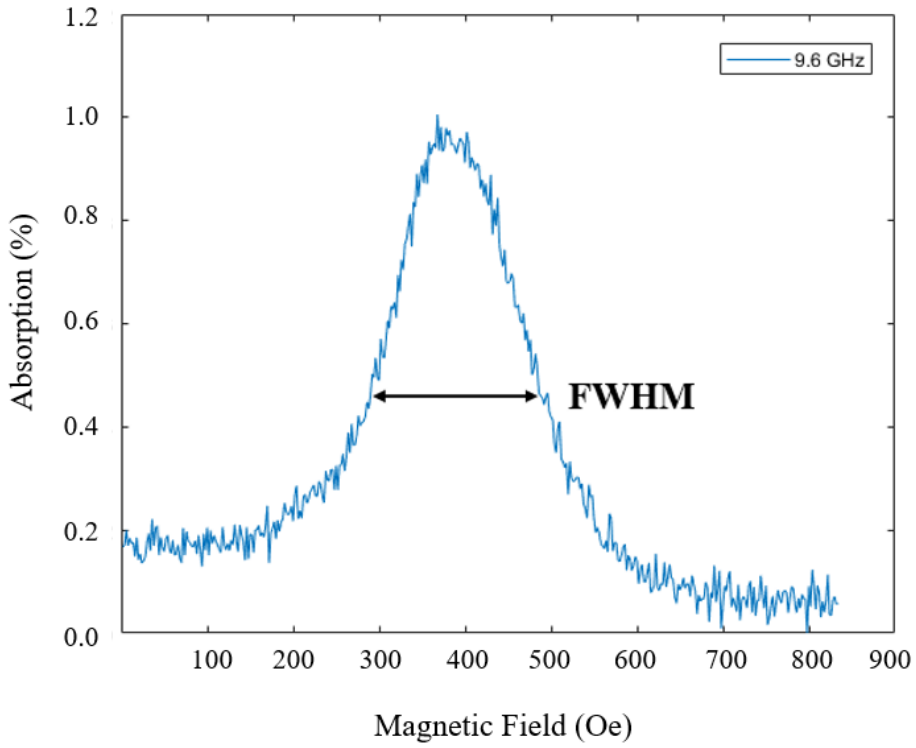

Figure 2.13: Cross section of the absorption as a function of the magnetic field from Figure 2.11 at a frequency of 9.6 GHz. Arrows depict measurement of FWHM.

Figure 2.13 depicts a cross section of Figure 2.12 to demonstrate the calculation of the FMR linewidth (ΔH). The FMR linewidth as a function of frequency (f_{FMR}) can then be used to calculate the gilbert damping, α, of a material using the following equation:

$$\mu_0 \Delta \boldsymbol{H} = \mu_0 \Delta \boldsymbol{H_0} + \frac{\boldsymbol{4\pi\alpha f_{FMR}}}{\boldsymbol{\gamma}} \tag{2.3}$$

Note that γ is the gyromagnetic ratio which is equal to ≈2.8 MHz/Oe.

2.3.1 Magnetoelastic characterization

In order to obtain magnetostriction measurements for FeGa films with different underlayers, an optical cantilever set-up was used as shown in the schematic in Figure 2.14. A

perpendicular AC magnetic field is applied along the short axis during the measurement, while a 100 Oe bias field is initially applied and held constant in the long axis in order to saturate the magnetization and access the full magnetostriction.

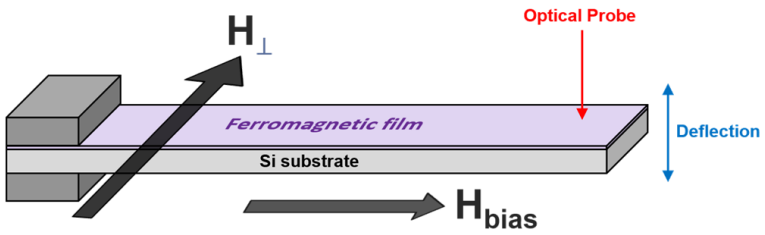

Figure 2.14: Schematic of the set-up used to measure the cantilever deflection and the relative directions of the constant saturating bias field and perpendicular AC magnetic field during the measurement.

The characterization for the magnetic field induced stress, b, of a 100 nm FeGa film on Si is shown in Figure 2.15 which is calculated from the deflection at the cantilever tip using the following relation (De Lacheisserie and Peuzin 1994):

$$\boldsymbol{b = -\frac{1}{d}\frac{t_s^2 E_s}{3t_f l^2(1+v_s)}} \tag{2.4}$$

where d is the deflection, t_s & t_f are the substrate and film thickness (100 μm & 100 nm, respectively), l is the distance between the clamping edge and the probe location (27 mm), and E_s & v_s are the Young's modulus and Poisson ratio of the Si substrate (169 GPa & 0.069, respectively). For thin films, the magnetostrictive stress is considered the more relevant parameter to describe magnetostrictive effects since the lateral deformation is blocked by the substrate and one can measure only the stress. This also avoids the need to measure the elastic properties of thin

films which can be difficult. However, for comparison to other literature on magnetostrictive thin films, the magnetostriction in terms of strain can be accessed from the relation: $\boldsymbol{\lambda} = -\frac{\mathbf{2}}{\mathbf{3}}\left(\frac{\mathbf{1}+\boldsymbol{\nu_f}}{\boldsymbol{E_f}}\right) \times \boldsymbol{b}$, where E_f and ν_f are the Young's modulus and Poisson ratio of the FeGa film which are approximated following the convention that $\left(\frac{\boldsymbol{E_f}}{\mathbf{1}+\boldsymbol{\nu_f}}\right) = \mathbf{50}$ GPa.

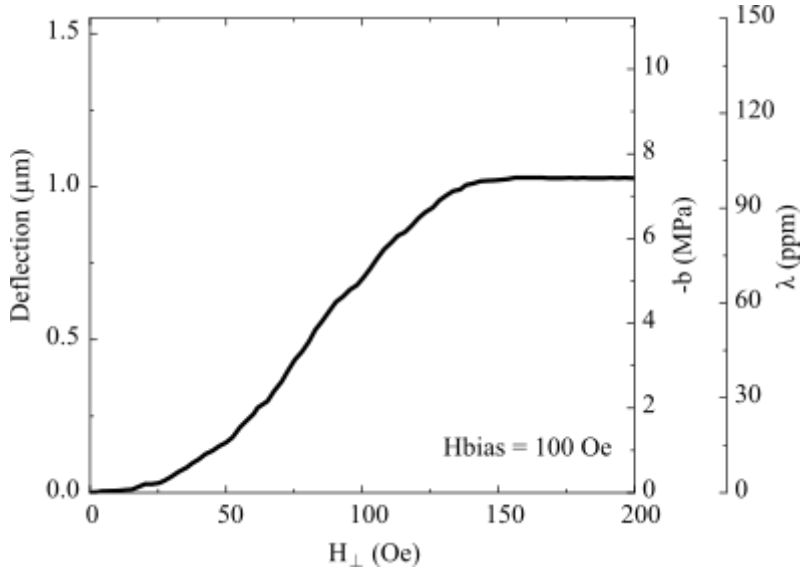

Figure 2.15: Measured deflection and calculated stress and magnetostriction as a function of magnetic field for 100 nm FeGa sputtered directly on Si using the set-up shown in Figure 2.14.

2.3.2 Underlayer and Multilayering Strategy

To study the influence of the substrate during growth on FeGa thin films on their soft magnetic properties, we explore the effect of different underlayer materials that serve as a buffer layer between the FeGa films and the substrate. A schematic of the strategy to study the underlayer effect is displayed in Figure 2.16. In Chapter 3 we present the results of the influence of different underlayer materials on the microstructure and in turn soft magnetic properties on FeGa films. The substrate can have a strong influence of the microstructure during growth of ferromagnetic films,

so it is of interest to identify the underlayer material that promotes soft magnetic properties (low coercivity and gilbert damping).

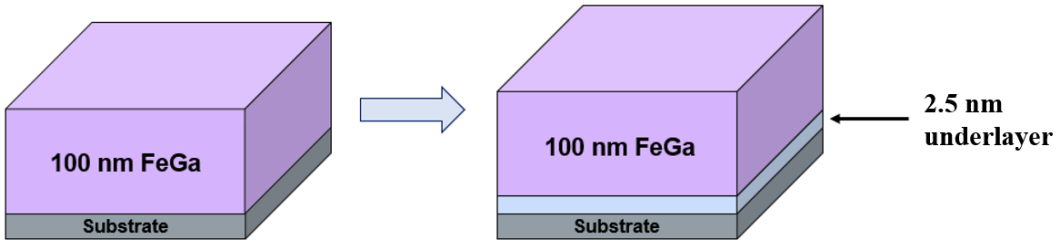

Figure 2.16: Schematic illustration of the strategy of using a thin underlayer as a buffer between an FeGa film and the underlying substrate.

After identifying the optimal underlayer material, we use the same underlayer as an interlayer in a multilayering strategy. It can be expected that across the thickness of an FeGa film, the influence of the underlayer is diminished, thus it can be expected that a multilayer structure can optimize the influence of the underlayer across the thickness of an FeGa thin film. A schematic of the multilayering approach in this work is shown in Figure 2.17. The total volume of FeGa is kept constant in each structure. The thickness of each interlayer is kept constant at 2.5 nm. The labels in Figure 2.17 (N=1, 2, 4, 10) correspond to the total number of FeGa bilayers with an interlayer pair, and the total thickness of each FeGa layer for each multilayer structure equals 100 nm / N.

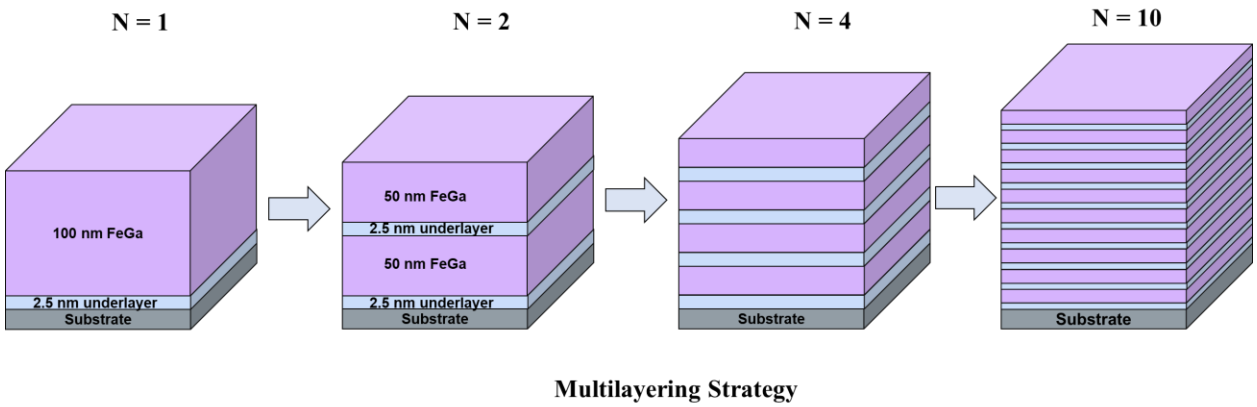

Figure 2.17: Schematic of multilayering approach that builds on the underlayer effect. The cumulative thickness of the FeGa film in the structure is kept constant at 100 nm and additional 2.5 nm interlayers are inserted through the thickness of the films. The label above each multilayer structure corresponds to the total number of bilayer pairs.

After identifying the optimal multilayer structure using the strategy described in Figure 2.17, we use the same multilayer structure to insert an insulating interlayer of Al_2O_3 with a thickness of 2.5 nm. Note that the order of the Al_2O_3 interlayer insertion always follows the FeGa layer – this is to ensure the FeGa always grows on an optimal underlayer material and preserve the underlayer effect throughout the thickness of the multilayer stack.

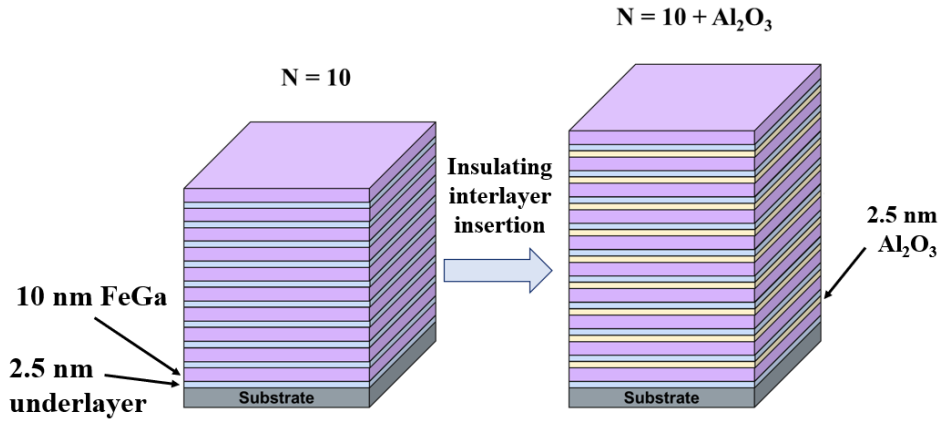

Figure 2.18: Schematic of the strategy to add insulating interlayers of Al_2O_3 (2.5 nm thickness) after each FeGa/NiFe bilayer. The case of a 10 FeGa/NiFe bilayer sample is shown.

2.4 Computational Methods

2.4.1 Density Functional Theory

Density functional theory (DFT) is a quantum mechanics based first principles model used to investigate the structural and electronic properties of a given configuration of atoms. Underlying this theory is the assumption that electrons and nuclei are the fundamental building blocks of matter. The main principle behind DFT is that the energy of a system is a unique functional of the charge density distribution. The only inputs required to successfully carry out a DFT calculation are the positions and the identities of the constituting atoms, thereby, rendering it to a parameter free computational method. Today, DFT-based quantum mechanical solutions are established to accurately define atomic level interactions in diverse chemical environments, at practically feasible computational costs. DFT formalism converts a many-nuclei, many-electron problem to an effective one electron problem. This was realized in the pioneering work of Hohenberg, Kohn and Sham (Hohenberg and Kohn 1964, Kohn and Sham 1965). Within the Kohn-Sham DFT formalism, the following eigenvalue relation is solved:

$$\left[\boldsymbol{\nabla^2} + \boldsymbol{V_{eff}(r)}\right]\boldsymbol{\psi_i(r)} = \boldsymbol{\epsilon_i \psi_i(r)} \tag{2.5}$$

where $\boldsymbol{\nabla^2}$ represents the electronic kinetic energy and $\boldsymbol{V_{eff}(r)}$ represents the effective potential energy as experienced by an electron. The latter contains all the electron-electron and electron-nucleus interactions, as well as the potential caused by any external electric field. The quantum mechanical part of the electron-electron interaction is not exactly known and in practice is approximated using a local functional within the local density approximation (LDA), a semi-local functional within the generalized gradient approximation (GGA), or nonlocal hybrid functionals. Additionally, $\boldsymbol{\epsilon_i}$ and $\boldsymbol{\psi_i}$ are the energy eigenvalues and wave-functions of the Kohn-Sham orbitals.

For a given set of atomic positions, the above equation is solved self-consistently to result in converged charge densities (obtained from the wave functions of the occupied states), total energies (obtained from the wave functions and eigen energies of the occupied states) and atomic forces (obtained from the first derivatives of the total energy with respect to the atomic positions). The obtained forces are utilized to update atomic coordinated during relaxation of a structure.

2.4.2 DFT parameters

The implementation of DFT in this work was done using the Vienna Ab Initio Simulation Package (VASP) (Kresse and Furthmüller 1996) employing the Perdew-Burke-Ernzerhof GGA exchange-correlation functional (Perdew, Burke et al. 1996) and the projector-augmented wave (PAW) methodology (Blöchl 1994). Standard VASP PAW potentials were used where the 2*s* and 2*p* electrons for O and the 5*s*, 5*p*, 6*s*, and 5*d* electrons for Hf are treated self-consistently.

For the calculation of bulk HfO_2 structures in this work, a basis set that includes all the plane waves with kinetic energies up to 800 eV was used and a *k*-point density of ~0.05 / Å in the reciprocal space using a Monkhorst-Pack grid. The optimal kinetic energy and *k*-point density was calculated based on the four-formula-unit orthorhombic HfO_2 shown in Figure 2.9(b). For this structure, the cell volume and the atomic degrees of freedom were relaxed until atomic forces are smaller than 0.001 eV/ Å as a function of the *k*-point density at a kinetic energy cutoff of 1000 eV and as a function of kinetic energy cutoff at a *k*-point density of ~0.02 / Å. The ultimate choice of *k*-point density and kinetic energy cutoff was chosen based on total energy convergence below 1 meV/atom. For the orthorhombic structure shown in Figure 2.19(b), the equilibrium lattice parameters obtained were a = 5.274 Å, b = 5.056 Å, c = 5.086 Å, and $\alpha, \beta, \gamma = 90°$. For reference, the higher symmetry tetragonal phase that is parent to the orthorhombic phase is shown in Figure

2.9a) which has equilibrium lattice parameters of: a = b = 5.082 Å, c = 5.230 Å, and α, β, γ = 90°. An example of a script of an INCAR file used as an input for VASP calculations of the bulk properties is shown in the appendices.

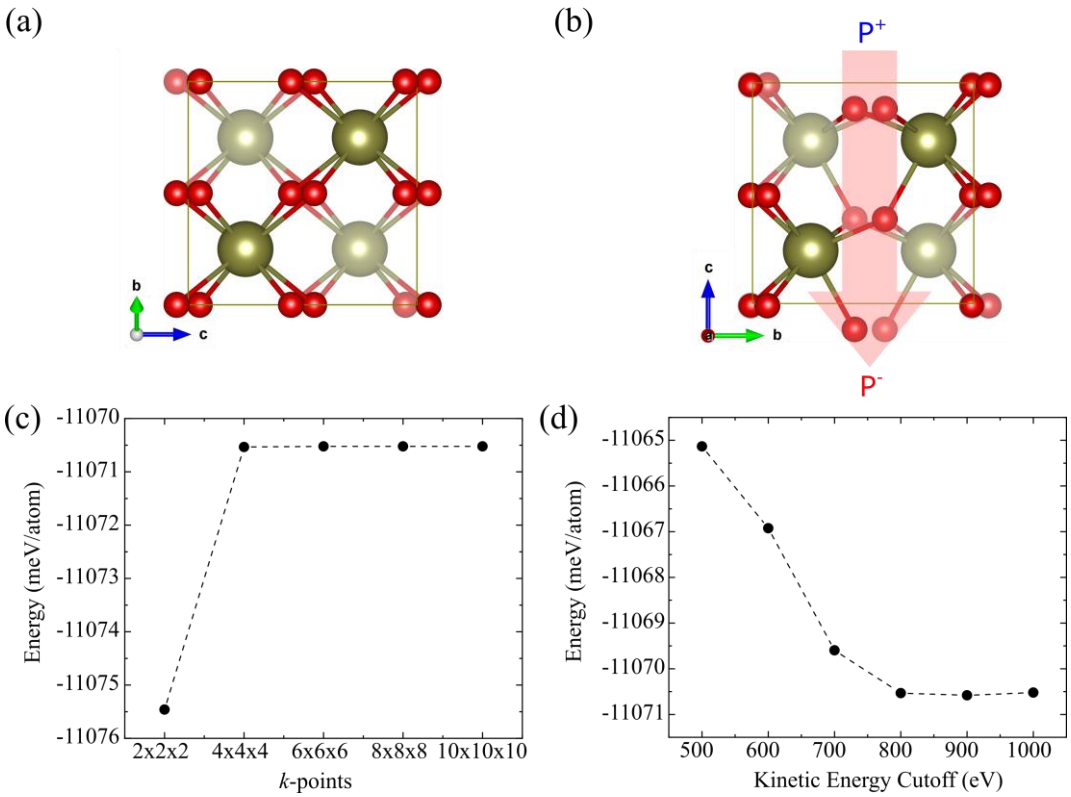

Figure 2.19: Structure of the bulk four-formula-unit supercell of (a) the nonpolar tetragonal ($P4_2/nmc$) phase and (b) the polar orthorhombic ($Pca2_1$) HfO_2 phase. The polarization vector is along the c axis [001] direction, as indicated by the overlaid arrow. Hf and O atoms are shown as green (large) and red (small) spheres, respectively. Total energy for the bulk four-formula-unit orthorhombic HfO_2 structure as a function of the (b) *k*-point density in a Monkhorst-Pack grid using a 1000 eV planewave kinetic energy cutoff and (c) the planewave kinetic energy cutoff using a 10x10x10 *k*-point density in a Monkhorst-Pack grid. The total energy convergences are both ~0.01 meV/atom for the 4×4×4 relative to the 10×10×10 *k*-point mesh and for the 800 eV relative to the 1000 eV kinetic energy cutoff.

To study the surfaces of HfO_2 and corresponding energetics, HfO_2 slab supercell structures were constructed composed of ~ nine formula units of HfO_2 layers (17–19 Hf and O "half-layers": here, we define a full layer to consist of an Hf half-layer and an O half-layer) along the surface

normal direction. Figure 2.20 shows the profile of the initial slab supercell structures for the corresponding nonpolar tetragonal and polar orthorhombic phases constructed initially from their relaxed bulk tetragonal and orthorhombic structures shown in Figure 2.20(a) and (b). Each half-layer consists of either two Hf or four O atoms, except for the outermost surface layers. The surface area of each side of the slabs corresponds to two bulk formula units. We also introduced a vacuum width of ~15 Å along the surface normal direction. An example of a script of an INCAR file used as an input for the VASP calculations for the total energy and ionic relaxation of the slab models is shown in the Appendices.

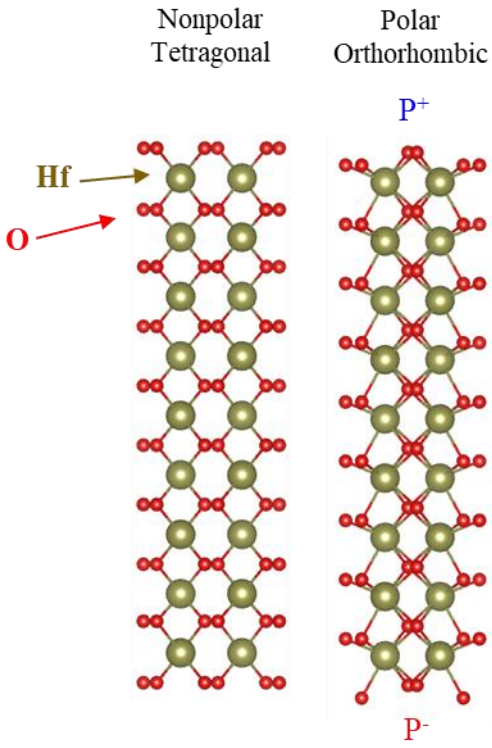

Figure 2.20: Profile view of nonpolar tetragonal (left) and polar orthorhombic (right) slab models consisting of 9 layers constructed from the bulk phases shown in Figure 2.19(a) and (b). P+ and P- labels denote the directions of polarization for the polar slab. Green atoms: Hf, red atoms: O.

A rotated profile perspective and a top and bottom view of the surfaces of the slabs from Figure 2.20 is shown in Figure 2.21. The surface views are shown to visualize the description of the nomenclature. For example, for the nonpolar slab, there are a total of 4 oxygen atoms within a single unit cell periodic boundary at the top and bottom surface. Thus, we divide the 4 O by 2 (corresponding to the fact that there are two formula units per unit surface cell) to arrive at 2.0-O/surface-formula-unit. Since there are two surfaces, and we later construct models with asymmetrically terminated surfaces, we further use the nomenclature of 2.0-O/2.0-O to describe the surface composition of the two surfaces (which are equivalently terminated in this case).

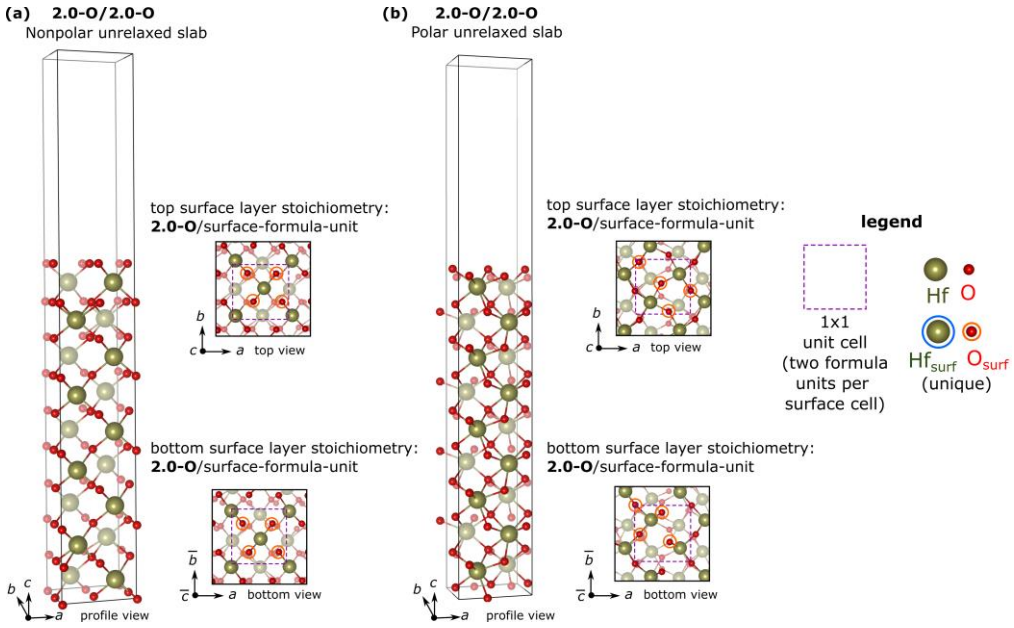

Figure 2.21: (a) Top and bottom surface views of the unrelaxed nonpolar tetragonal 2.0-O/2.0-O slab, profile is rotated compared to the same slab in Figure 2.19(a). (b) top and bottom surface views of the unrelaxed polar orthorhombic 2.0-O/2.0-O slab, profile is rotated compared to the same slab in Figure 2.19(b). The nomenclature refers to the composition of the surface termination per surface-formula-unit. Legend (right) is used to show the perimeter of a single surface cell. Outermost atoms are circled in (a) and (b) as noted in the legend.

To compare the relative thermodynamic stability of the surfaces that can be constructed from Figure 2.20 we can formulate an expression for the surface energy based on the derivation for a transition metal oxide discussed in prior bodies of work, e.g. see ref. (Reuter and Scheffler 2001), where we first define an average surface free energy (top and bottom surfaces) using the Gibbs free energy of a slab, $\boldsymbol{G^{slab}(T, p, N_{Hf}, N_O)}$:

$$\boldsymbol{\gamma_{average} = \frac{1}{2A}\left(G^{slab}(T, p, N_{Hf}, N_O) - N_{Hf}\mu_{Hf}(T, p) - N_O\mu_O(T, p)\right)} \tag{2.6}$$

where N_{Hf} and N_O are the numbers of Hf and O atoms in the slab supercell, $\boldsymbol{\mu_{Hf}}$ and $\boldsymbol{\mu_O}$ are the chemical potentials of Hf and O atoms in the reservoir (environment), and A is the surface area of one side of the slab. Because the bulk phase must be in equilibrium with the chemical reservoirs in order to exist, the Gibbs free energy of bulk HfO_2 must be: $\boldsymbol{g^{bulk}_{HfO_2}(T, p) = \mu_{Hf}(T, p) + 2\mu_O(T, p)}$. Substituting $\boldsymbol{g^{bulk}_{HfO_2}(T, p) - 2\mu_O(T, p)}$ for $\boldsymbol{\mu_{Hf}(T, p)}$ in the $\boldsymbol{\gamma_{average}}$ expression above, we have a surface energy expression that depends only on the chemical potential of O:

$$\boldsymbol{\gamma_{average} = \frac{1}{2A}\left(G^{slab}(T, p, N_{Hf}, N_O) - N_{Hf}g^{bulk}_{HfO_2}(T, p) - (N_O - 2N_{Hf})\mu_O(T, p)\right)} \tag{2.7}$$

We approximate the free energies of the bulk and the slabs using only DFT-PBE energies. This is because we expect that the vibrational free energy contributions from the bulk and surface mostly to cancel out. The chemical potential of oxygen, $\boldsymbol{\mu_O(T, p)}$, can be expressed by the following Gibbs-Duhem equation for an ideal gas:

$$\boldsymbol{\mu_O(T,p) = \frac{1}{2}\mu_{O_2}(T,p) = \frac{1}{2}\mu_{O_2}(T,p^\circ) + \frac{1}{2}kTln\left(\frac{p}{p^\circ}\right)} \quad (2.8)$$

where $\boldsymbol{\mu_{O_2}}$ is the chemical potential of the O_2 gas and we need to find the temperature dependence of $\boldsymbol{\mu_O(T,p)}$ at a particular partial pressure of O_2 ($\boldsymbol{p}$, with $\boldsymbol{p^\circ}$ = 1 bar). In this case, we chose the reference state of $\boldsymbol{\mu_O(T,p^\circ)}$ with respect to an isolated (gaseous) O_2 molecule:

$$\boldsymbol{\mu_O(T,p^\circ) = \frac{1}{2}\mu_{O_2}(T,p) = \frac{1}{2}[\{H(T,p^\circ,O_2) - H(0\ K,p^\circ,O_2)\} - TS(T,p^\circ,O_2)]}$$

$$\boldsymbol{\left[\nabla^2 + V_{eff}(r)\right]\psi_i(r) = \epsilon_i\psi_i(r)} \quad (2.9)$$

We express $\boldsymbol{H(0\ K,p^\circ,O_2)}$ as:

$$\boldsymbol{H(0\ K,p^\circ,O_2) = 2\left(E_0^{DFT} - \Delta E_{f,O}(0\ K,p^\circ)\right)}$$

$$\boldsymbol{\left[\nabla^2 + V_{eff}(r)\right]\psi_i(r) = \epsilon_i\psi_i(r)} \quad (2.10)$$

where $\boldsymbol{E_0^{DFT}}$ and $\boldsymbol{\Delta E_{f,O}(0\ K,p^\circ)}$ are respectively the DFT energy of an O atom in vacuum (in a periodic asymmetric 8.0 × 7.5 × 7.0 $\boldsymbol{Å^3}$ box to obtain the ^{3}P ground state) and the empirically extrapolated formation energy of an O atom from O_2 at 0 K and 1 bar. The DFT-PBE binding error for O_2 can be as large as ~ 0.9 eV/O_2 (Perdew, Burke et al. 1996), therefore requiring an empirical correction to the simulation of an isolated O atom in DFT instead. To calculate $\boldsymbol{H(T,p^\circ,O_2) - H(0\ K,p^\circ,O_2)}$, we first use the tabulated data for the reference enthalpy of O_2 at 1 bar for 0 K and 298 K to obtain $\boldsymbol{H(298\ K,p^\circ,O_2) - H(0\ K,p^\circ,O_2)}$ (Darwent 1970), and then used the Shomate equation to determine the enthalpy at *T* relative to 298 K:

$$H(T, p^\circ, O_2) - H(298\ \mathrm{K}, p^\circ, O_2) = AT + {BT^2}/{2} + {CT^3}/{3} + {DT^4}/{4} - {E}/{T} + F - H \quad (2.11)$$

where Table 2.2 displays the constants A to H for 100 – 700 K and 700 – 1000 K (taken from Ref. (Chase 1996)). Hence:

$$(T, p^\circ, O_2) - H(0\ \mathrm{K}, p^\circ, O_2) = [H(T, p^\circ, O_2) - H(298\ \mathrm{K}, p^\circ, O_2)] + [H(298\ \mathrm{K}, p^\circ, O_2) - H(0\ \mathrm{K}, p^\circ, O_2)] \quad (2.12)$$

Similarly, for $S(T, p^\circ, O_2)$ we used the Shomate equation:

$$S(T, p^\circ, O_2) = A \ln T + BT + {CT^2}/{2} + {DT^3}/{3} - {E}/{2T^2} + G \quad (2.13)$$

using the same above-mentioned constants and an additional constant G (also shown in Table 2.2).

Table 2.2: Constants in the Shomate equations used to evaluate the enthalpy (H) and entropy (S) of O_2 over various temperature ranges. These constants correspond to units of kJ/mol and J/K-mol for H and S, respectively, using the equations in the main text, where T is in K.

Temp. (K)	A	B	C	D	E	F	G	H
100-700	31.3223	-20.235	57.866	-36.506	-0.0074	-8.904	246.80	0
700-1000	30.0324	8.7730	-3.9881	0.7883	-0.7416	-11.33	236.17	0

Note that in Chapter 5, the calculated surface energies use the equation for $\gamma_{average}$ applied only to the slab model surfaces after ionic relaxation.

2.5 Summary

Addressing the materials integration challenges for ferromagnetic FeGa and ferroelectric HfO_2-based thin films requires different sets of analysis. The soft magnetic properties of FeGa films are influenced by factors at the microstructural level and experimental techniques like XPS, XRD, SQUID, and FMR spectroscopy are well suited to study the microstructural and macroscopic magnetic thin film properties. On the other hand, DFT is well suited to systematically explore the influence of the structural and electronic properties of the surface that cannot be easily controlled or accessed through experiment, and thus is instrumental towards the goal of isolating the effect of the surface composition and its influence on the surface energy to stabilize the ferroelectricity in HfO_2 thin films.

Chapter 3 Underlayer Effect on the Soft Magnetic Properties of FeGa Thin Films

To isolate and identify the influence of NiFe on the soft magnetic properties of FeGa in composite FeGa/NiFe multilayers, we studied the influence of a single thin NiFe underlayer compared to Ta, Cu, and no underlayer on the growth of 100 nm FeGa thin films. The films deposited with an underlayer showed increased in-plane uniaxial anisotropy and a decrease in in-plane coercivity. The smallest coercivity was observed in FeGa deposited with a NiFe underlayer at 15 Oe, compared to 84 Oe for films deposited directly on Si. In addition, an effective Gilbert damping coefficient as low as 0.044 was achieved for a 100 nm FeGa film with a NiFe underlayer. The FeGa films were also able to retain or increase their saturation magnetostriction when deposited on an underlayer. This led to an increase in the piezomagnetic coefficient from 1.2 ppm/Oe to 8.3 ppm/Oe. This enhancement is attributable to the impact of the underlayer to promote an increased (110) film texture and smaller grain size, which is correlated to the lattice match of the underlayer of the sputtered FeGa film.

3.1 Effect of underlayers on the static magnetic properties of FeGa thin films

3.1.1 Magnetic hysteresis

Figure 3.1 shows the in-plane magnetic hysteresis loops for the 100 nm FeGa films deposited on different underlayer materials normalized to the saturation magnetization. All the films exhibited strong in-plane magnetic anisotropy. The FeGa film deposited directly onto a Si substrate, without an underlayer, showed a coercivity of 84 Oe. The coercivity of FeGa was reduced to 54 Oe when deposited onto a 2.5 nm Ta underlayer and further decreased to 17 and 15 Oe when deposited on 2.5 nm Cu and NiFe underlayers, respectively. These results follow a similar trend to that previously observed for $Fe_{65}Co_{35}$ films where a Ta underlayer resulted in a modest

decrease in easy-axis coercivity while Cu and NiFe underlayers promoted a larger decrease (Jung, Doyle et al. 2003). In addition, the FeGa films deposited with both Cu and NiFe underlayers displayed an enhanced uniaxial anisotropy, as observed from the increase in remnant magnetization. These trends are summarized in Table

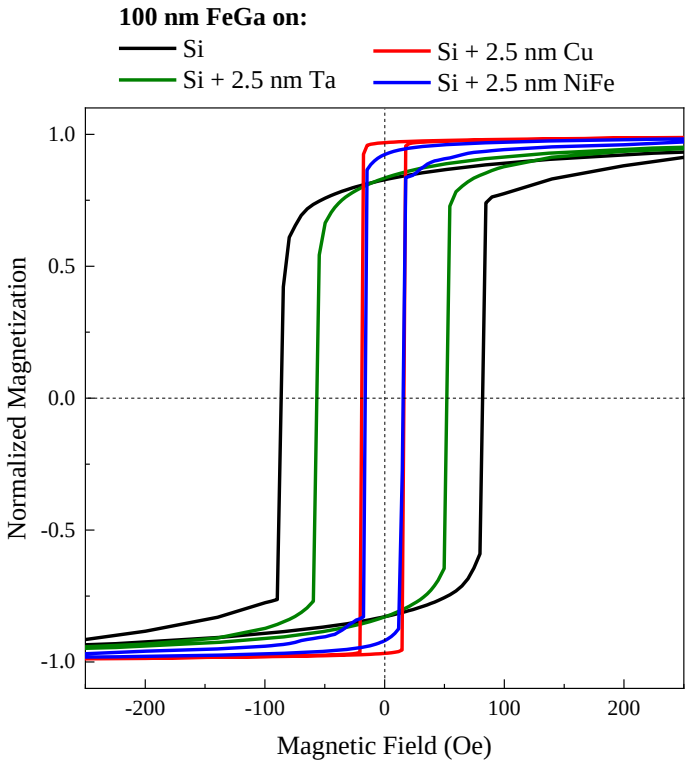

Figure 3.1: Normalized in-plane magnetic hysteresis loops of 100 nm FeGa sputtered on a Si substrate with different underlayer materials.

3.1.2 High frequency magnetic absorption

The high frequency characteristics of FeGa films deposited with different underlayers were studied using broadband FMR spectroscopy. Figure 3.2 shows the s_{11} absorption as a function of the magnetic bias field (0–600 Oe) at a fixed frequency of 6 GHz. For a 100 nm FeGa film

deposited without an underlayer, the FMR spectra are characterized by a very low peak absorption (∼0.3%) and very broad FMR linewidth (>600 Oe at 6 GHz) that extends beyond the maximum magnetic field applied. For an FeGa film deposited with a Ta underlayer, a small enhancement in the FMR linewidth (∼465 Oe at 6 GHz) can be observed. In contrast, the FeGa films deposited on a Cu or a NiFe underlayer were characterized by a dramatic enhancement in the FMR response with linewidths decreasing to as low as ∼178 Oe and ∼160 Oe at 6 GHz, respectively.

The effective Gilbert damping coefficient, α_{eff}, was calculated by fitting the FMR linewidth of the absorption as a function of frequency for the entire FMR spectra in Figure 3.2 as described in Chapter 2. The values are listed in Table 3.1. The FeGa films deposited with Cu and NiFe underlayers show a significant decrease (∼75%–78%) in their effective Gilbert damping coefficient compared to an FeGa film without an underlayer.

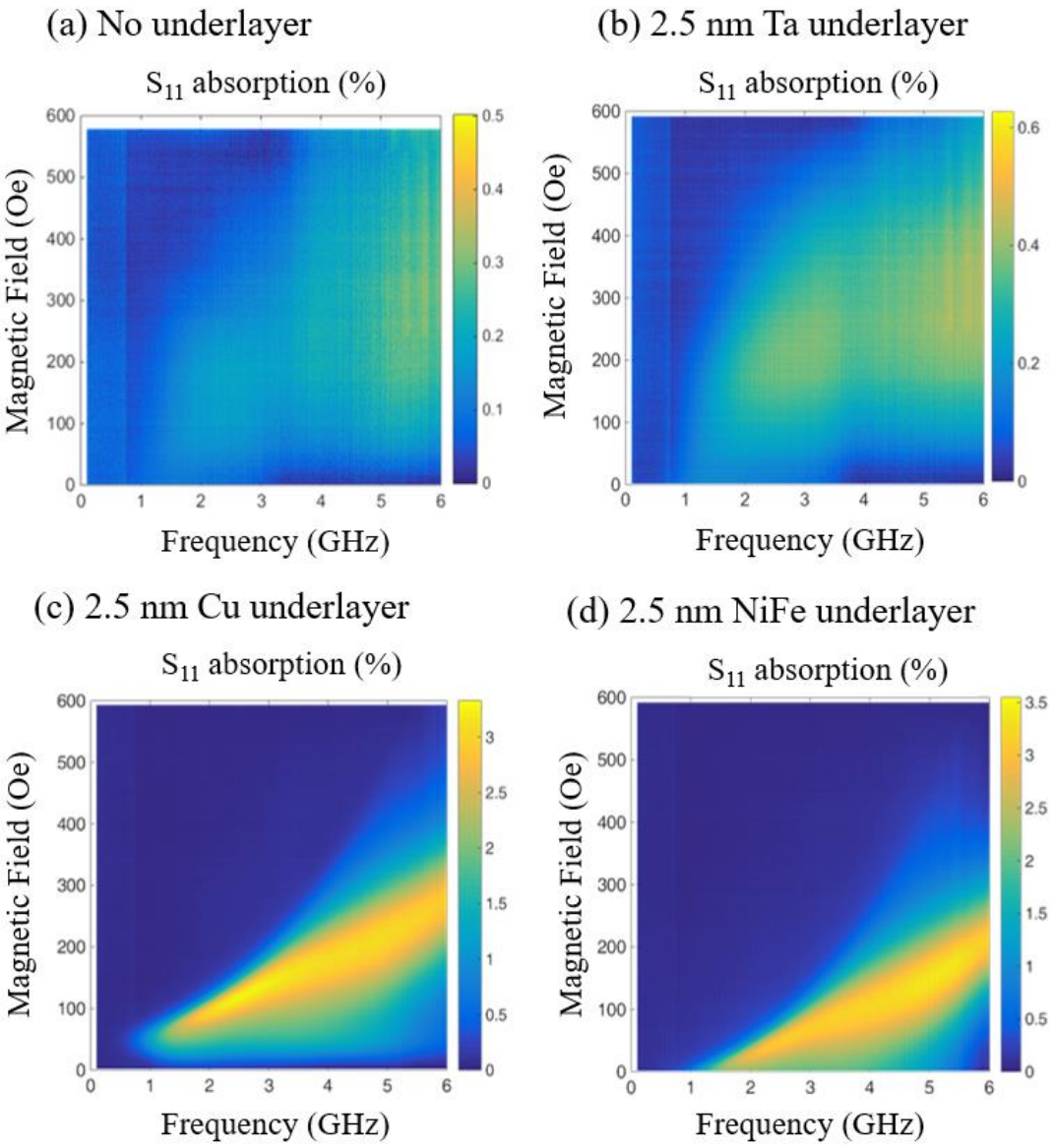

Figure 3.2: FMR absorption spectra as a function of both frequency (100 MHz - 6 GHz) and magnetic bias (0 - 600 Oe) for 100 nm FeGa sputtered on the following: (a) Si only, (b) Si + 2.5 nm Ta underlayer, (c) 2.5 nm Cu underlayer, (d) Si + 2.5 nm NiFe underlayer.

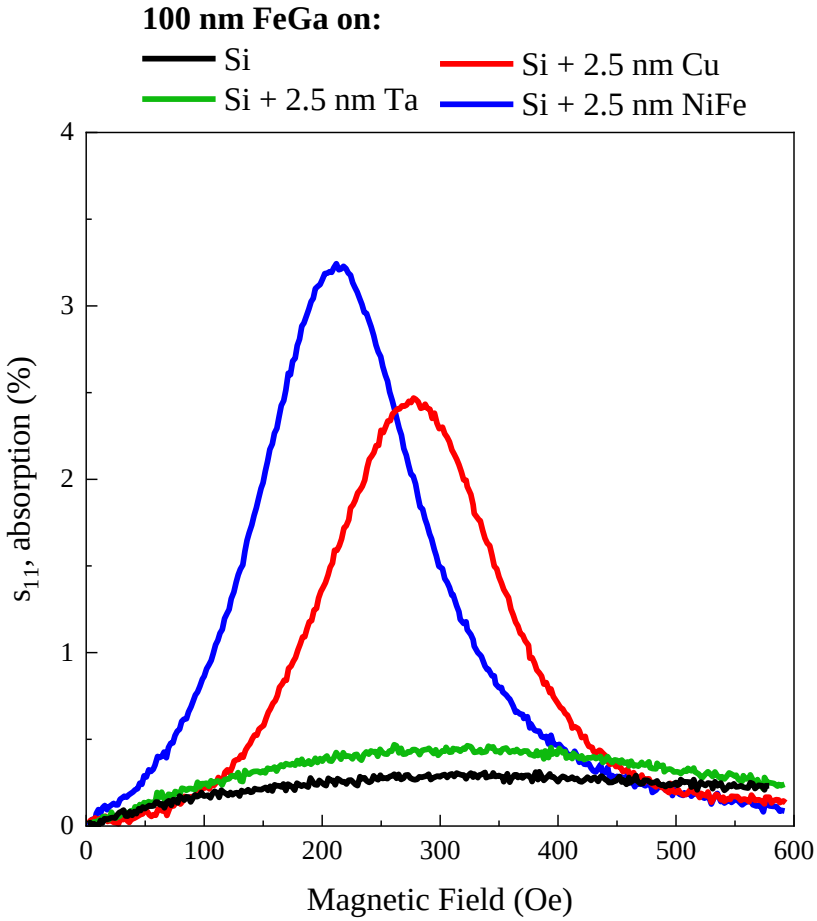

Figure 3.3: FMR absorption spectra as a function of magnetic bias field at 6 GHz for 100-nm FeGa films sputtered on a 2.5 nm underlayer of different materials (Ta, Cu, and NiFe).

3.2 Effect of underlayers on the microstructure of FeGa thin films

The enhanced soft magnetic properties of the FeGa films grown on the Cu and NiFe underlayers must originate from the impact of the underlayer on its microstructure. This was studied using XRD and AFM imaging.

3.2.1 Crystalline structure

Structural characterization of the FeGa films grown on the different underlayers was first investigated with XRD. All of the FeGa films all show primarily a bcc (110) diffraction as the strongest diffraction line. Figure 3.4 shows the spectra highlighting the bcc (110) diffraction for a 100 nm FeGa film without an underlayer compared to FeGa sputtered on Ta, Cu, and NiFe underlayers. The films deposited onto Cu and NiFe underlayers, which show the largest enhancement in their soft magnetic properties, also display a large shift of the (110) diffraction line position which is caused by relative change in the internal stress of the films. The shift in peak position represents a relative decrease of 0.28% and 0.21% tensile strain for the FeGa films on Cu and NiFe underlayers, respectively, compared to FeGa deposited directly onto a Si substrate.

The FeGa films deposited on the Cu and NiFe underlayers show an increase (~30%) in the intensity of their (110) diffraction peak compared to Ta or no underlayer, indicating an increased (110) polycrystalline texture. This enhancement can be attributed to the close lattice match of the FeGa (110) (d = 2.06 Å) film texture during growth to the underlying Cu (111) (d = 2.09 Å) and NiFe (111) (d = 2.05 Å) film texture and is highlighted in Figure 3.5. In contrast to Cu and NiFe, Ta exhibits a preferential β-(002) diffraction at 33.7° (d = 2.66) that has a poor lattice match with FeGa.

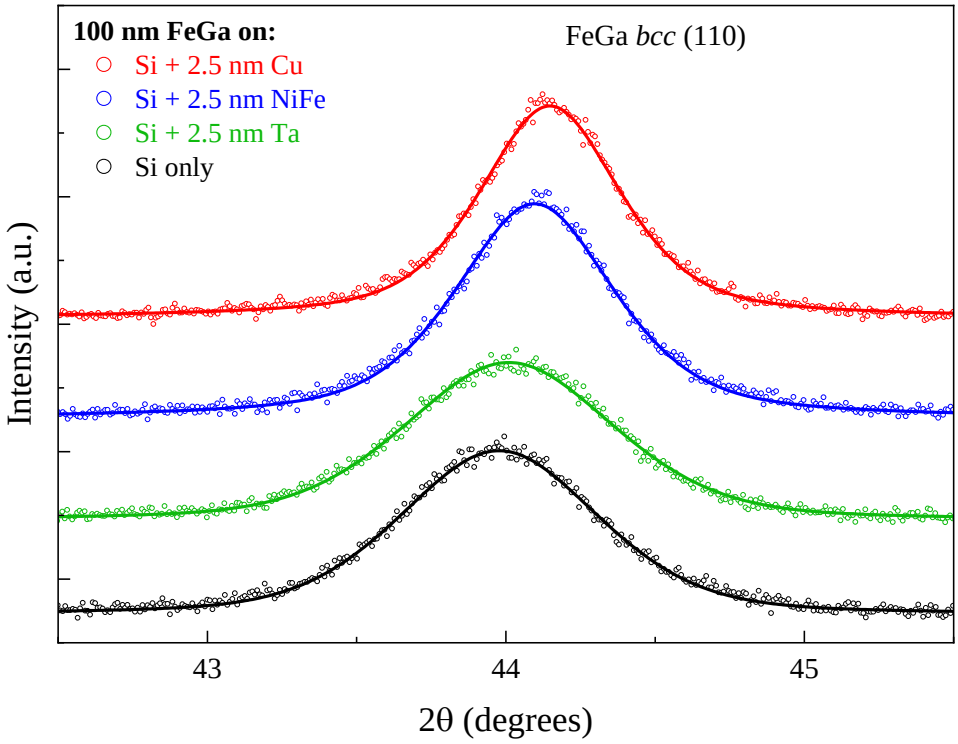

Figure 3.4: XRD spectra of the main bcc (110) FeGa peak when grown on different underlayer materials. Solid lines are the best Voigt fit of the data in circles. Vertical dashed lines are used to highlight the shift in the (110) peak across samples.

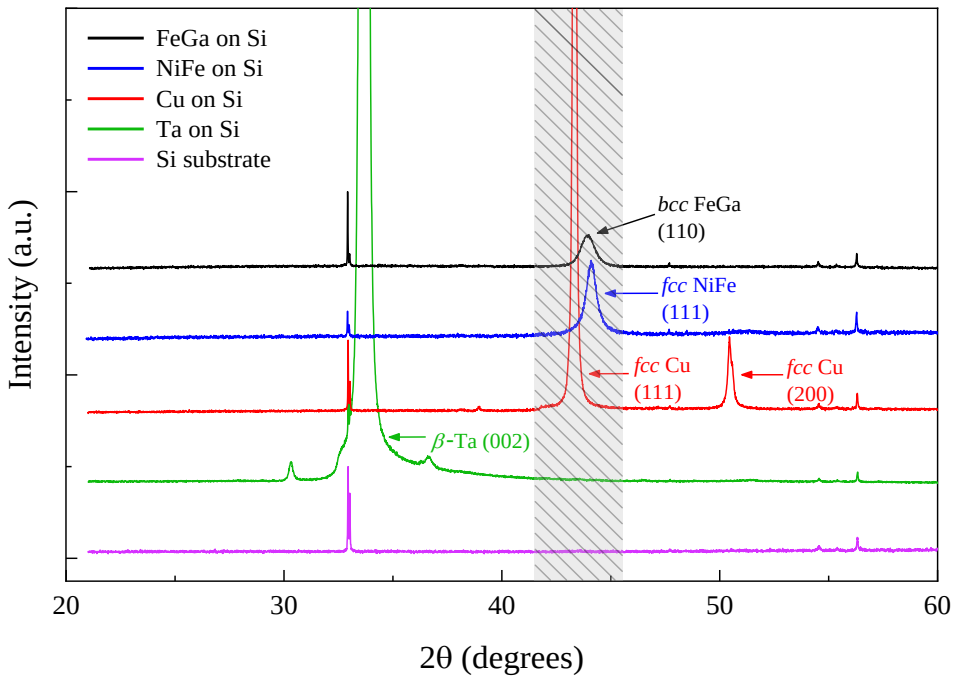

Figure 3.5: XRD spectra of a Si substrate alone and the following films (~100 nm thickness) on Si: Ta, Cu, NiFe, FeGa. Highlighted area is used to show close lattice match of main Cu & NiFe diffraction peaks to FeGa.

3.2.2 Surface topography

AFM imaging was used to probe the differences in the microstructure of the FeGa films that can appear in their surface morphology when grown on the different underlayers. Figure 3.6 shows 1 μm×1 μm AFM images of the FeGa films deposited on the various underlayers. The surface roughness remained in the range of 1.1-1.4 nm for FeGa films deposited with and without the underlayers. More importantly, it can be observed that the magnetically softer FeGa films deposited on Cu & NiFe underlayers exhibit a smaller and more uniform grain width (D) distribution (29 ± 7 nm & 29 ± 6 nm, respectively) than the magnetically harder FeGa samples deposited directly on Si or with a Ta underlayer (46 ± 23 nm & 39 ± 14 nm, respectively)

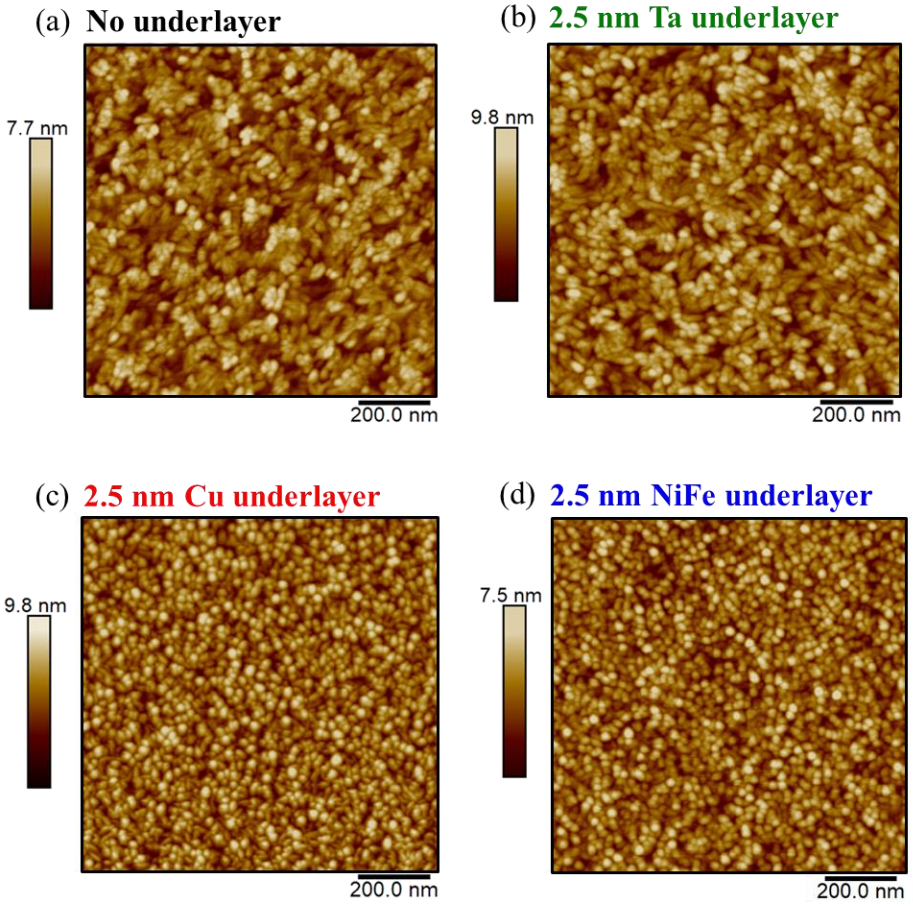

Figure 3.6: AFM of ~100 nm FeGa films grown (a) directly on Si, (b) with a 2.5 nm Ta underlayer, (c) with a 2.5 nm Cu underlayer, (d) with a 2.5 nm NiFe underlayer

Table 3.2: Table Summary of in-plane coercivity, normalized remnant magnetization (M_r/M_s), Gilbert damping coefficient (α), relative change in 110 peak intensity (ΔI_{110}), and average grain width (D) for 100-nm FeGa grown on different underlayer materials on a Si substrate.

Underlayer	In-plane coercivity (Oe)	M_r/M_s	α	ΔI_{110} (%)	D (nm)
None	83	0.83	0.21	-	46 ± 23
2.5 nm Ta	54	0.84	0.12	-0.01	39 ± 14
2.5 nm Cu	17	0.97	0.053	30	29 ± 7
2.5 nm NiFe	15	0.92	0.044	29	29 ± 6

3.3 Magnetoelastic properties of FeGa thin films with NiFe and Cu underlayers

In order to obtain magnetostriction measurements for FeGa films with different underlayers, an optical cantilever set-up was used as shown in the schematic in Chapter 2. From the data in Figure 3.7, the FeGa film deposited without an underlayer reaches a maximum magnetic field induced stress of 7.4 MPa. The film grown on the Cu underlayer largely maintains the same magnetostriction, displaying a maximum magnetic field induced stress of 7.2 MPa. Interestingly, the FeGa film grown on the NiFe underlayer shows a 27% increase in the saturation stress, reaching 9.4 MPa.

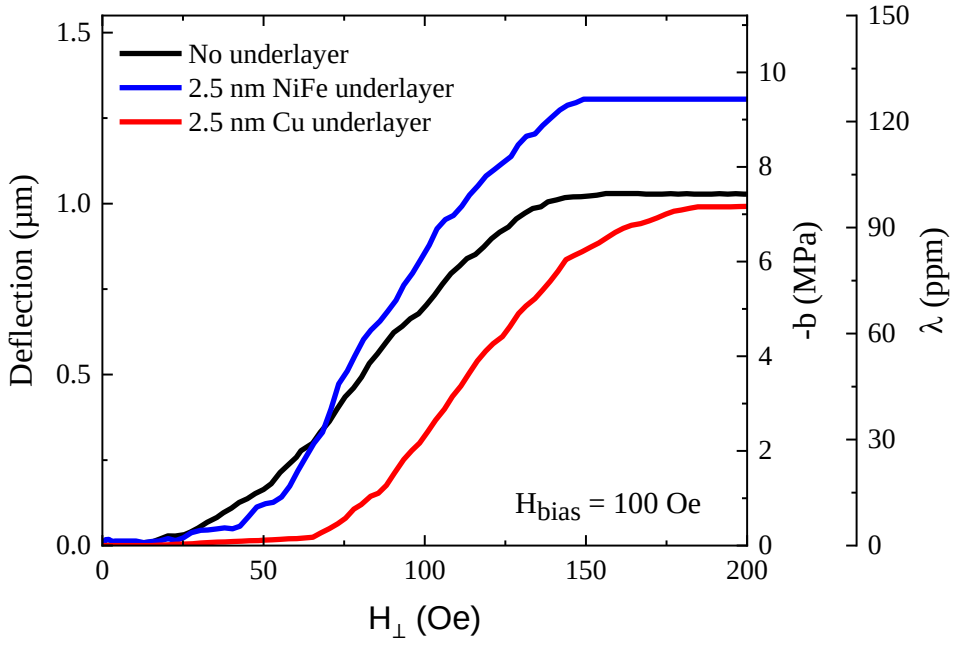

Figure 3.7: (Left axis) Cantilever deflection calculated for ~100 nm FeGa sputtered directly on Si and on NiFe and Cu underlayers as a function of the AC magnetic field (along the short axis of cantilever sample). (Right axis: b) Stress calculated from the cantilever deflection. An initial bias field of 100 Oe was applied to saturate the magnetization along the long axis of the cantilever sample and held constant during the measurement. (Right axis: λ) Stress calculated from the cantilever deflection. An initial bias field of 100 Oe was applied to saturate the magnetization

along the long axis of the cantilever sample and held constant during the measurement.

3.4 Summary

To enhance the soft magnetic properties of sputtered FeGa thin films, a strategy of using a thin 2.5 nm underlayer as a buffer between the growth of an FeGa film and a Si substrate was explored. It was found that an ~80-82% decrease in coercivity and ~75-78% decrease in Gilbert damping coefficient for 100-nm of sputtered FeGa on Si can be achieved using the optimal Cu and NiFe underlayer materials. It is observed that underlayer serves to influence the microstructure of the FeGa films, resulting in an increased (110) polycrystalline texture, smaller grain size, and an increase in compressive film strain for FeGa deposited on Cu and NiFe underlayers. We also observe that the saturation magnetostriction is maintained for the FeGa films grown with a Cu underlayer and displays a 27% increase with a NiFe underlayer. This led to an increase in the piezomagnetic coefficient from 1.2 ppm/Oe to 8.3 ppm/Oe. The use of a thin underlayer material is this shown to be a useful strategy to enhance the soft magnetic properties of FeGa thin films.

Chapter 4 Process development of FeGa/NiFe multilayer composite

To further optimize the soft magnetic properties of FeGa films, a multilayering approach that builds on the underlayer effect was explored. Multilayers where NiFe was used as an interlayer of constant 2.5 nm thickness while keeping the total volume of FeGa constant were fabricated. Additionally, the use of Al_2O_3 interlayers were used to improve the FMR absorption at high frequencies. Multilayer films consisting of 10 FeGa (100 nm) / NiFe (2.5 nm) bilayers showed increased in-plane uniaxial anisotropy (normalized remnant magnetization of 0.97), a decrease in in-plane coercivity (12 Oe), and a decrease in gilbert damping down to 0.014. A further decrease in coercivity was achieved in multilayers with a 2.5 nm Al_2O_3 interlayer added after the FeGa layer but before the NiFe layer. In addition, a Gilbert damping coefficient as low as 0.0081 was achieved for the 10 bilayer structure with Al_2O_3 interlayers.

4.1 Influence of Multilayering on Magnetic Hysteresis

Figure 1.1 shows the normalized in-plane magnetic hysteresis of multilayer FeGa/NiFe structures. The multilayer structures characterized in this section and their nomenclature were described in Chapter 2.

There is decrease in coercivity from 70 Oe for a single FeGa film to 20 Oe for an FeGa (100 nm) / NiFe (2.5 nm), or N = 1 bilayer structure. The samples consisting of N = 2 and N = 4 bilayers show an increase in the coercivity to 28 Oe and 25 Oe, respectively. The trend in decrease in coercivity continues for the N = 10 sample, which achieves a coercivity of 10 Oe. In parallel, we can see that the normalized remnant magnetization begins at 0.91 for a single FeGa film which increases to 0.93 for the N = 1 bilayer structure. The samples consisting of N = 2 and N = 4 bilayers show a decrease to 0.50 and 0.54, respectively. However, the N = 10 sample exhibits a normalized remnant magnetization of 0.97.

The N = 2 and N = 4 multilayer samples show a different magnetic anisotropy and hysteresis that doesn't follow a uniform trend with the other multilayer samples. This could be attributed to variations in the residual stress from variations from deposition to deposition in the sputtering chamber. Ultimately, the N = 10 multilayer sample shows the best combination of the highest remnant magnetic magnetization, indicative of a strong uniaxial anisotropy, and the lowest coercivity. The multilayer sample with N = 10 was thus chosen to determine the effect of adding Al_2O_3 insulating interlayers (FeGa/NiFe/Al_2O_3, N = 10 + Al_2O_3).

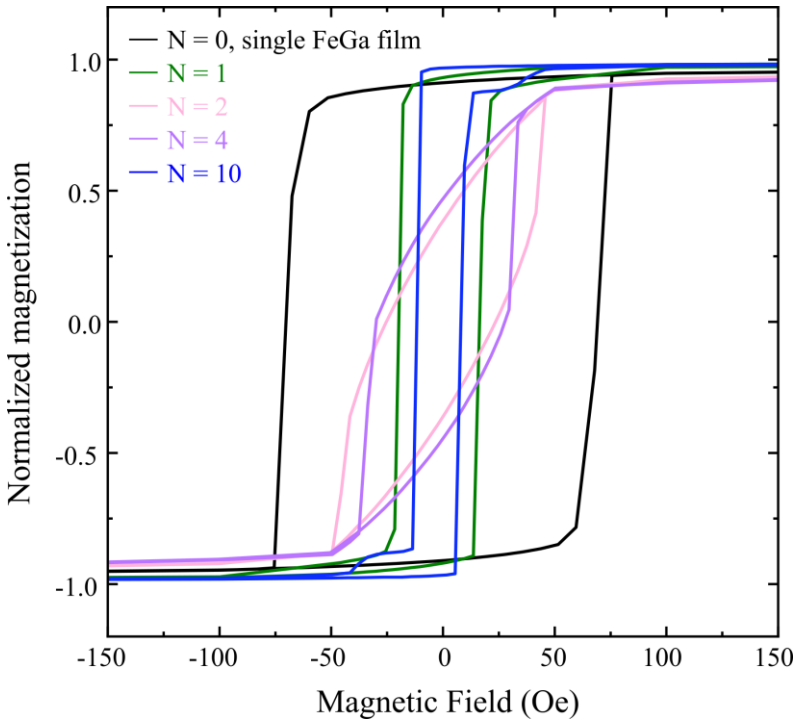

Figure 4.1: Normalized in-plane magnetic hysteresis loops comparing a single FeGa film (N=0) to multilayer FeGa/NiFe samples (N=1, 2, 4, 10). N refers to the total number of FeGa/NiFe bilayers, where the total volume of FeGa remains constant and the thickness of the individual NiFe layers is fixed at 2.5 nm.

The in-plane magnetic hysteresis of the N = 10 + Al_2O_3 sample is shown in Figure 4.2. The multilayer structure for the N = 10 + Al_2O_3 multilayer sample is shown in Figure 2.18. This sample shows coercivity that further reduces to 6 Oe from 10 Oe with the addition of Al_2O_3 insulating interlayers while retaining a strong uniaxial anisotropy. More critically, we are interested to identify the impact of the Al_2O_3 interlayers on the high frequency response.

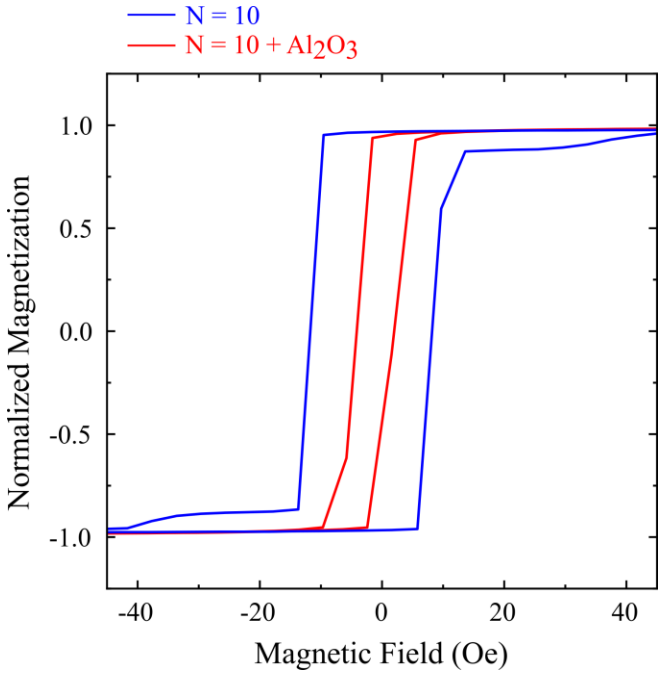

Figure 4.2: Normalized in-plane magnetic hysteresis loops comparing a 10 bilayer stack of FeGa/NiFe before and after the addition of a thin 2.5 nm Al_2O_3 interlayer insertion in each bilayer. N = 10 refers to the same sample in Figure 4.1 consisting of a stack of 10 bilayers of (10 nm FeGa/ 2.5 nm NiFe). N = 10 + Al_2O_3 refers to the multilayer stack consisting of 10 trilayers of (10 nm FeGa/ 2.5 nm NiFe/ 2.5 nm Al_2O_3).

4.2 First order reversal curves

Whereas conventional magnetic hysteresis curves give a picture of the macroscopic magnetic behavior of a material, first-order-reversal-curve analysis of magnetic hysteresis samples allow us to obtain further insight into the individual magnetic domain switching behavior.

In order to obtain a FORC diagram, a sample is initially prepared by saturating the magnetization. Starting from saturation at H_{sat}, the sample is prepared in a characteristic magnetization state by reducing the external magnetic field to the reversal field H_r. Then the first FORC is measured by detecting the sample's magnetization while increasing the external magnetic field back to its saturation value. This is repeated for gradually reduced reversal fields, i.e.,

different initial magnetization states at the beginning of each FORC. Thereby, the sample's magnetization $M(H_r, H_a)$ is obtained on a two-dimensional grid where each point is identified by H_r, the initial field at the beginning of each FORC, and H_a, the external magnetic field at which the data point was taken during the field sweep.

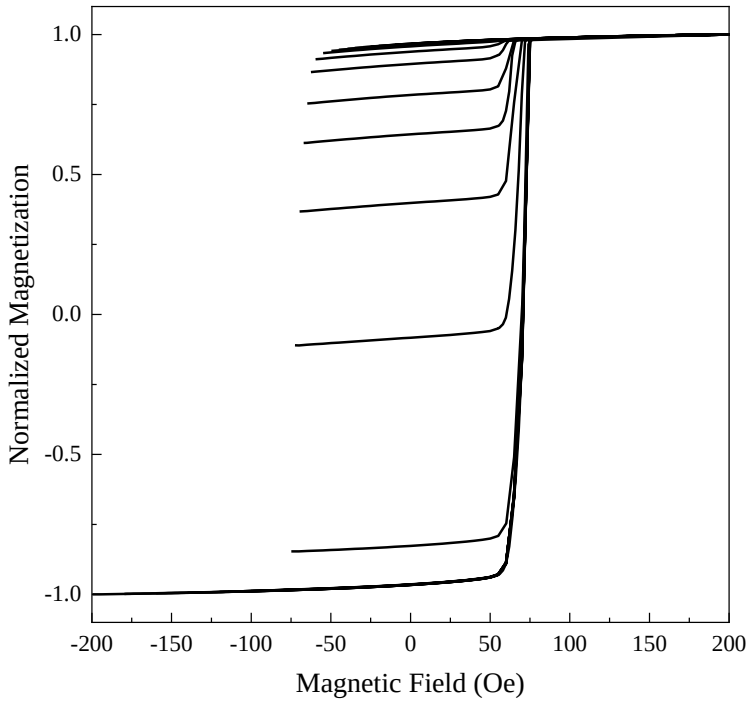

Figure 4.3: A set of FORC curves for a 100 nm FeGa film grown directly on a Si substrate.

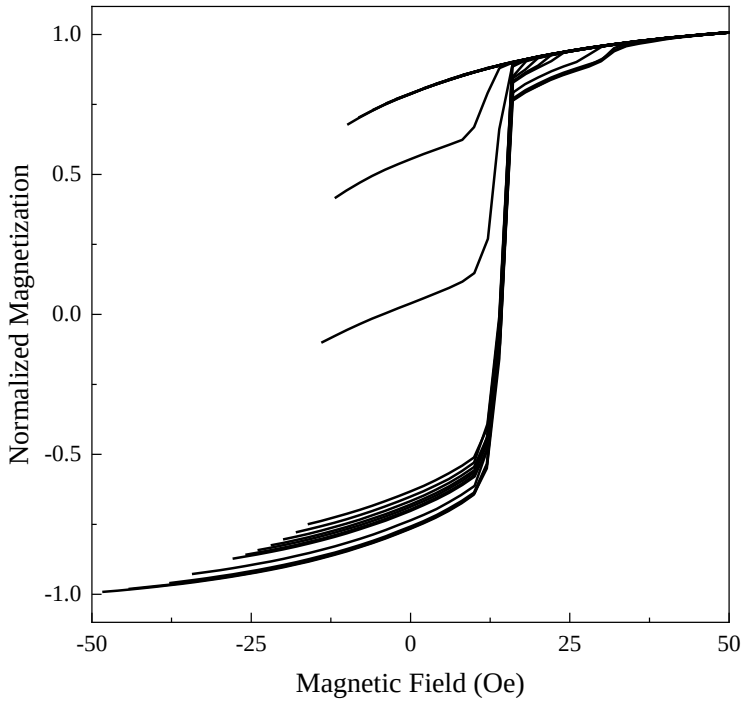

Figure 4.4: A set of FORC curves for a 10 bilayer multilayer film stack of (10 nm FeGa)/(2.5 nm NiFe) on a Si substrate.

A FORC diagram can then be obtained by the second-order mixed derivative of the data set. This transformation of the individual FORC curves shown in Figure 4.3 and Figure 4.4 to the FORC diagram shown in Figure 4.5 and Figure 4.6 is obtained by applying the transformation that:

$$\boldsymbol{\rho(H_r, H_a) = -\frac{1}{2}\frac{\partial^2 M(H_r, H_a)}{\partial H_r H_a}} \tag{4.1}$$

The final FORC diagram is shown in a rotated coordinate system by using the H_u- and H_c-axis, which are related to the H_r- and H_a-axis by $H_u = (H_a + H_r)/2$ and $H_c = (H_a - H_r)/2$. In this work, the software package doFORC (Cimpoesu, Dumitru et al. 2019) was used to transform the data to smooth the noise.

The broadening along the x-axis of Figure 4.5 and Figure 4.6 represent the distribution of coercive switching fields. The broadening is centered around a lower value for the multilayer FeGa/NiFe films compared to a single FeGa film which is expected since we know the macroscopic coercivity is lower (see Figure 4.1). More interestingly, it can be observed that the broadening decreases by ~55% for the multilayer FeGa/NiFe films compared to a single FeGa film which represents a more uniform rotation of magnetization.

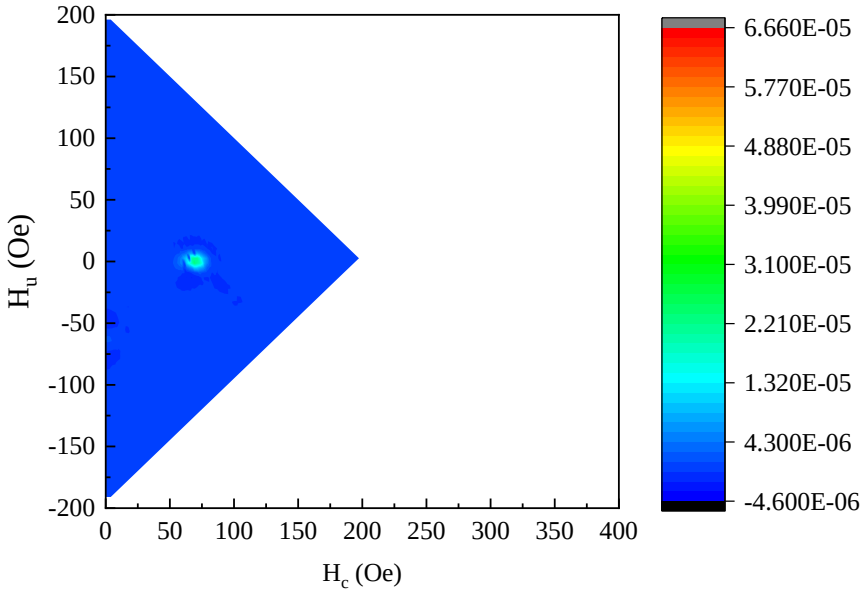

Figure 4.5: FORC diagram for the 100 nm FeGa film grown directly on a Si substrate shown in Figure 4.3.

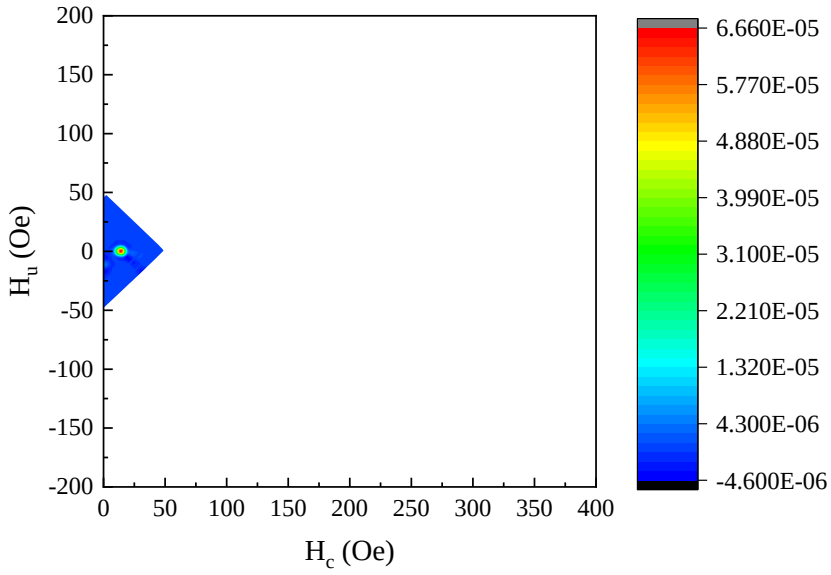

Figure 4.6: FORC diagram for a 10 bilayer multilayer film stack of (10 nm FeGa)/(2.5 nm NiFe) on a Si substrate.

4.3 Influence of Multilayering on High Frequency Properties

To further investigate the impact of multilayering on the high frequency properties, we examined the FMR absorption across multilayer samples. Figure 4.7 shows the FMR absorption for a single FeGa film, and the N = 1, 2, 4, and 10 multilayer structures that correspond to the same samples in Figure 4.1. It can be seen that the single FeGa film displays a spectra with poor absorption which is expected for a magnetically hard sample. The magnitude of the peak FMR absorption increases for the N = 1 bilayer structure sample, as expected for sample with a smaller coercivity and thus has a higher permeability. The sample with the highest magnitude of FMR absorption is the N = 10 multilayer structure, which also follows the trend of having a smaller coercivity correlating to a higher FMR absorption.

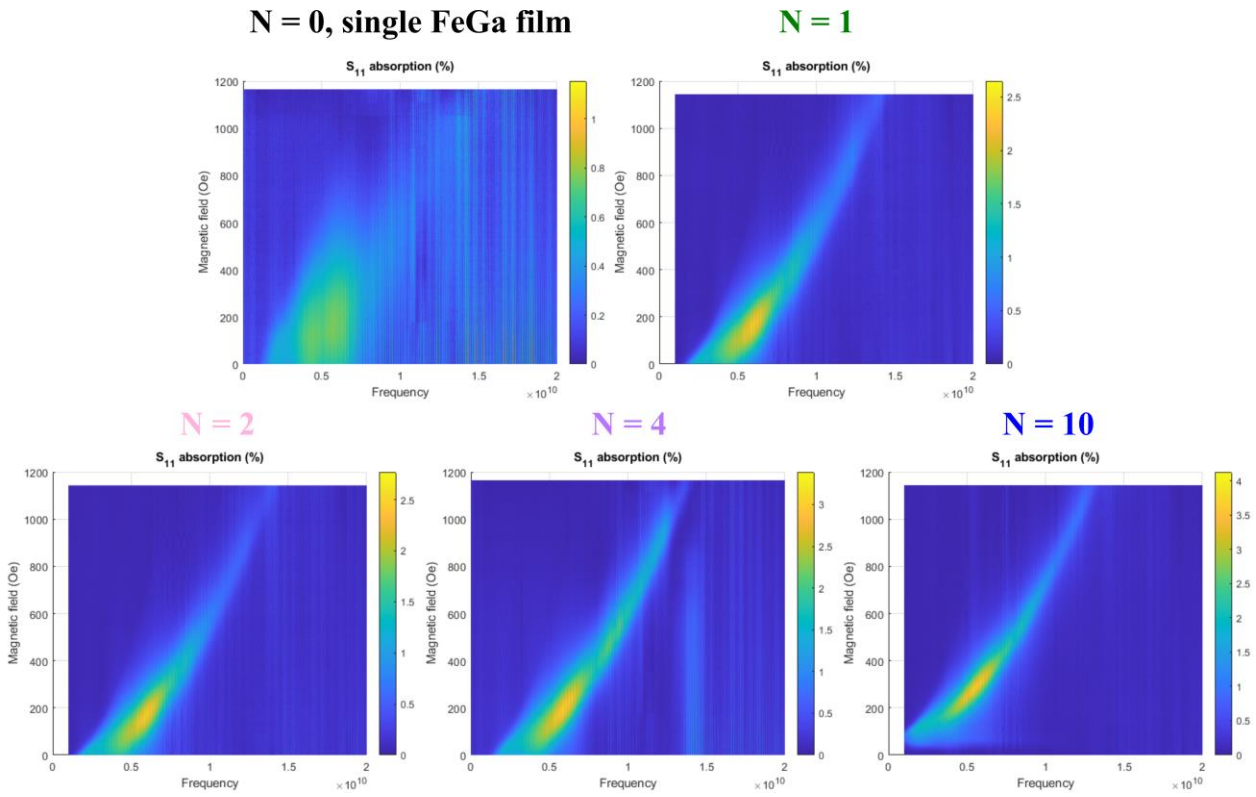

Figure 4.7: FMR spectra as a function of both frequency (100 MHz – 20 GHz) and magnetic bias (0 – 1200 Oe) for a single FeGa film (N=0) and multilayer FeGa/NiFe samples (N = 1, 2, 4, 10).

A fit of the FMR linewidth as a function of frequency can be used to calculate the gilbert damping. This is plotted in Figure 4.8 for the trends in the FMR linewidth as a function of frequency for the multilayers from Figure 4.1. The gilbert damping coefficient and the inhomogeneous linewidth, calculated from the slope and y-intercept of the fitted line, respectively, is tabulated in sssTable 4.1. The single FeGa film displays the largest gilbert damping coefficient at a value of 0.0851 and an inhomogeneous linewidth of 225 Oe. The value of the gilbert damping for the N = 1 bilayer structure sample decreases down to 0.0143 with a corresponding decrease in the inhomogeneous linewidth down to 171 Oe.

The sample with the highest magnitude of FMR absorption is the N = 10 multilayer structure, which also has the smallest coercivity that we indeed expect to correlate to a higher FMR absorption. Correspondingly, this sample has the smallest gilbert damping coefficient and inhomogeneous broadening of 0.0143 and 73 Oe, respectively.

We can interpret the results of the gilbert damping coefficient in context of the influence of multilayering on the microstructure. Based on the understanding of the underlayer effect in Chapter 3, we can expect that the N = 1 bilayer structure sample to have an enhanced (110) polycrystalline texture, while also having a smaller average grain size. The former leads to a smaller inhomogeneous linewidth, associated with disorder in the microstructure, and the latter is leads to a smaller gilbert damping coefficient which is expected from decrease in the effective magnetocrystalline anisotropy. An increase in the number of multilayers (going from N = 1 to N = 10) does not lead to a decrease in the gilbert damping coefficient, however, it leads to a decrease in the inhomogeneous linewidth so we can expect that additional NiFe interlayer improve the crystalline texture but not lead to changes in the average grain size.

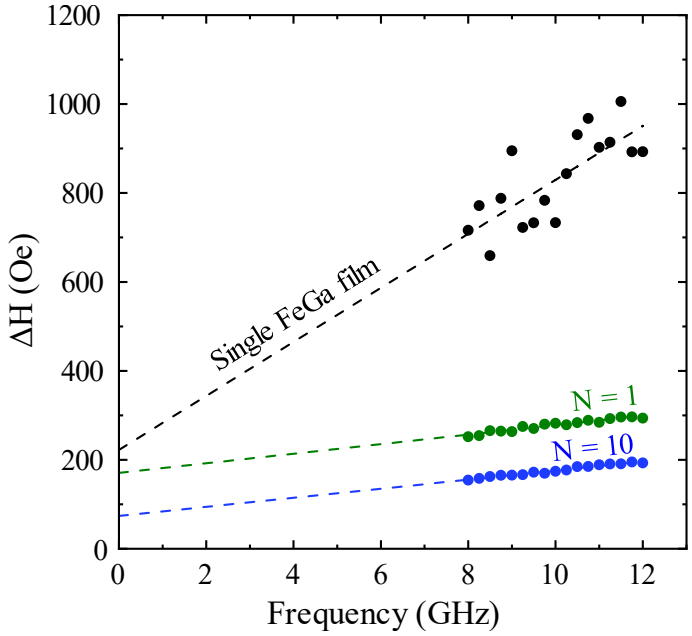

Figure 4.8: FMR linewidth as a function of frequency for a single FeGa film (N=0) and multilayer FeGa/NiFe samples (N = 1, 2, 4, 10) shown in Figure 4.7. Linear fit is shown as a dashed line.

Next, we looked at the influence of Al_2O_3 insulating interlayers for the N = 10 multilayer structure on the FMR absorption (Figure 4.9). Given that the N = 10 multilayer structure gives the smaller gilbert damping and inhomogeneous broadening, it is the best candidate to further optimize with an insulating interlayer insertion.

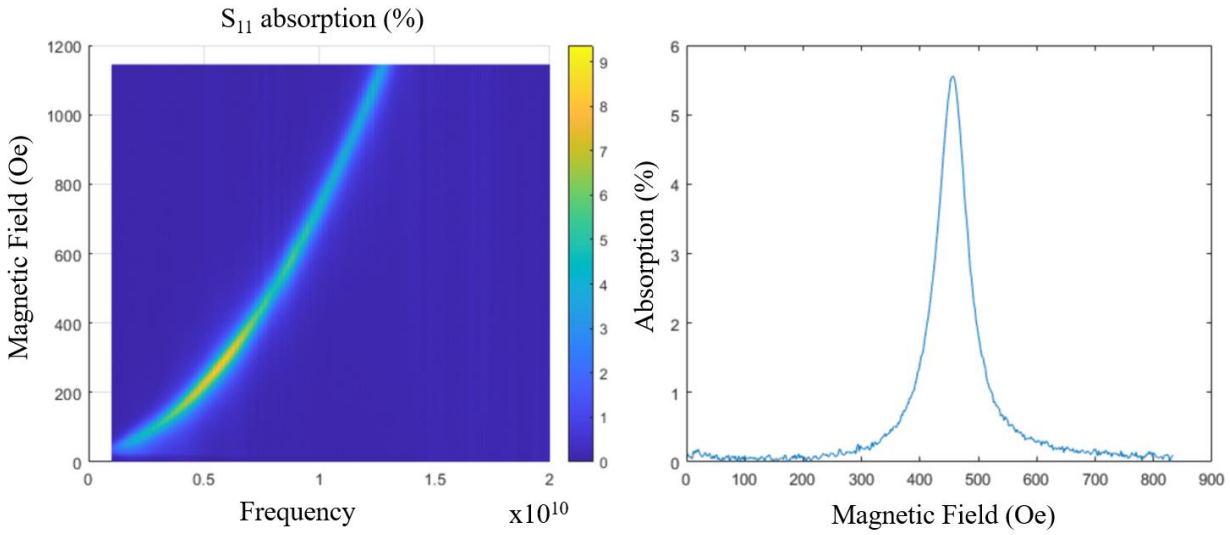

Figure 4.9: (left) FMR spectra as a function of both frequency (100 MHz – 20 GHz) and magnetic bias (0 – 1200 Oe) for a 10 trilayer stack of (10 nm FeGa/ 2.5 nm NiFe/ 2.5 nm Al_2O_3). (right) cross section of FMR absorption at 9 GHz.

It can be seen that the magnitude of the peak FMR absorption increases by more than a factor of 2, despite containing the same total amount of magnetic material between the two structures. This enhancement can be attributed to the impact of the Al_2O_3 insulating interlayers to reduce the losses from the generation of eddy currents that are disrupted across the thickness of the multilayer stack. We further plot the trends in the FMR linewidth as a function of frequency for the N = 10 and N =10 + Al_2O_3 multilayers in Figure 4.10. The gilbert damping coefficient and inhomogeneous broadening reach a low of 0.0081 and 38 Oe, respectively. This value of the gilbert damping and inhomogeneous broadening approaches the lowest value observed for homogeneous FeCoC films, 0.0027 and 30 Oe, respectively (Liang, Dong et al. 2018).

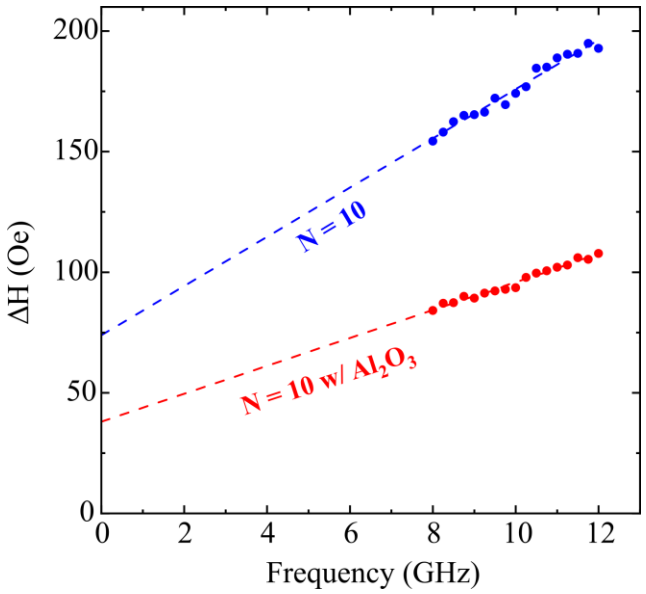

Figure 4.10: FMR linewidth as a function of frequency for the N = 10 multilayer sample in Figure 4.7 and the 10 bilayer stack of FeGa/NiFe/Al_2O_3 (N = 10 + Al_2O_3) in Figure 4.9. Linear fit is shown as a dashed line.

sssTable 4.1: Summary of the gilbert damping coefficient and inhomogeneous linewidth extracted from Figure 4.8 and Figure 4.10. Error bars represent 1 standard deviation to the linear fit parameters.

Sample	Gilbert damping, α	Inhomogeneous linewidth, ΔH_0 (Oe)
Single FeGa film	0.0851 ± 0.019	225 ± 137
N = 1	0.0143 ± 0.001	171 ± 8
N = 2	0.0167 ± 001	138 ± 9
N = 4	0.0143 ± 0.001	151 ± 8
N = 10	0.0143 ± 0.001	73 ± 4
N = 10 w/ Al_2O_3	0.0081 ± 0.001	38 ± 2

4.4 Summary and Outlook

We showed here that a multilayering strategy of FeGa/NiFe bilayers can be used to achieve a composite with smaller coercivity and lower high frequency losses than a single FeGa (100 nm)/NiFe (2.5 nm) bilayer structure. Specifically, a multilayer consisting of a 10 bilayers of FeGa (10 nm) / NiFe (2.5 nm) multilayers yields a magnetic film with a coercivity of 10 Oe and retains a strong uniaxial anisotropy (normalized remnant magnetization of 0.97). Additionally, the 10-bilayer structure exhibits a gilbert damping coefficient of 0.0143 and inhomogeneous broadening linewidth of 73. The addition of Al_2O_3 insulating interlayers in the structure further reduces the coercivity to 6 Oe, and more critically yields a gilbert damping coefficient of 0.0081 and inhomogeneous broadening linewidth of 73 Oe.

The multilayering strategy combined with an insulating interlayer is thus shown to be a useful strategy to achieve a composite that meets the necessary criteria of magnetic softness and low loss necessary for integration in magnetoelastic and high frequency antenna devices.

Chapter 5 Influence of the ferroelectric polarization on the stability of HfO_2 surfaces

To understand the relationship between the ferroelectric polarization and stoichiometry of ferroelectric HfO_2 surfaces we employed density functional theory. *Ab anitio* methods like density functional theory allow us to probe properties of a system that are often inaccessible to experiment. In this case, in this chapter we first isolated and decoupled the effect of the surface polarization on the surface energy of HfO_2 surfaces by comparing the surface energy of nonpolar tetragonal ($P4_2/nmc$) $HfO_2(110)$ surface to polar orthorhombic ($Pca2_1$) $HfO_2(001)$. We found that while a stoichiometric slab with O-terminated surface compositions is the most stable composition for nonpolar slabs, it is unstable for a polar slab. Additional O at the positively polarized surface of HfO_2 slabs leads to the stability of the surface by providing additional ionic charge that can screen the electrostatic potential. The insight gained here provides a guidance for the engineering of stable ferroelectric HfO_2 thin films for integration towards next-generation devices that require robust ferroelectricity at the nanoscale.

5.1 Surface structures of HfO_2 models

5.1.1 Nonpolar tetragonal HfO_2 slab surfaces

We constructed supercell slab structures consisting of nine Hf and ten O half-layers (~ nine-formula-units thick with each half-layer composed of either two Hf or four O atoms, i.e., two-formula units) from their respective nonpolar bulk tetragonal ((110) surface) and polar bulk orthorhombic ((001) surface) phases such that the polarization vector points normal to the surface of the orthorhombic slab (see Figure 2.20 in Chapter 2 for a more detailed description on how the slabs were constructed). Additionally, we fixed the middle three Hf and two O half-layers for all

slabs to their bulk-like arrangement to simulate a semi-infinite-bulk-like boundary condition for the surface atoms and to avoid spurious phase transformations.

We then generated slab supercells with surfaces of varying composition terminated with the following stoichiometric or off-stoichiometric terminations per surface unit cell: 2.0-O, 1.5-O, 1.0-O, 0.5-O, 1.0-Hf, and 0.5-Hf. We named the surfaces according to the atoms that compose their outermost layer and their number per formula unit. Each surface unit cell has an area corresponding to two-formula units (see Figure 5.1 and Figure 5.2 and their corresponding legend), therefore, an O-terminated surface with three O atoms per surface unit cell is named 3/2-O or 1.5-O, so that the names reflect the surface composition per surface formula unit. Among the compositions explored, the stoichiometric slabs are those with 1.0-O or 0.5-Hf terminations on both surfaces. We created the surfaces by removing O or Hf atoms starting from slabs with either 2.0-O or 1.0-Hf surfaces until we achieved the compositions listed above. We included slab supercells consisting of both compositionally symmetric and asymmetric surface terminations to explore the effect of the positive versus negative surface polarizations of the polar slabs in stabilizing different surface compositions. Therefore, along with compositionally symmetric slabs, namely, 2.0-O/2.0-O, 1.5-O/1.5-O, 1.0-O/1.0-O, 0.5-O/0.5-O, 1.0-Hf/1.0-Hf, and 0.5-Hf/0.5-Hf, we studied a select set of compositionally asymmetric slabs, namely, 1.5-O/1.0-O, 1.5-O/0.5-O, and 1.5-O/0.5-Hf (we provide below a rationale on why we targeted these asymmetric slabs). We named the slabs according to the composition of their top and bottom surfaces (whose naming scheme is discussed above). For example, 1.0-O/1.0-O refers to a supercell slab with both top and bottom surfaces terminated with two O atoms per surface unit cell (recall a surface unit cell is composed of two formula units, therefore the designation 1.0-O shows surface composition in per surface formula unit basis as explained above). Surface 1.5-O/1.0-O refers to a supercell slab with

three O atoms per surface unit cell at one surface and two O atoms per surface unit cell at the opposite surface. Note that for the orthorhombic slab, the top surface faces the positive polarization, while the bottom surface faces the negative polarization.

Figure 5.1 and Figure 5.2 respectively show the surface views of the relaxed nonpolar and polar slabs for the range of surface compositions explored. We faded-out the atoms lying in deeper layers in the surface view for clarity and the atoms in the outermost layers within a 1×1 unit cell area are circled. Additionally, the full profile view shows the most stable compositionally symmetric and asymmetric slabs.

For the polar orthorhombic slabs, we later discuss the need for construction of asymmetric surface terminations shown in Figure 5.2 to identify the thermodynamically most stable ferroelectric surfaces. For direct comparison to these asymmetric surface compositions, we also construct nonpolar tetragonal slabs shown in Figure 5.1 that parallel the asymmetric surface compositions of the polar orthorhombic slabs.

The reconstructions after relaxation of both surfaces of the compositionally symmetric nonpolar slabs mirror each other, as expected. The reconstructions of the two surfaces of the compositionally asymmetric nonpolar slabs, on the other hand, do not lead to the same structural configuration as the surfaces from their equivalent compositionally symmetric slab counterpart. For the polar slabs, two surfaces with a symmetric composition but with opposite polarization, positive (P+) for the top and negative (P-) for the bottom, did not reconstruct to be mirror configurations after relaxation. In almost all cases, the surface atoms roughly remain in their bulk-like lattice positions in the surface plane with primary relaxations along the surface normal – this is true for both the tetragonal and orthorhombic phases. The only glaring exception is the 1.5-

O/1.5-O orthorhombic slab where the P- O atoms undergo significant rearrangement, which is discussed in more detail below.

In the following sections, we discuss the relative stabilities of the surface structures and evaluate their electronic structures as a means to explain their stability or instability. We proceed with the nonpolar cases first; then we compare them with the polar cases.

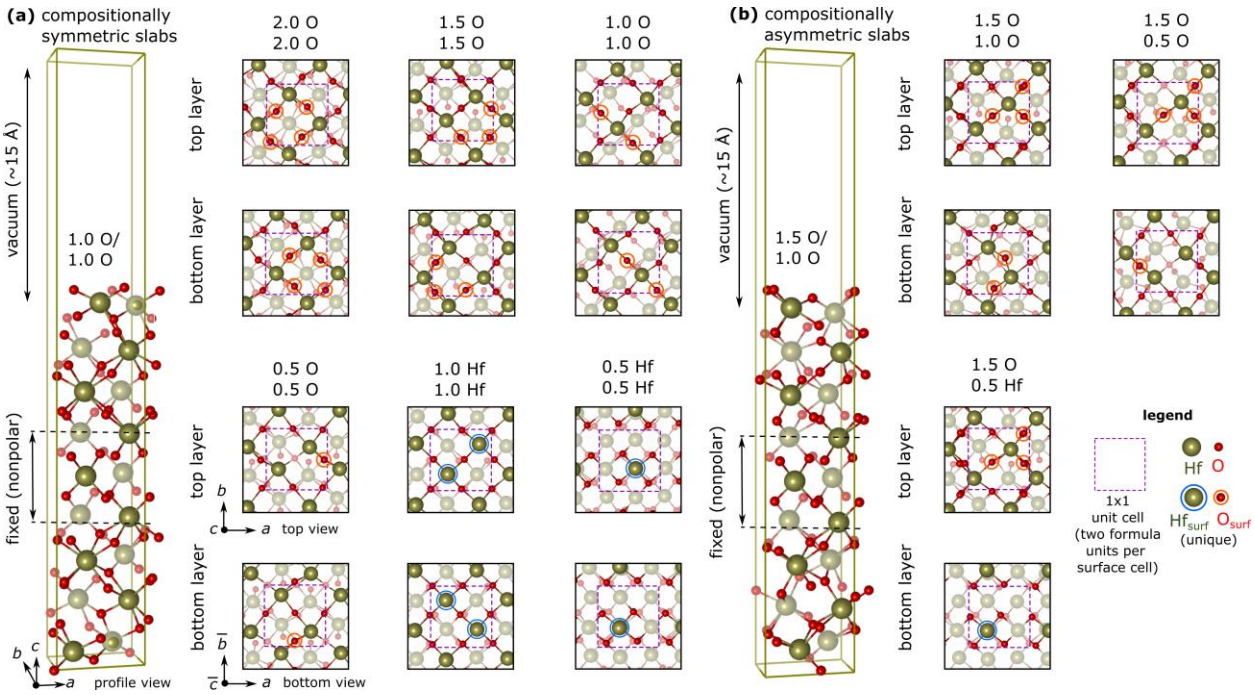

Figure 5.1: Relaxed structures for compositionally (a) symmetric and (b) asymmetric nonpolar tetragonal HfO_2 supercell slabs. Profile views are shown only for the most stable compositionally symmetric and asymmetric slabs among all compositions studied. Top and bottom views of the slabs are shown for the most stable configuration for a given composition. The composition of the outermost layers in terms of atoms per surface unit cell is labeled for the top and bottom layer above each structure. The fainter atoms are farther away from the viewer. Outermost atoms are circled within a 1 × 1 lateral unit cell that contains 2 f.u. (purple-dashed box)

5.1.2 Polar orthorhombic HfO_2 slab surfaces

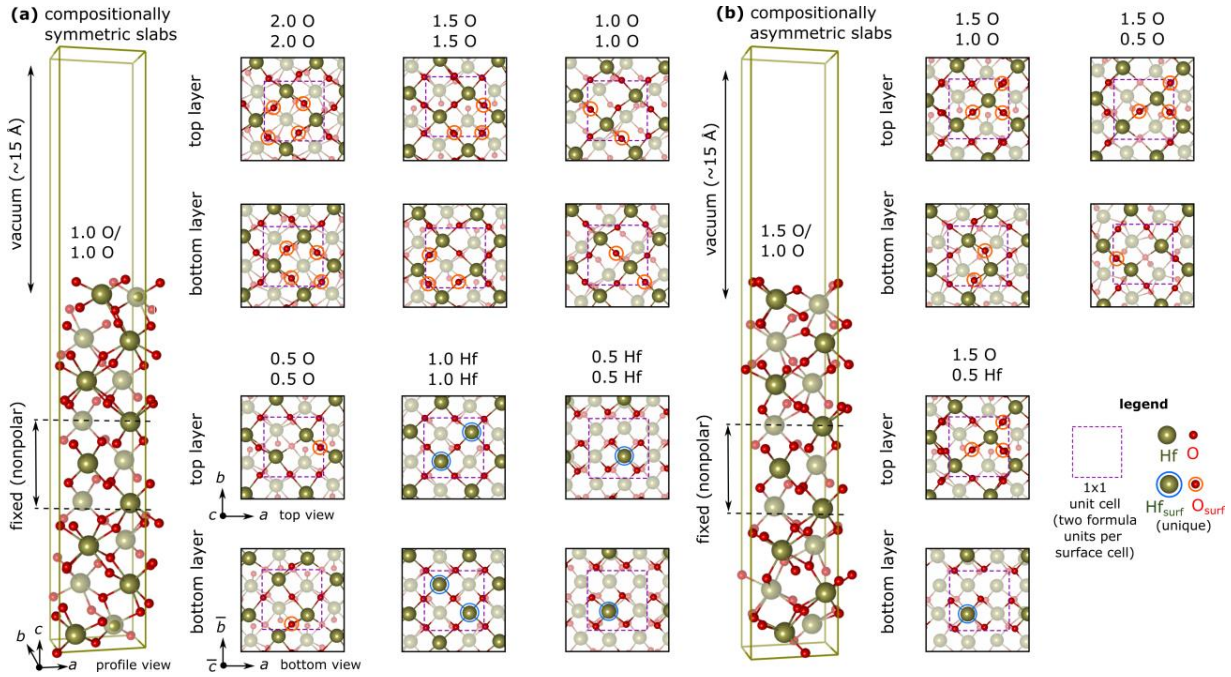

Figure 5.2: Relaxed structures for most stable compositionally (a) symmetric and (b) asymmetric orthorhombic HfO_2 supercell slabs. Profile views are shown only for the most stable compositionally symmetric and asymmetric slabs among all compositions studied. Top and bottom views of the slabs are shown for the most stable configuration for a given composition. The composition of the outermost layers in terms of atoms per surface unit cell is labeled for the top (P+) and bottom (P−) layer above each structure. To disambiguate the nomenclature for the compositionally asymmetric slabs, we use P+ and P− to refer to the composition of the positively and negatively polarized surfaces, respectively. The fainter atoms are farther away from the viewer. Outermost atoms are circled within a 1 × 1 lateral unit cell that contains 2 f.u. (purple-dashed box).

5.2 Surface energies

Figure 5.3 and Figure 5.4 display the surface energies for the most thermodynamically stable configurations of tetragonal HfO_2(110) and orthorhombic HfO_2(001) slabs at each surface composition explored as a function of both temperature (at 1 bar O_2) and pressure (at 900 K). Experimentally relevant ranges for crystallization of HfO_2 thin films were used for the choice of temperature and pressure: magnitudes of pressure experimentally explored range from ultra-high vacuum to high pressure annealing and temperatures up to near 1100 K have been applied to explore the tetragonal/orthorhombic phase boundary (Park, Chung et al. 2018, Mittmann, Materano et al. 2019, Woo, Goh et al. 2019, Hsain, Lee et al. 2020).

The slope of the surface energies arises from off-stoichiometry from the bulk Hf:O ratio of 1:2, which is reflected in the term $\left(\boldsymbol{N_O - 2N_{Hf}}\right)\boldsymbol{\mu_O}(\boldsymbol{T},\boldsymbol{p})$ in the reduced surface energy expression (section II-D). When $\boldsymbol{N_O > 2N_{Hf}}$, then the average surface energy ($\boldsymbol{\gamma_{average}}$) positively correlates with $\boldsymbol{\mu_O}(\boldsymbol{T},\boldsymbol{p})$ whereas when $\boldsymbol{N_O < 2N_{Hf}}$, a negative correlation between $\boldsymbol{\gamma_{average}}$ and $\boldsymbol{\mu_O}(\boldsymbol{T},\boldsymbol{p})$ exists. On the other hand, $\boldsymbol{\mu_O}(\boldsymbol{T},\boldsymbol{p})$ of the reservoir decreases with temperature *T* (primarily due to an increase in gas-phase entropy) but increases with O_2 partial pressure *p* (as expressed in the Gibbs-Duhem relation for an ideal gas, section II-D). The former (off-stoichiometry) factor explains the varying dependence of surface energies with *T* and *p* among different compositions, while the latter (chemical potential) factor explains the opposite *T* and *p* trend for a given composition in Figure 5.3 and Figure 5.4.

For the compositionally symmetric tetragonal slabs (i.e., ignoring 1.5-O/1.0-O, 1.5-O/0.5-Hf, and 1.5-O/0.5-O), the relative ordering of the surfaces with respect to stability for $100 < T \leq 1100$ K and 1 bar [Figure 5.3(a)] is: 1.0-O > 1.5-O > 0.5-Hf > 2.0-O > 0.5-O > 1.0-Hf, where ">"

means more stable. Comparing to the compositionally symmetric ferroelectric orthorhombic slabs (Figure 5.4), the same relative ordering of the surface stability holds at 400 - 1100 K and 1 bar except 1.5-O > 1.0-O (i.e., the 1.5-O/1.5-O line is lower in energy than the 1.0-O/1.0-O line within the entire temperature range investigated in Figure 5.4). The relative stability of 0.5-Hf and 2.0-O switches to 2.0-O > 0.5-Hf for $T < 400$ K (i.e., the 0.5-Hf/0.5-Hf line is higher in energy than the 2.0-O/2.0-O line at lower temperatures). We discuss later the effect of having asymmetric stoichiometries between the top and bottom terminations on the surface energies.

We can interpret the trends in stability of the surfaces primarily through electrostatics (in the absence of strong quantum mechanical influence, e.g., the breaking of covalent bonds producing "dangling bonds"). In general, a nonpolar surface is electrostatically stable without further surface modification or reconstruction needed (atomic or electronic). If one considers the tetragonal slab to be constructed from perfectly ionic equally spaced layers of pure Hf^{4+} and O^{2-} building blocks, one should expect from simple charge accounting that the compositionally symmetric slabs that exhibit bulk stoichiometry (Hf:O = 1:2), namely, 1.0-O/1.0-O and 0.5-Hf/0.5-Hf slabs to be stable (Tasker 1979). Indeed, the stoichiometric slab with a symmetric 1.0-O/1.0-O surface composition is lowest in energy (Figure 5.3). We can attribute the higher instability of the compositionally symmetric 0.5-Hf/0.5-Hf terminated surface to the more significant loss in the coordination number (higher number of dangling bonds) of Hf compared to O at the surface compared to the bulk. Deviation from either of the above-mentioned compositions leads to higher energy. An excess of O is less destabilizing than a deficiency of O: compare 1.5-O/1.5-O and 0.5-O/0.5-O in Figure 5.3. As expected, the former oxidizes surface O species while the latter reduces the Hf atoms in the layers below (*vide infra*). 1.0-Hf/1.0-Hf is very unstable due to the surface Hf^{4+} being reduced to lower oxidation states and a higher number of Hf dangling bonds.

Next, we consider stability trends for the polar orthorhombic slabs compared to the nonpolar tetragonal slabs. Despite similar composition between the tetragonal and orthorhombic phases, the non-centrosymmetric displacements of the Hf and O planes along the [110] direction of the tetragonal phase, which is along the [001] direction of the orthorhombic phase, result in a dipole and thus a polar (001) surface of the orthorhombic phase. We expect a polar surface to be compensated by a surface charging mechanism which generally occurs through a modification of the number surface ions to form nonstoichiometric surfaces or through electronic reorganization and electron transfer towards or away from the surface, producing, e.g., surface metallization. The former is understood to be preferential as the compensation mechanism (Levchenko and Rappe 2008, Stengel 2011, Garrity, Kakekhani et al. 2013, Setvin, Reticcioli et al. 2018, Gattinoni, Strkalj et al. 2020), given an available chemical reservoir that can exchange with ions or molecules. Here, the formation of polar orthorhombic slab surfaces resulting in a nonstoichiometric deviation from the bulk indeed leads to some degree of stabilization for the polar orthorhombic slab surfaces: compare 1.5-O/1.5-O vs 1.0-O/1.0-O in Figure 5.4 Despite the compositional symmetry of the surfaces in 1.5-O/1.5-O, the distinct ability of O to form a bond with another surface O leads to formally compositionally asymmetric P+ and P- surfaces. As Figure 5.2 shows, the 1.0-O/1.0-O has all of its surface O coordinated only with Hf on both terminations – this in fact leads to surface metallization to (partly) screen the surface polarization (*vide infra*). In the 1.5-O/1.5-O, on the other hand, a pair of surface O on the P- surface form a bond of length 1.37 Å (see Figure 5.2), reminiscent of an average between a peroxide and superoxide bond (Cramer, Tolman et al. 2003). This rearrangement does not appear in the corresponding 1.5-O/1.5-O tetragonal slab (Figure 5.1). The formation of an O−O bond is favored on the P- because this surface would otherwise favor p-doping (O_2^{n-} species are an oxidized form of O^{2-} which may act as a positive localized surface

defect). This eliminates the need for the P- to metallize (p-doped) to screen the polarization charge (*vide infra*).

In fact, we can construct an orthorhombic slab with asymmetric composition between surfaces that has an even lower average surface energy which requires only half an additional O per surface-formula-unit at the P+ surface (to disambiguate the nomenclature for the compositionally asymmetric slabs, we use P+ and P- to refer to the composition of the positively and negatively polarized surfaces, respectively). For example, at 900 K and 1 bar, this asymmetric orthorhombic slab with a surface composition of P+:1.5-O/P-:1.0-O has an average surface energy of 2.14 J/m^2 compared to 2.22 J/m^2 for the compositionally symmetric case of 1.5-O/1.5-O (Figure 5.4). Although asymmetric reconstruction appears to be an effective mechanism to stabilize the polar phase, other examples of such modifications, namely, P+:1.5-O/P-:0.5-O and P+:1.5-O/P-:0.5-Hf, do not improve the average surface energy. The two latter examples expose more undercoordinated Hf, which also is unfavorable for the tetragonal phase. In P+:1.5-O/P-:0.5-O, the removal of O from, e.g., P-:1.0-O or P-:1.5-O to yield P-:0.5-O composition exposes the Hf in the layer below (Figure 5.2).

The tetragonal slabs with an asymmetric surface termination have surface energies that are almost the average of energies of the surface stoichiometries from which they are derived. For example, the surface energy at 900 K and 1 bar is 2.09 J/m^2 for the 1.5-O/1.0-O slab, which is roughly the average of 2.53 J/m^2 and 1.49 J/m^2 that correspond to the surface energies of the 1.5-O/1.5-O and 1.0-O/1.0-O slabs. In contrast, the average surface energy of P+:1.5-O/P-:1.0-O (2.14 J/m^2) is lower than that of the average (2.34 J/m^2) of the surface energies of the orthorhombic slabs 1.5-O/1.5-O (2.22 J/m^2) and of 1.0-O/1.0-O (2.46 J/m^2) at the same temperature and pressure.

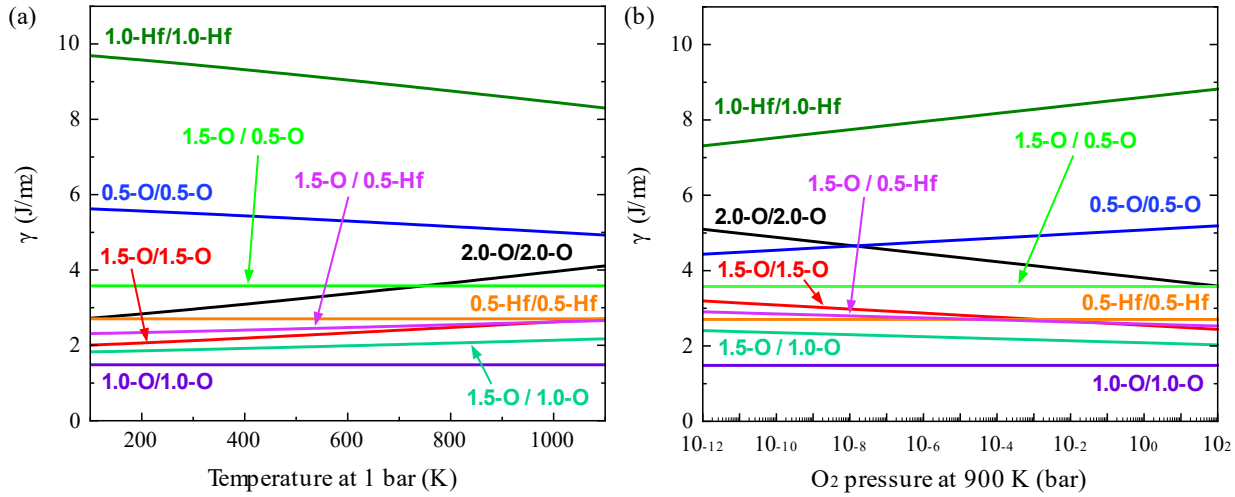

Figure 5.3: Plot of surface energy as a function of (a) temperature from 100 to 1100 K and (b) pressure from 10^{-12} to 10^{2} bar for compositionally symmetric and asymmetric tetragonal HfO_2(110) slabs.

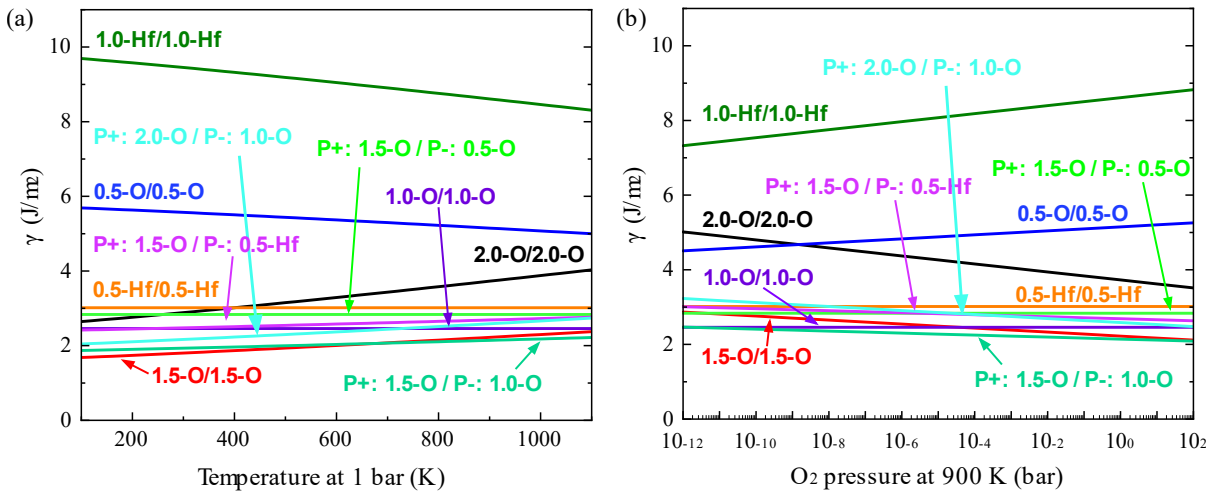

Figure 5.4: Plot of surface energy as a function of (a) temperature from 100 to 1100 K and (b) pressure from 10^{-12} to 10^{2} bar for compositionally symmetric and asymmetric orthorhombic HfO_2(001) slabs. To disambiguate the nomenclature for the compositionally asymmetric slabs, we use P+ and P− to refer to the composition of the positively and negatively polarized surfaces, respectively.

5.3 Surface bader charges

To obtain further insight into the electronic charge redistribution that leads to stabilization of the polar orthorhombic HfO_2 slabs with 1.5-O/1.5-O and P+:1.5-O/P-:1.0-O surface terminations over the 1.0-O/1.0-O surface termination, we calculated the Bader charges of O and Hf in each layer. The Bader charge analysis (Bader 1990, Henkelman, Arnaldsson et al. 2006) partitions the continuous charge density into atomic charges and because HfO_2 is largely ionic, this analysis is an appropriate choice to assign atomic charges. Figure 5.5 displays the charge deviation layer-by-layer in both tetragonal and orthorhombic slabs, where we see the major changes occur near the surface, induced by the ferroelectric polarization in the middle bulk layers in the orthorhombic slab. We calculated the deviation of the charge per atom within the slab with respect to the average Bader charge values of Hf and O in their respective bulk phases (tetragonal or orthorhombic). The calculated Bader charges in the tetragonal phase are 9.41 *e* for Hf and 7.30 *e* for O (corresponding to the outer core/valence electrons only, i.e., not including the electrons subsumed into the PAW potentials), and in the orthorhombic phase are 9.41 *e* for Hf and 7.31 *e* and 7.29 *e* for the two types of O. In comparison, the valence charges should be 12 *e* ($5s^2 5p^6 6s^2 5d^2$) for neutral Hf and 6 *e* ($2s^2 2p^4$) for neutral O. In the orthorhombic phase, the O takes two values that differ by 0.02 *e* depending on their location in the polar or nonpolar half-unit.

The tetragonal HfO_2 with a symmetric 1.0-O/1.0-O surface composition yields Bader charges of O at the surface closest to the bulk value, which indicates that they are fully ionized to a bulk-like oxidation state [Figure 5.5(a)]. The symmetric cases (1.0-O/1.0-O and 1.5-O/1.5-O) have symmetric distributions of charge across the slabs, as expected. In the tetragonal cases with excess O, i.e., 1.5-O/1.5-O and 1.5-O/1.0-O, the surface O atoms on the 1.5-O surface contain fewer electrons (negative change deviation, oxidized) with some additional depletion of O charge

(although significantly less) within the inner layers across the slab [Figure 5.5(a)]. For the asymmetric 1.5-O/1.0-O termination, the charge deficiency of the O atoms is asymmetric, where the 1.5-O surface corresponds to the 1.5-O surface in the symmetric 1.5-O/1.5-O slab (0.41 *e*/atom and 0.42 *e*/atom, respectively), and the 1.0-O surface has a charge deficiency of 0.12 *e*/atom which lies closer to the value of 0.06 *e*/atom in the symmetric 1.0-O/1.0-O slab.

In compositionally symmetric orthorhombic slabs, we expected electrons to transfer from the P- to the P+ surface as a screening mechanism in order to eliminate the polarization field. Comparing the most thermodynamically stable nonpolar tetragonal 1.0-O/1.0-O slab to its ferroelectrically polarized counterpart in the orthorhombic 1.0-O/1.0-O slab, an additional deficiency of -0.19 *e*/atom exists at the P- surface. At the positive P+ surface, the charge deficiency (0.06 *e*/atom) equals to that of the tetragonal phase, instead, the excess electron (0.28 *e*/atom) accumulates in the Hf half-layer below [Figure 5.5(b)].

The addition of an O to both surface unit cells of the orthorhombic 1.0-O/1.0-O slab to arrive at the more thermodynamically stable orthorhombic 1.5-O/1.5-O slab shows that the excess accumulation of electrons decreases at the P+ surface [Figure 5.5(b)]. This indicates that the addition of O can adequately provide the ionic charge to screen the ferroelectric polarization with a smaller need for electronic charge redistribution across the slab (the excess O on the 1.5-O P+ surface also ionizes more than in the tetragonal phase). However, a large excess of O on the P- surface that is already electron-deficient yields even more electron-deficient surface O atoms (associated with the emergence of the surface O_2^{n-} species, *vide supra*), decreasing by approximately 0.44 *e*/atom. This indicates that while the addition of O on the P+ surface is favorable, it leads to the destabilization of the P- surface. The removal of an O from the P- surface of the 1.5-O/1.5-O slab to yield the P+:1.5-O/P-:1.0-O slab alleviates this electron deficiency and

thus can explain further stabilization of the asymmetric slab compared to the symmetric 1.5-O/1.5-O.

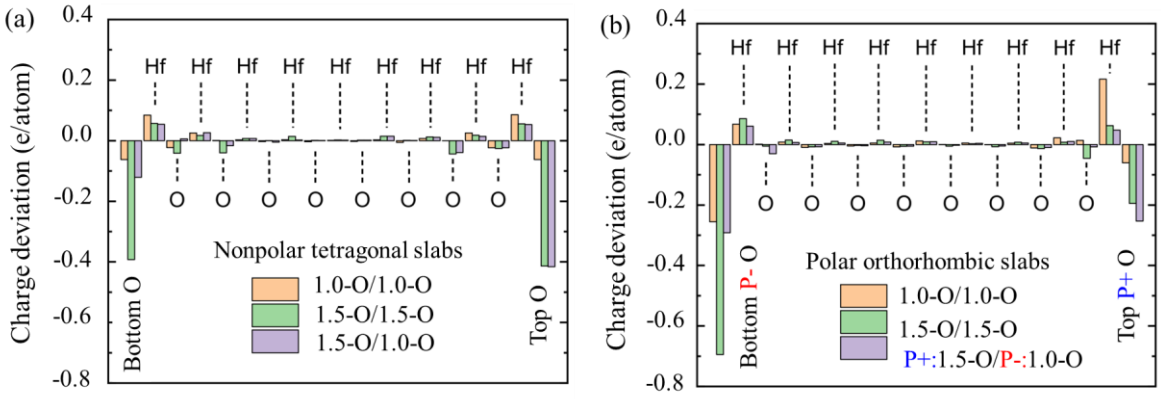

Figure 5.5: Layer-by-layer Bader charge deviation for (a) nonpolar tetragonal and (b) polar orthorhombic HfO_2 slabs for three different compositions. The values correspond to the average Bader charge deviation per atom for each Hf and O half-layer relative to their respective bulk phase. Note that the left- and right-hand sides of the plots correspond respectively to the bottom and the top of the slabs. In the surface nomenclature, the composition of the top surface is given first.

5.4 Interpreting surface stability via electrostatic potential and projected DOS profiles

To study the electronic response of ferroelectric HfO_2 to the built-in electric field, we calculated and plotted the plane(*xy*)-averaged electrostatic potential (blue lines) and its out-of-plane running average ("z-averaged", within 5.09 Å windows, red lines) along the direction normal to the slab (Figure 5.6). The flat electrostatic potential in the vacuum on each side of the slabs confirms that the vacuum thickness is large enough and that the dipole correction is effective in removing spurious interaction between slabs. The nonpolar 1.0-O/1.0-O tetragonal slab displays a symmetric profile across both surfaces from the center of the slab [Figure 5.6(a)]. In contrast, for the polar 1.0-O/1.0-O slab, the ionic displacement associated with the tetragonal to orthorhombic HfO_2 phase transition in the bulk layers sets up a potential gradient across the slab [Figure 5.6(b)]. As a result, a difference remains in the work function between the P+ surface and P- surface of -4.25 eV. From the slope of the *z*-averaged electrostatic potential across the fixed middle layers of the slab, we approximate the electric field to be roughly -0.34 V/Å. This electric field drives the accumulation of excess charge observed in the Hf half-layer on the P+ surface [Figure 5.5]. We examine below how this large electrostatic potential leads to the dielectric breakdown, as visualized in Figure 5.6.

The addition of O to both surfaces in the case of the polar 1.5-O/1.5-O slab [Figure 5.6(c)] serves to reduce the electrostatic potential difference, and we observe a reduction in the magnitude of the difference in the work function between the two surfaces and the electric field to 0.7 eV and 0.186 V/Å, respectively. Removal of an O from the P- surface of the 1.5-O/1.5-O slab to yield the P+:1.5-O/P-:1.0-O slab [Figure 5.6(d)] alleviates the deeper potential on the P- surface and causes the slope of the electrostatic potential to vanish – the magnitude of the difference in the work function and the electric field decreases to -0.07 eV and 0.03 V/Å, respectively.

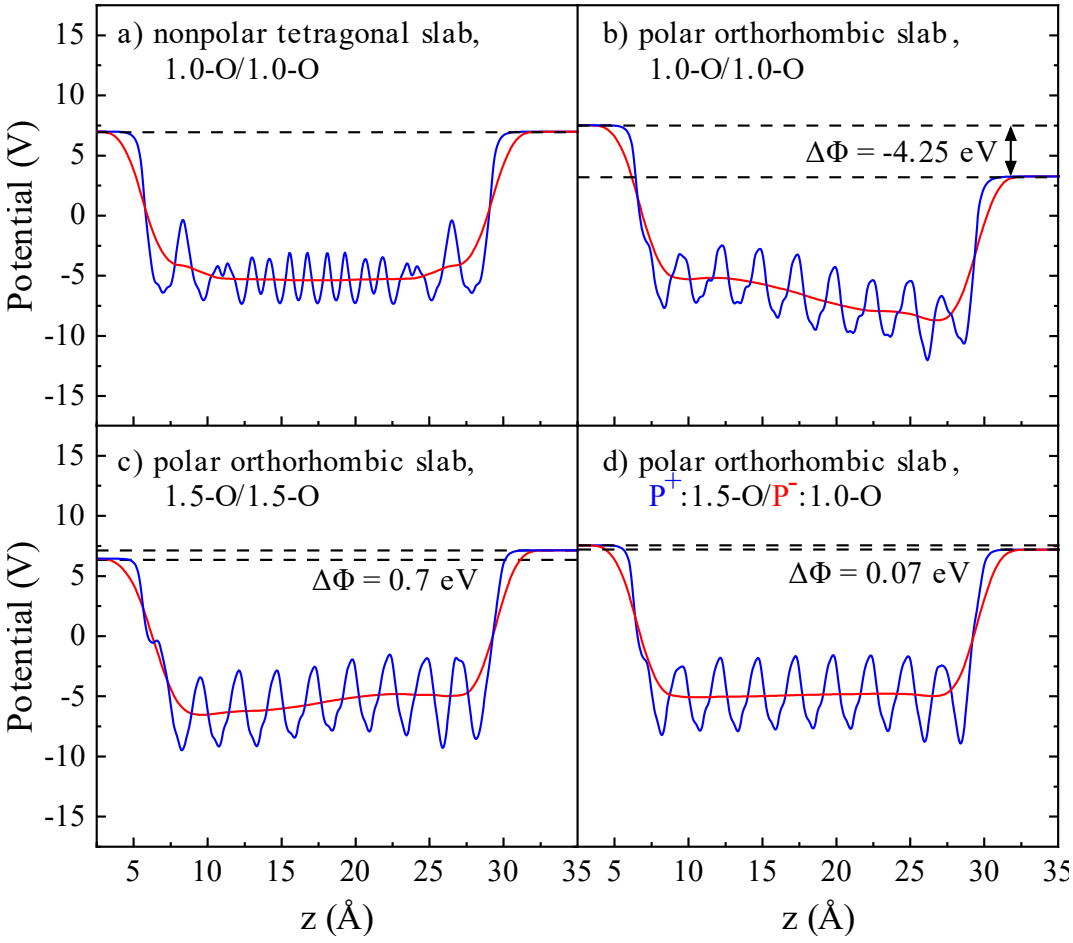

Figure 5.6: Plane-averaged electrostatic potential comprised of the ionic and Hartree potentials (blue) and the z-averaged potential (red), calculated along the surface normal for the tetragonal(110) surface with (a) symmetric 1.0-O/1.0-O composition and orthorhombic(001) surfaces with (b) symmetric 1.0-O/1.0-O, (c) symmetric 1.5-O/1.5-O, and (d) asymmetric P+:1.5-O/P−:1.0-O compositions. The potentials are referenced to the Fermi level. The horizontal dashed lines mark the positions of the vacuum level for each surface. The difference in the work functions (ΔΦ) is the difference in the vacuum potentials of the two surfaces multiplied by a unit of elementary charge e = 1. Note that the left- and right-hand sides of the plots respectively correspond to the bottom and the top of the slabs. In the surface nomenclature, the composition of the top surface is given first.

Figure 5.7(a) shows a layer-by-layer projected densities of states (pDOS) for the most stable tetragonal slab with symmetric composition of 1.0-O/1.0-O and Figure 5.7(b) shows its orthorhombic counterpart with the same symmetric composition. The top pDOS in each panel of

Figure 5.7 corresponds to the top (P+ for orthorhombic) surface O layer for each structure. Each subsequent pDOS going downward in each panel corresponds successively to the Hf or O half-layer below, with the lowest pDOS corresponding to the bottom (P- for orthorhombic) surface O layer. Note how the bands hardly shift relative to the band edges of the middle layers for the 1.0-O/1.0-O tetragonal slab, except for the outermost layers as expected due to the change in their coordination environments (Figure 5.7(a)). An increased density of O states exists at the surface, but the O atoms remain fully reduced and closed shell. The nonpolar tetragonal slab also remains insulating throughout the slab as in the bulk.

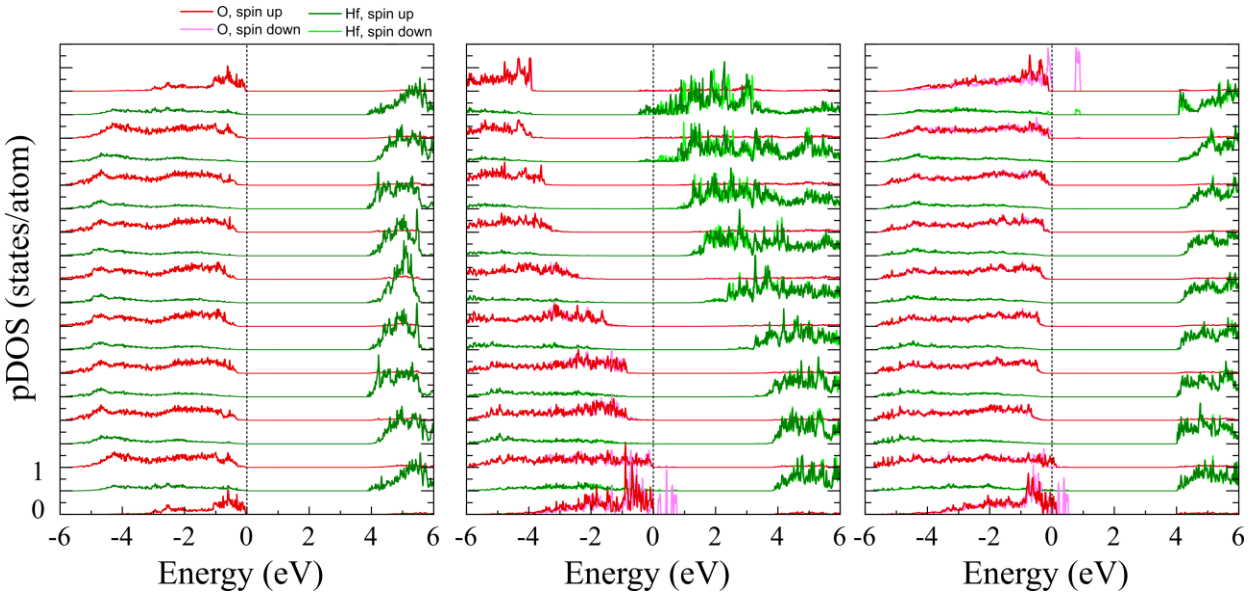

Figure 5.7: Layer-by-layer projected densities of states (pDOS) for the tetragonal HfO2(110) surface with (a) symmetric 1.0-O/1.0-O composition and orthorhombic (001) surfaces with (b) symmetric 1.0-O/1.0-O, (c) symmetric 1.5-O/1.5-O, and (d) asymmetric P+:1.5-O/P−:1.0-O compositions. The electronic energies reference to the valence-band edge or the Fermi level (dashed vertical lines mark Energy = 0 eV). The top O layer of the polar orthorhombic slab corresponds to the P+ surface and the bottom O layer corresponds to the P− surface. Hf half-layer spin up/down: green/light green; O half-layer spin up/down: red/pink. The values are shifted so that the pDOS of the top and bottom layers correspond respectively to the top-most and bottom-most curves

It is known that large electric fields originating from the spontaneous polarization of ferroelectrics induce band bending at ferroelectric surfaces and interfaces (Cohen 1997, He, Stephenson et al. 2012, Huang, Chen et al. 2012, Kalinin, Kim et al. 2018, Gattinoni, Strkalj et al. 2020). The net macroscopic field from the steep electrostatic field [Figure 5.6(b)] dramatically shifts the bands as a function of position across the slab in the polar orthorhombic slab – compare [Figure 5.7(a) and (b)]). Examining the pDOS starting at the top surface (P+) of the orthorhombic slab [Figure 5.7(b)], we see that the Fermi level is now above the conduction band edge of the outermost Hf sublayer, indicating that the interface is conducting (n-doped). Moving towards the bulk, the conduction and valence bands both rise in energy almost linearly, such that the Fermi

level lies roughly in the middle of the bulk frontier states. The increase in energy of the frontier states continue while descending down the slab layers, where finally at the bottom surface (P-), we see that the Fermi level now lies below the (O-derived) valence band edge, making that surface also conducting (p-doped). Additionally, spin polarization reveals induced magnetic moments for both the (reduced) Hf and (oxidized) O atoms near and at the surface of the orthorhombic slab.

Figure 5.7(c) and (d) show the pDOS for the most thermodynamically stable compositionally symmetric (1.5-O/1.5-O) and asymmetric (P+:1.5-O/P-:1.0-O) orthorhombic slabs. In contrast to the 1.0-O/1.0-O orthorhombic slab in Figure 5.7(b), the more stable 1.5-O/1.5-O orthorhombic slab in Figure 5.7(c) exhibits a reduction in band bending across the sublayers, which we attribute to the additional ionic charge that screens the macroscopic electrostatic potential from the ferroelectric polarization in the bulk. In general, the accumulation of excess charge as a charge screening mechanism that leads to the filling of the surface conduction bands in ferroelectric oxides is energetically expensive as the potential across the slab (prior to charge redistribution) would need to be greater or equal to the band gap, which for HfO_2 is at least ~4.34 eV (Stengel 2011). The emergence of nonstoichiometric polar HfO_2 slabs provides the additional ionic charge that can effectively screen ferroelectric polarization, avoiding the need for surface metallization as a charge screening mechanism.

The addition of O on the P+ surface of the 1.5-O/1.5-O orthorhombic slab eliminates the need to n-dope the top Hf sublayer (compare the topmost Hf layer pDOS in Figure 5.7(c) to Figure 5.7 (b)). In Figure 5.7(c), the Fermi level of the top surface (P+) now lies at the valence band edge, making the surface insulating, although localized empty states exist above the Fermi level in this layer (a complete reversal compared to the orthorhombic 1.0-O/1.0-O termination where the Hf sublayer of the P+ surface is n-doped, Figure 5.7(b)). Although an excess O on the P- surface is in

principle electrostatically unfavorable, the emergence of O_2^{n-} on this surface of the 1.5-O/1.5-O orthorhombic slab (Figure 5.7(a)) provides a net positive defect (for $n < 2$, because it replaces an otherwise surface O^{2-} ion) that is favored on the P- surface. This mechanism in fact eliminates the metallization of the P- surface (compare the bottom O layer pDOS in Figure 5.7(c) to 5.7(b). However, at the P- surface, an O-derived state exists just above the Fermi level (Figure 5.7(c), associated with the O_2^{n-} species). Spin polarization is also induced, especially for the P- surface O atoms (once again consistent with the O_2^{n-} species).

Finally, as previously highlighted, the most stable orthorhombic slab favors an asymmetric surface composition (P+:1.5-O/P-:1.0-O). Keeping the excess O on the P+ while removing it on the P- surface ultimately leads to enhanced stabilization and removal of band bending [Figure 5.7 (d)], although the p-doped metallic character of the P- surface persists as in the orthorhombic 1.0-O/1.0-O case. The O atoms are fully ionized except for the outermost P+ and P- O atoms. The emergence of the empty gap states on the P+ surface indicate that more O is present than is needed to screen the positive polarization charge - a lower excess O coverage would suffice, although the limited simulation supercell size does not capture this effect.

The stability of asymmetric oxygen termination at the P+ and P- surfaces can partially explain the observed "wake-up effect" in HfO_2-based ferroelectrics that increases the orthorhombic/tetragonal phase fraction and stabilizes the strength of ferroelectric polarization after electric field cycling (Zhou, Xu et al. 2013, Hoffmann, Schroeder et al. 2015, Lomenzo, Takmeel et al. 2015, Schenk, Hoffmann et al. 2015, Buragohain, Richter et al. 2018, Jiang, Luo et al. 2021). After crystallization of HfO_2 via a nonpolar tetragonal phase pathway, the instability of the stoichiometric surfaces (which the tetragonal nonpolar phase initially favors) would disfavor the persistence of polar ferroelectric grains after polarization with an electric field. In the context of

these prior observations and proposed mechanisms of the wake-up effect, redistribution of O vacancies near the surfaces or interfaces of HfO_2 films through electric-field cycling then could contribute to the sustained stabilization of ferroelectric polarization after many cycles.

5.5 Summary & outlook

We constructed nonpolar slabs from the bulk tetragonal HfO_2 phase composed of alternating pure Hf and pure O half-layers along the [110] direction. We found the most stable (110) surface to be O-terminated with only one O atom present per surface formula unit, instead of two O. The slab maintains overall stoichiometry and the stable reconstruction satisfies simple electrostatic requirements to eliminate electrostatic potential divergence when truncating along this direction where alternating positive (Hf) and negative (O) planes exist.

For the corresponding (001) surface in the structurally related ferroelectric orthorhombic phase, we found polarization to have a nontrivial influence on the surface energetics. Surface-polarization charge, due to the bound charge displacements within the slab, favors a deviation in the surface composition relative to the nonpolar surface. Specifically, the positively polarized surface remains O-terminated but favors a composition with 1.5 O per surface formula unit, while the negatively polarized surface still favors one O per surface formula unit.

The ferroelectric polarization induces an increase in the electrostatic potential across the slab that leads to band bending (as illustrated in layer-by-layer pDOS) and is associated with an unstable surface configuration in slabs whose only means of polarization screening occurs through a major charge redistribution and electronic reorganization that metallizes the surface. Thus, ionic passivation of the excess surface charge screens effectively the internal polarization of the ferroelectric displacements and is more favorable than free carrier compensation through band

bending, also yielding improved stability of the polar slab. In ongoing work, we are exploring the reciprocal effect to understand how the optimal surface composition can influence the stability of ferroelectric polarization across the entire thickness of HfO_2 films (as was predicted recently for ferroelectric $BaTiO_3$ and $PbTiO_3$ (Saidi, Martirez et al. 2014)).

Our results, in the conjunction with prior work on ferroelectric HfO_2, highlight the importance of the interaction between surface composition and stability of surface polarization. As surfaces and interfaces play emphasized dominant role at small scales, this points to the necessity to carefully consider the role of chemistry and surface engineering in the stabilization and implementation of ferroelectric HfO_2 for technological applications.

Chapter 6 Effect of the surface composition and thickness on the stability of ferroelectric polarization in HfO_2 thin films

After establishing that there is an intimate link between the stability of the surface composition and ferroelectric polarization in HfO_2, the influence of the surface composition and thickness on the stability of ferroelectric polarization in HfO_2 thin films was further studied using density functional theory. The surface composition was found to play a critical role in the ferroelectric stability of HfO_2 thin films and we demonstrate an evolution of HfO_2 polarization with decreasing thickness that can account for the recently observed absence of a ferroelectric critical thickness. These results highlight the importance of the surface composition for the stability of ferroelectricity in HfO_2 and points towards control of the surface composition as a mechanism for optimizing the ferroelectric performance of HfO_2-based thin films toward next generation nanoscale applications of ferroelectric materials, e.g. toward multiferroic devices.

6.1 Influence of composition on the ferroelectric stability of HfO_2 slabs

We compared two cases for polar orthorhombic HfO_2 supercell slab structures: a stoichiometric slab with O-terminated surfaces and symmetric compositions across the positive (P+) and negative (P−) polarization surfaces, and a nonstoichiometric slab with asymmetric composition across the P+ and P− surfaces. The choice of the two surface compositions for polar orthorhombic HfO_2 slabs comes from our prior work, in which we showed that while a compositionally symmetric surface (consisting of 1.0-O termination per surface formula unit on both surfaces: 1.0-O/1.0-O) is the most stable for a nonpolar tetragonal ($P4_2/nmc$) slab, the same composition is unstable for a polar orthorhombic ($Pca2_1$) slab (Acosta, Martirez et al. 2021). Instead, an asymmetric termination of 1.5-O and 1.0-O per surface formula unit on the P+ and P− surface, respectively (P+:1.5-O/P−:1.0-O), is more stable for the orthorhombic slab. We showed that the greater stability of the latter arises from its ability to screen the surface polarization more effectively (Acosta, Martirez et al. 2021).

Before examining the thickness effect on the stability of polarization in orthorhombic HfO_2 thin films, we first established the polarization response to the surface composition using an 11-Hf-half-layer thick slab. As mentioned above, in our prior work, the bulk nonpolar tetragonal and polar orthorhombic phases favor O-terminated symmetric (1.0-O/1.0-O) and asymmetric (P+:1.5-O/P−:1.0-O) surfaces, respectively (Acosta, Martirez et al. 2021). The intimate relationship between surface composition and ferroelectric stability at reduced dimensionality, such as in thin films, necessitates us to look at the two surface compositions. Although previously we found that the 1.5-O/1.5-O surface composition is more stable than the P+:1.5-O/P−:1.0-O one for the bulk orthorhombic phase below 680 K and at an O_2 pressure of 1 bar, we focus here on the P+:1.5-O/P−:1.0-O because it is more stable at ≥ 680 K and the experimentally necessary conditions to crystallize ferroelectric orthorhombic HfO_2 thin films generally require annealing above 900 K (Mittmann, Materano et al. 2019).

After ionic relaxation, the 11-Hf-half-layer thick HfO_2 supercell slab with a symmetric surface composition (initialized with a bulk polar orthorhombic $Pca2_1$ structure) transitions to a monoclinic ($P2_1/c$)-like phase (Figure 6.1) which is centrosymmetric and nonpolar in its bulk ground state (Muller, Boscke et al. 2012, Huan, Sharma et al. 2014). Figure 6.1 highlights the repeating four-HfO_2-formula-units resembling a conventional monoclinic unit cell with its [001] axis normal to the surface. For a comparison of the structural similarity, Figure 6.2(a) in the Supplemental Material (SM) presents different views of the optimized bulk monoclinic phase presented with the different views of the relaxed symmetric slab [Figure 6.2(b)]. Additionally, we present a comparison of the interlayer Hf spacings and intralayer O spacings for the bulk monoclinic phase and the symmetric HfO_2 slab in Figure 6.2(c) of the SM . Note that because the 11-Hf-half-layer thick slab contains 5.5 formula units of the conventional monoclinic unit cell, the

center of the slab accommodates the remaining layer (0.5 formula units out of plane) to be one that instead retains resemblance to the higher symmetry orthorhombic unit cell, which in turn contributes a residual polarization that we discuss later.

Ionic relaxation to a nonpolar monoclinic-like phase is a consequence of the otherwise unscreened dipole of the polar orthorhombic phase. This depolarization manifests in the plane-averaged electrostatic potential and plane-integrated electron density plotted along direction normal to the slab in Figure 6.4(a). Before ionic relaxation, an electrostatic potential builds up across the slab and results in a net difference in electrostatic potential between the P− and P+ surfaces of 3.01 V. Ionic relaxation does not eliminate entirely but reduces this electrostatic potential difference to 0.46 V. Furthermore, before ionic relaxation, note the asymmetric excess accumulation of electron density at the P+ surface compared to the P− surface [see Figure 6.4(a)], which is required to screen the ferroelectric polarization in the absence of other charge compensating mechanisms. After ionic relaxation, the distribution of electron density near the P+ and P− surfaces balances more evenly between both surfaces.

In contrast to stoichiometric HfO_2 slabs constructed with symmetrically terminated surfaces, nonstoichiometric HfO_2 slabs with asymmetric surface composition maintain a bulk-like polar orthorhombic phase after ionic relaxation (see right panel of Figure 6.1). Passivation with an additional O on the P+ surface compared to the HfO_2 slab with symmetric surfaces appears to be sufficient to provide the charge screening needed to sustain polarization.

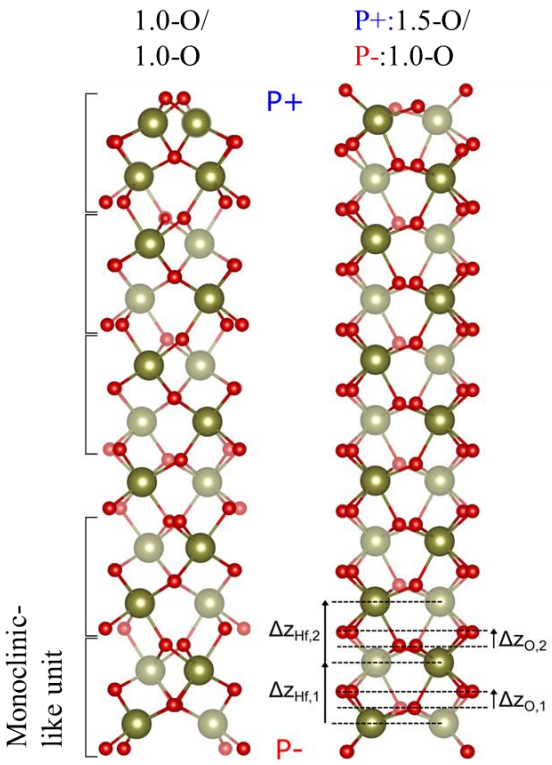

Figure 6.1: Profile view (after ionic relaxation) of 11-Hf-half-layer thick HfO_2 supercell slabs constructed with symmetric (1.0-O/1.0-O) or asymmetric (P+:1.5-O/P−:1.0-O) surface terminations. Green spheres are Hf whereas red spheres are O.

To show how the orthorhombic phase persists across the entire slab, we plot in Figure 6.3 the interlayer spacings between each Hf half-layer to the next, starting at the P− surface and moving towards the P+ surface. The spacings remain close to the bulk orthorhombic value of 2.54 Å. The asymmetric profile of the Hf spacings between the top and bottom surfaces stems from the difference in the composition of the two surfaces. Of note, the inward relaxation of the Hf atoms on the P+ surface (~2.7 % relative to the bulk) likely serves to reduce the positive polarization charge on this surface. Additionally, to compare the polarization of the supercell slabs to the bulk polarization, we plotted in Figure 6.3 the intralayer displacement between the two planes of O atoms within each O half-layer, along the surface-normal coordinate. The polar displacements near

the center lie close to the bulk value (0.55 Å) with larger deviations occurring toward the surface (an indication of enhanced polarization near the surface).

As further evidence of the stable ferroelectric polarization in the asymmetric HfO_2 slab, we note that before ionic relaxation (initialized with a bulk orthorhombic structure) the net electrostatic potential difference between the P− and P+ surface is only -0.09 V [Figure 6.4(b), top panel]. A perfectly screened polarization would have zero difference in the electrostatic potential between surfaces, but a slightly negative value arises from the excess O concentration at the P+ surface. After ionic relaxation, the net electrostatic potential reverses and its magnitude slightly increases to 0.35 V. Later, we showed that thinner HfO_2 slabs can sustain a stronger polarization than the bulk orthorhombic phase. Lastly, unlike the case of symmetric HfO_2 slabs, we observe in the bottom panel of Figure 6.4(b) that the excess electron density accumulating near the P+ surface does not redistribute towards the P− surface after ionic relaxation and in fact grows.

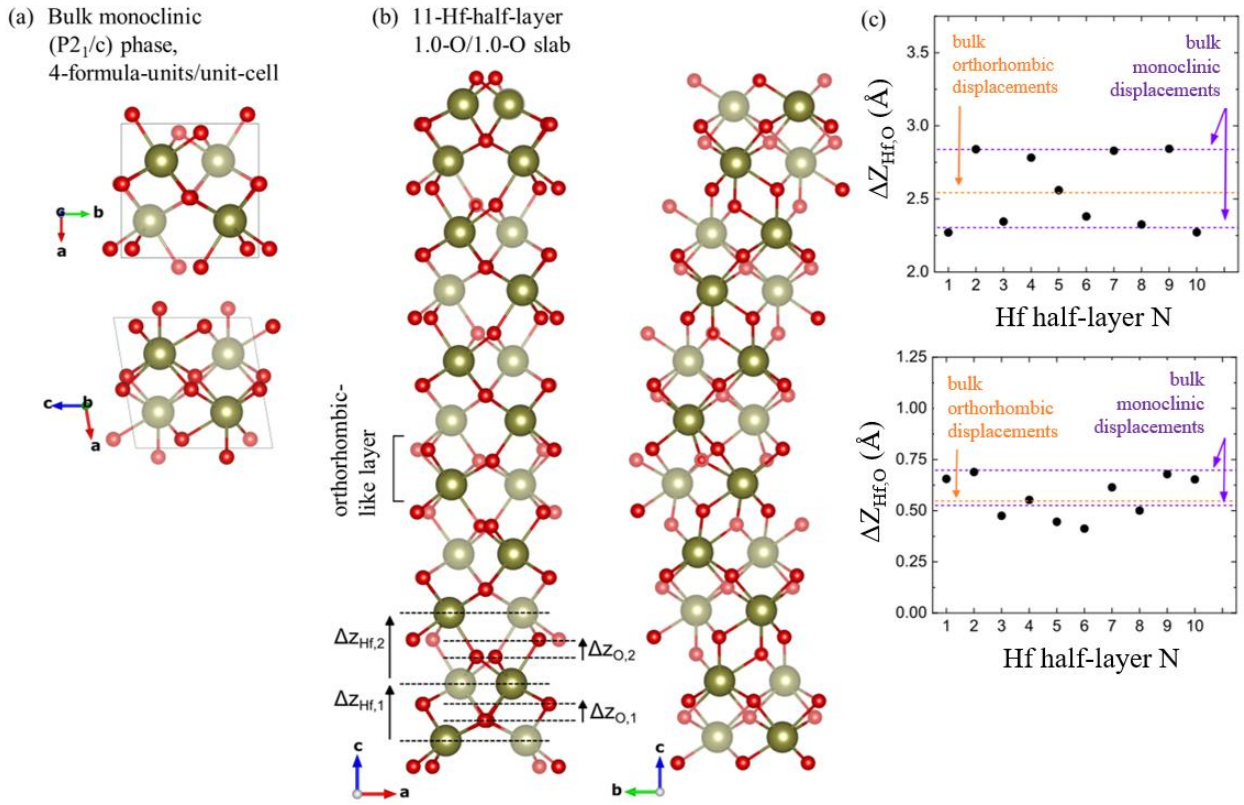

Figure 6.2: (a) Optimized atomic structure of bulk monoclinic ($P2_1/c$) phase looking down the [001] and [010] axis (left and right, respectively). The optimized lattice parameters are a = 5.148 Å, b = 5.198 Å, c = 5.331 Å, α = 90.00°, β = 99.70°, γ = 90.00°. The parameters are close to the experimental values, namely, a = 5.12 Å, b = 5.17 Å, c = 5.29 Å, α = 90.0°, β = 99.1°, γ = **90.0**°. (b) Two profile views (after ionic relaxation) of the symmetric (1.0-O/1.0-O) 11-Hf-half-layer thick HfO_2 supercell slab. Green spheres are Hf whereas red spheres are O. Compare the similarity of the two profiles (rotated by 90° about the c-axis) to that of the bulk monoclinic phase in (a). Note that an orthorhombic-like layer exists at the phase boundary between monoclinic-like units [outlined in the left panel of Figure 6.1] and is present in symmetric slabs with odd number of Hf layers that cannot accommodate a full monoclinic unit cell. (c) Plots of the interlayer distances of each Hf half-layer to the next (left) and intralayer distances between the two O planes within each O half-layer (right) as illustrated in (b) along the direction of the surface normal for the symmetric (1.0-O/1.0-O) 11-Hf-half-layer thick HfO_2 supercell slab. The N^{th} half layer begins at the bottom of the slab. Dashed purple and orange lines show the values from the bulk monoclinic phase in (a) for reference.

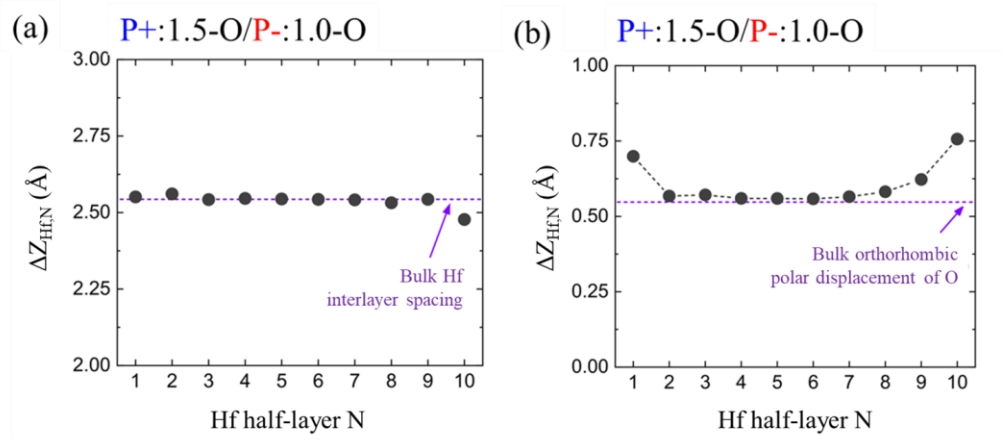

Figure 6.3: (a) Interlayer spacing from one Hf half-layer to the next for asymmetrically terminated slabs along the direction of the surface normal. The N^{th} Hf half-layer begins at the bottom P− surface of the slab as illustrated in Figure 6.1. Dashed purple line shows the bulk value for reference. (b) Intralayer spacing between O planes within each O half-layer for asymmetrically terminated slabs along the direction of the surface normal. Each O half-layer is partitioned into two O planes of two O atoms each and we use the distance of the average z-coordinate of the two O in each plane. Illustration of the measure for this displacement is shown via dashed lines for N = 1 and N = 2 in part (a) of Figure 6.1. Dashed purple line shows the bulk value for reference.

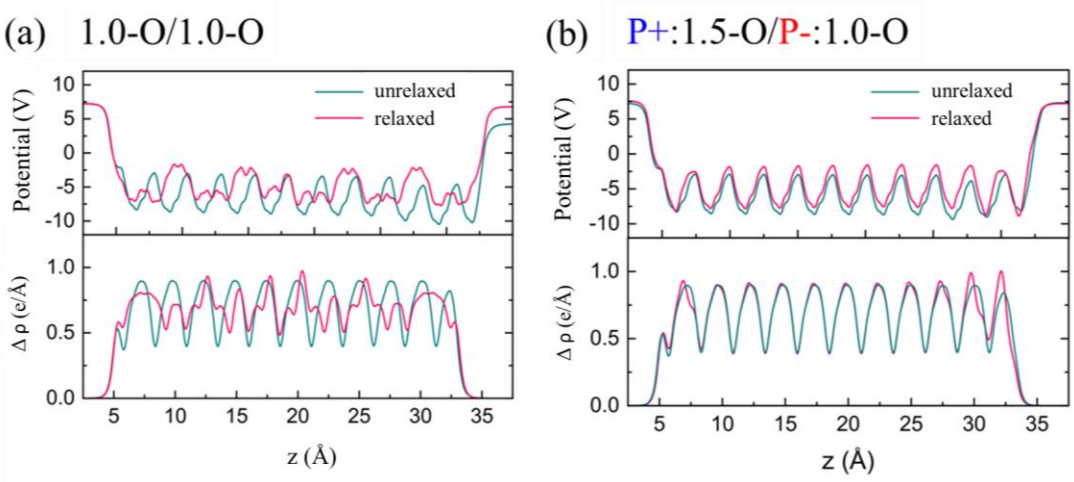

Figure 6.4: Planar-averaged electrostatic potential and planar-integrated electron density (bottom panel) for (a) symmetrically and (b) asymmetrically terminated slabs along the direction of the surface normal, before and after ionic relaxation. The z-coordinate tracks the distance from the middle of the vacuum to the bottom of the slab (P−) surface to the top of the slab (P+) surface and back to the middle of the vacuum. The potentials in the top panels reference to the Fermi level.

6.2 Influence of thickness on the ferroelectric polarization of HfO_2 slabs

We next explore the influence of thickness on the ferroelectric stability of asymmetrically terminated (P+:1.5-O/P-:1.0-O) orthorhombic HfO_2 slabs by constructing additional models with nine, seven, five, and three Hf half-layers. As was done for the case of the asymmetric slab with 11 Hf half-layers in Figure 6.1, we plot the characteristic polar displacement of O across slabs of varying total thickness in Figure 6.3. The displacements near the center resemble the bulk polar displacement O with larger deviations occurring near the surface/ Figure 6.5(b) plots the average values of the polar displacements across the asymmetric slabs, which increase from ~ 10.3% to ~ 26.3% larger than the bulk going from an 11-Hf-half-layer thickness down to five-Hf-half-layer thickness. Conversely, we expect that as the slab thickness increases, this value will approach the bulk limit. Similar behavior of increasing polarization in HfO_2-based thin films with decreasing thickness has been observed – e.g. by Cheema *et al.* in $Hf_{0.8}Zr_{0.2}O_2$ and Lyu *et al*. in $Hf_{0.5}Zr_{0.5}O_2$ thin films (Cheema, Kwon et al. 2020, Lyu, Song et al. 2020).

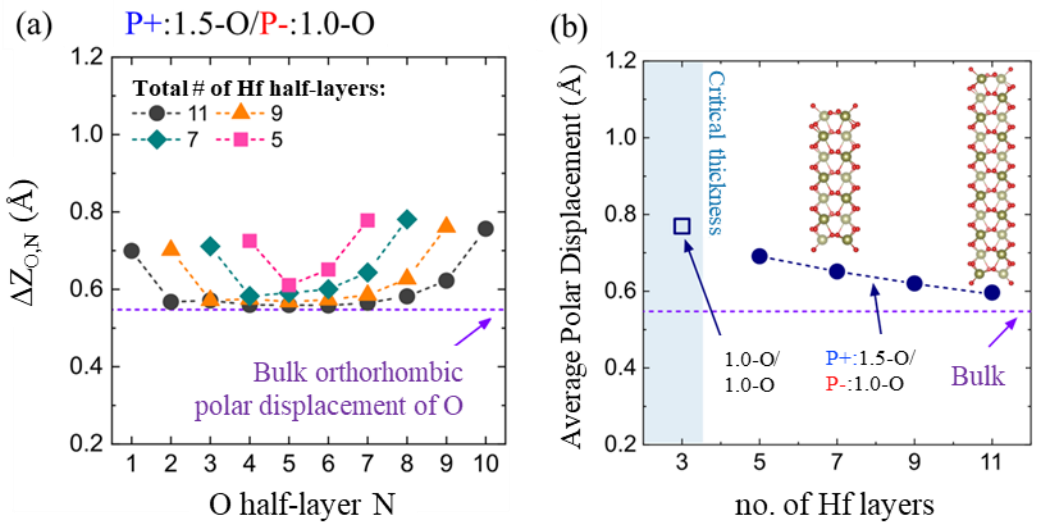

Figure 6.5: (a) Displacement between the two O planes within each O half-layer for asymmetrically terminated polar orthorhombic HfO_2 slabs, $\Delta z_{O,N}$, with varying thickness along the direction of the surface normal [see Figure 6.1(a) for the definition of $\Delta z_{O,N}$]. Dashed purple line shows the bulk value for reference. (b) Average value of the polar displacements of O across the slabs plotted in (a). Dashed purple line provides a comparison to the bulk polar displacement. Inset figures show profile view of 11- and seven-Hf-layer thick slabs (green spheres are Hf whereas red spheres are O). At three Hf layers (labeled "critical thickness") the asymmetric HfO_2 structure. Consequently, we do not plot its average O displacement. In its place, the average polar displacement is plotted for the symmetric slab (whose orthorhombic phase is stable at a three-Hf-layer thickness).

We omitted a comparison for the asymmetric three-Hf-half-layer slab from Figure 6.5(a) and Figure 6.5(b) as the structure undergoes a phase transition that no longer resembles the orthorhombic phase [see Figure 6.2, left] and the characteristic intralayer polar displacements of O in the orthorhombic phase no longer apply. However, the symmetric three-Hf-half-layer thick slab retains a strong bulk-like polarization with an average polar displacement of ~ 40.5% larger than the bulk. We discuss these special cases for both the symmetric and asymmetric three-Hf-half-layer thick slabs further below.

To gain further insight into the stability of polarization, we plot in Figure 6.6 the net electrostatic potential of the HfO_2 slabs before and after ionic relaxation for varying thicknesses,

calculated by subtracting the electrostatic potential in the vacuum near the P+ surface from that of the P− surface. The 1.0-O/1.0-O-terminated HfO_2 slabs (at five- to 11-Hf-half-layer thickness) undergo ionic relaxation that depolarizes the structure to eliminate the otherwise strong, unscreened electrostatic potential [Figure 6.6, open squares]. Note that a residual polarization exists for all the symmetric slabs, even after relaxation. For the five- to 11-layer slabs with an odd number of Hf half-layers, we attribute this to the fact that residual single layer of the polar orthorhombic phase is accommodated in the center of the slab instead of half of a monoclinic-like unit cell even after relaxation [e.g., see Figure 6.2]. By contrast, for a four-Hf-half-layer thick slab (which has the same number of atoms in a monoclinic unit cell), the electrostatic potential drop between the two surfaces reaches ~ 0 V after relaxation (not shown).

Even before relaxation, and in contrast to the symmetric slabs, all of the asymmetric P+:1.5-O/ P−:1.0-O-terminated HfO_2 slabs maintain only a small net electrostatic potential due to the successful screening of the polarization via a nonstoichiometric construction [Figure 6.6, filled dark cyan circles]. With fewer layers, the accumulated dipole moment and associated net electrostatic potential from the ionically screened ferroelectric displacements in each layer becomes more negative. As a result, with decreasing thicknesses prior to relaxation, the magnitude of the net electrostatic potential strengthens from -0.07 V to -0.16 V going from 11- to three-Hf-layers. After relaxation, the direction of the polarization reverses, and as in the unrelaxed case, the slabs retain an increasingly stronger unscreened net electrostatic potential with decreasing thickness (although opposite in direction).

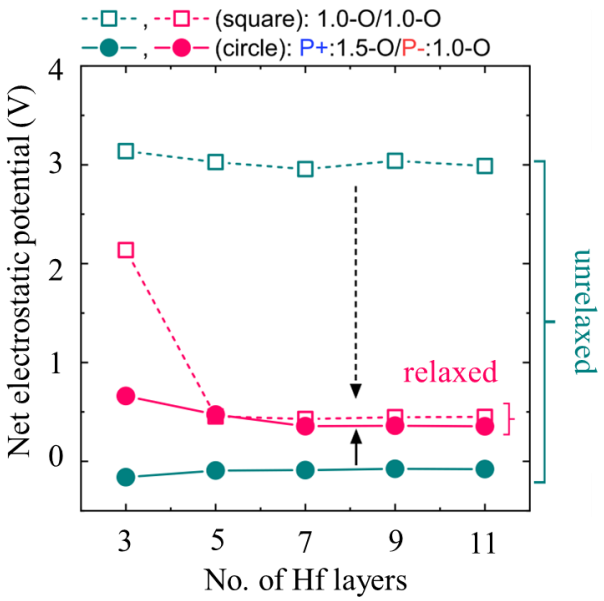

Figure 6.6: Net electrostatic potential as measured by the difference in flat electrostatic potential in the vacuum region of the P− and P+ surfaces as a function of total slab thickness for symmetrically and asymmetrically terminated orthorhombic HfO_2 slabs, before (dark cyan) and after (pink) ionic relaxation.

We next examine the behavior of symmetric and asymmetric HfO_2 slabs at a three-Hf-half-layer thickness [Figure 6.7 displays the profiles]. At this critical thickness, a symmetric HfO_2 slab retains an orthorhombic bulk-like phase after ionic relaxation without depolarization and can support a strong unscreened net electrostatic potential [2.14 V, Figure 6.8], in contrast to thicker symmetric slabs. An unscreened stable ferroelectric polarization can in principle be stable without the need for compensating surface charges to avoid electrostatic divergence, as long as the electrostatic potential energy is smaller than the band gap to avoid dielectric breakdown, which has been predicted to be the case for polar binary oxides below a critical thickness of a few layers (Goniakowski, Noguera et al. 2007, Noguera and Goniakowski 2008). Thus, despite the presence of the unscreened electrostatic potential, the symmetric three-Hf-half-layer thick slab has a calculated band gap of ~2.0 eV [Figure 6.8] and remains insulating throughout its thickness. Note that the slab band gap is lower than the value we previously calculated for bulk orthorhombic HfO_2

(~4.3 eV) (Acosta, Martirez et al. 2021) which is also lower than the measured value 5.25 – 5.95 eV from x-ray photoelectron spectroscopy and spectroscopic ellipsometry for thin-films, as expected (Yu, Li et al. 2002, Zhu, Tamagawa et al. 2002, Modreanu, Hurley et al. 2003, Nguyen, Sayan et al. 2005).

Furthermore, while the asymmetric HfO_2 slab undergoes a phase change at the three-Hf-half-layer thickness, the structure remains polar [Figure 6.6]. This is accompanied by a change in composition at the top (P+) of the slab from 1.5-O to 1.0-O (3 O to 2 O per unit cell) and at the bottom (P-) of the slab from 1.0-O to 1.5-O (2 O to 3 O per unit cell). The structural transformation that the asymmetric HfO_2 slab undergoes at a three-Hf-half-layer thickness resembles the polar rhombohedral phase observed in several other studies of HfO_2-based thin films. Cheema *et al.* pointed out an increasingly rhombic distortion of the $HfZrO_x$ polyhedra in their ferroelectric $Hf_{0.8}Zr_{0.2}O_2$ thin films with decreasing thickness (Cheema, Kwon et al. 2020) and several studies specifically identified the *R*3 and *R*3*m* phases as the rhombohedral polar phase (Wei, Nukala et al. 2018, Nukala, Wei et al. 2020). Figure 6.9 in the SM provides evidence of the structural resemblance of the asymmetric slab at a thickness of three-Hf-half-layers to a bulk *R*3 phase (obtained from Wei *et al.* (Wei, Nukala et al. 2018)). Although comparison between the asymmetric three-Hf-half-layer thick slab and the bulk *R*3 phase is imperfect, differences may be due to the strain imposed by the in-plane lattice parameters kept fixed to the bulk orthorhombic phase in the slab model and the large ionic relaxations that can occur near the surface. Furthermore, the *Pca*2_1 HfO_2(001) surface has inherently higher symmetry, as it contains one-third the number of HfO_2 formula units/surface-area/unit cell compared to the *R*3 $HfO_2(\bar{1}11)$ surface.

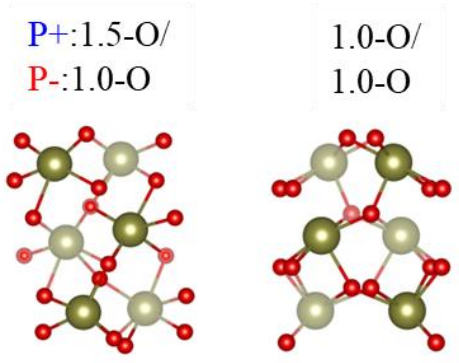

Figure 6.7: Three Hf layer optimized structures for the asymmetric (left) and asymmetric (right) HfO_2 slab structures.

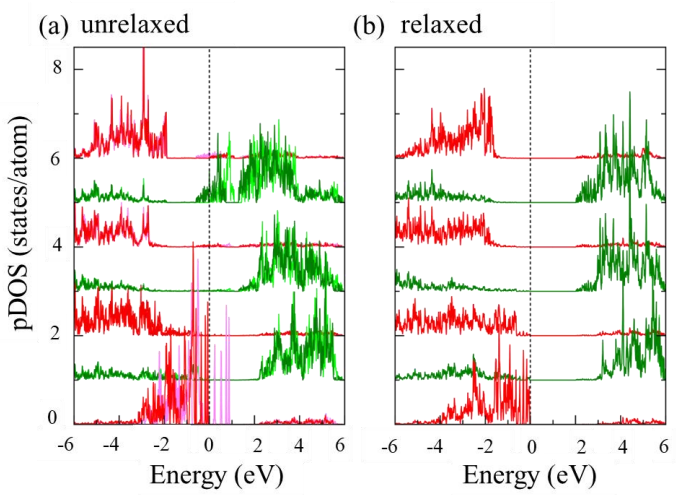

Figure 6.8: Layer-by-layer projected densities of states (pDOS) for a three-Hf-half-layer thick HfO_2 supercell slab with a symmetric (1.0-O/1.0-O) surface composition (a) before and (b) after ionic relaxation. The electronic energies are referenced to the Fermi level (dashed vertical lines denote Energy = 0 eV). The top O layer of the polar orthorhombic slab corresponds to the P+ surface and the bottom O layer corresponds to the P− surface. Hf half-layer spin up/down: green/light green; O half-layer spin up/down: red/pink. The values on the vertical axes are shifted so that the pDOS of the top and bottom layers correspond to the top-most and bottom-most curves

(a) 3-Hf layer (P+:1.5-O/P-:1.0-O) slab, (4-formula-units/unit-cell)

(b) Bulk rhombohedral *(R3)* phase, (12-formula-units/unit-cell)

Figure 6.9: Profile views that highlight the resemblance of (a) a supercell of the asymmetric three-Hf-half-layer thick HfO_2 slab shown in Figure 6.1 and (b) the bulk rhombohedral (*R*3) phase of HfO_2 looking down the [010] axis. Green spheres: Hf, red spheres: O. The predicted lattice parameters of the *R*3 phase shown in (b) are $a = b = 7.19$ Å, $c = 9.106$ Å and $\alpha = \beta = 90.0°$, $\gamma = 120.0°$.

6.3 Extending results to $Hf_{0.5}Zr_{0.5}O_2$

In general, ferroelectricity in $Hf_{0.5}Zr_{0.5}O_2$ thin films (particularly at this 1:1 ratio of Hf:Zr) is experimentally easier to stabilize than ferroelectricity in HfO_2, e.g., under a wider range of conditions or without need for additional small dopants (Muller, Boscke et al. 2012, Park, Kim et al. 2016, Migita, Ota et al. 2018, Shibayama, Nishimura et al. 2018, Cao, Shi et al. 2021). Thus, given the similarity between the orthorhombic HfO_2 and $Hf_{0.5}Zr_{0.5}O_2$ fluorite structures, we extend our study to explore the influence of the surface composition in orthorhombic $Hf_{0.5}Zr_{0.5}O_2$ in a similar fashion.

We first calculate the surface energy landscape of orthorhombic $Hf_{0.5}Zr_{0.5}O_2(001)$ surfaces, where the polarization is normal to the surface. We limited our calculations to O-terminated surfaces because in our prior study on orthorhombic $HfO_2(001)$ surfaces we showed Hf-terminated surfaces to be energetically unstable due to the larger loss of coordination (Acosta, Martirez et al. 2021). Profile views of the slab models with varying O-terminated compositions are shown in Figure 6.10(a).

The surface free energies (as an average of the two surfaces of the slab models) were calculated as a function of temperature and pressure from the Gibbs free energy of our slab models, $\boldsymbol{G^{slab}(T, p, N_{Hf}, N_{Zr}, N_O)}$, using the relation that:

$$\boldsymbol{\gamma_{average} = \frac{1}{2A}\left(G^{slab}(T, p, N_{Hf}, N_{Zr}, N_O) - N_{Hf}\mu_{Hf}(T, p) - N_{Zr}\mu_{Zr}(T, p) - N_O\mu_O(T, p)\right)} \quad (6.1)$$

where N_{Hf}, N_{Zr}, and N_O are the numbers of Hf, Zr, and O atoms in the slab supercell, $\boldsymbol{\mu_{Hf}}$, $\boldsymbol{\mu_{Zr}}$, and $\boldsymbol{\mu_O}$ are the chemical potentials of Hf, Zr, and O atoms, and A is the surface area of one side of the slab. By considering that the Gibbs free energy of bulk $Hf_{0.5}Zr_{0.5}O_2$ can be expressed as:

$$\boldsymbol{g^{bulk}_{Hf_{0.5}Zr_{0.5}O_2}(T, p) = 0.5\mu_{Hf}(T, p) + 0.5\mu_{Zr}(T, p) + 2\mu_O(T, p)}, \quad (6.2)$$

and with the use of the substitution that $N_{Hf} = N_{Zr} = \frac{1}{2}N_{Hf+Zr}$, we can simplify eq. (1) to the following:

$$\boldsymbol{\gamma_{average} = \frac{1}{2A}\left(G^{slab}(T, p, N_{Hf}, N_O) - N_{Hf+Zr}g^{bulk}_{Hf_{0.5}Zr_{0.5}O_2}(T, p) + (2N_{Hf+Zr} - N_O)\mu_O(T, p)\right)}. \quad (6.3)$$

If we know the temperature dependence of the chemical potential of oxygen, $\boldsymbol{\mu_O(T, p^\circ)}$, at one particular reference pressure $\boldsymbol{p^\circ}$, then the entire temperature and pressure dependence can accessed by considering the following Gibbs-Duhem equation for an ideal gas:

$$\boldsymbol{\mu_O(T, p) = \frac{1}{2}\mu_{O_2}(T, p) = \frac{1}{2}\mu_{O_2}(T, p^\circ) + \frac{1}{2}kTln\left(\frac{p}{p^\circ}\right)}, \quad (6.4)$$

where $\boldsymbol{\mu_{O_2}}(\boldsymbol{T}, \boldsymbol{p}^\circ)$ is the chemical potential of O_2 gas at the reference pressure. For further details of the derivation and tabulated values used to calculate the chemical potential of O, see our prior work on the surface energy calculations of HfO_2 surfaces (Acosta, Martirez et al. 2021).

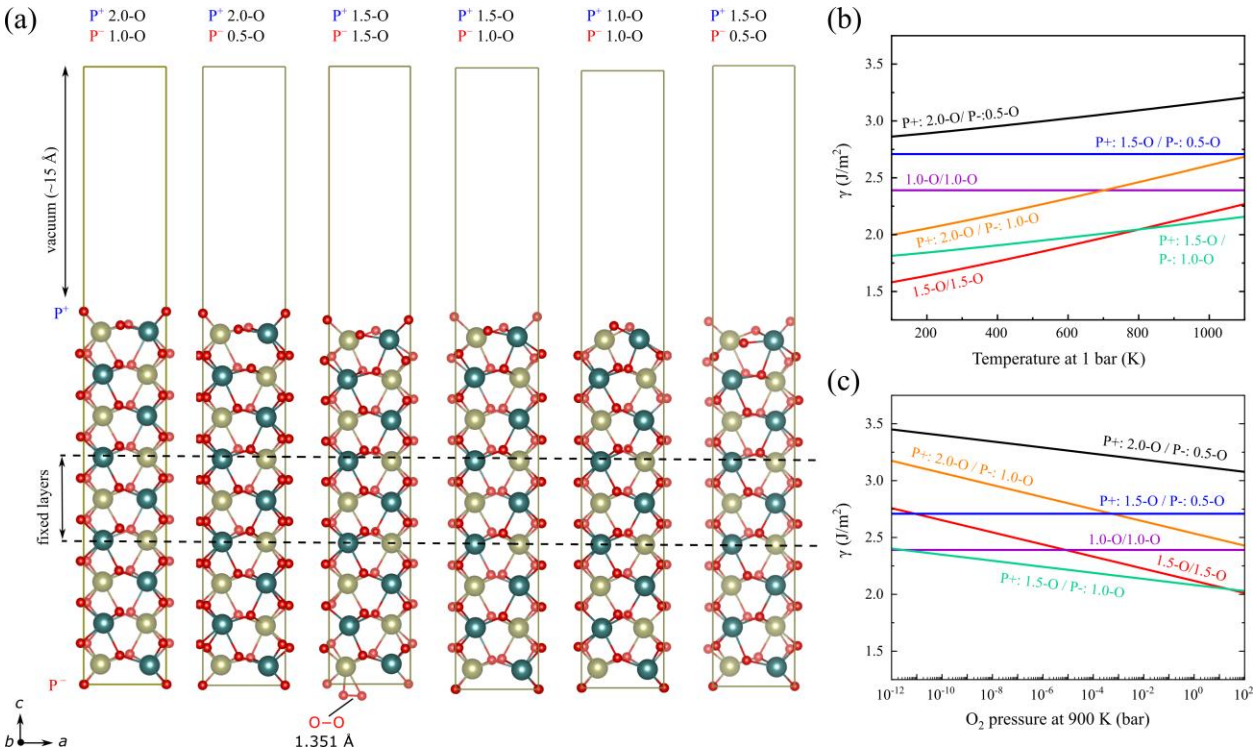

Figure 6.10: (a) Profile views of the relaxed structures for orthorhombic $Hf_{0.5}Zr_{0.5}O_2$ supercell slabs. The composition of the outermost layers in terms of atoms per surface unit cell is labeled for the top and bottom layer above each structure. The middle three Hf/Zr and two O half-layers for all slabs are fixed to their bulk-like arrangement with the polarization direction normal to the surface as labeled. The fainter atoms are farther away from the viewer. Plots of the surface energy as a function of (b) temperature from 100 to 1100 K and (c) pressure from 10^{-12} to 10^{2} bar corresponding to the slabs in (a). See SM for the bulk optimized orthorhombic structure of $Hf_{0.5}Zr_{0.5}O_2$.

The surface energies as a function of temperature and pressure are plotted in Figure 6.10(b) and Figure 6.10(c). We find that the surface energy landscape of orthorhombic $Hf_{0.5}Zr_{0.5}O_2(001)$ surfaces is indeed similar to that of polar orthorhombic $HfO_2(001)$ surfaces that we previously calculated (Acosta, Martirez et al. 2021). At 1 bar, the most stable surface composition is the 1.5-

O/1.5-O surface at low temperatures and P+:1.5-O/P-:1.0-O at high temperatures. However, note that the transition between the two occurs at 800 K for $Hf_{0.5}Zr_{0.5}O_2$ whereas it occurs at 680 K for HfO_2 (Acosta, Martirez et al. 2021). We also note that the surface energies calculated here for the ferroelectric orthorhombic phase of $Hf_{0.5}Zr_{0.5}O_2$ are lower than those calculated by Materlik *et al*. (Materlik, Künneth et al. 2015). For example, they report a calculated value of 2.58 J/m^2 whereas we find the surface energy for the most stable surface composition to be 2.12 J/m^2 at 900 K and 1 bar and not exceed 2.28 J/m^2 at the highest temperature range of 1100 K. In addition to the conceptual difficulties with the phenomological model used by Materlik *et al*. that have been pointed out by Park *et al.* (Park, Lee et al. 2019), we can expect differences from our calculations reported here to arise since they did not perform direct experimental measurements or obtain the values from first principles, but rather extrapolated from the surface energies of nonpolar monoclinic and tetragonal phases of HfO_2 and ZrO_2 phases.

A further significant difference between the $Hf_{0.5}Zr_{0.5}O_2(001)$ and $HfO_2(001)$ surfaces energies is that they are lower by ~6-18% for $Hf_{0.5}Zr_{0.5}O_2$ compared to HfO_2 (calculated by comparing the lowest surface energies across the temperature range of 100 K – 1100 K and 1 bar). Note that while the bulk energy of the polar orthorhombic phase of $Hf_{0.5}Zr_{0.5}O_2$ is also higher than the nonpolar monoclinic phase ($E_{orthorhombic} - E_{monoclinic}$ = 77.1 meV/formula-unit), it is lower than the difference for HfO_2 ($E_{orthorhombic} - E_{monoclinic}$ = 83.2 meV/formula-unit) by 7.3%. The combination of lower relative bulk energy differences and surface energies contribute to the observed greater stability of ferroelectricity in $Hf_{0.5}Zr_{0.5}O_2$ compared to HfO_2 in nanoscale thin films.

After establishing that a $Hf_{0.5}Zr_{0.5}O_2$ slab that is O-rich at the positively polarized surface (P+:1.5-O/P-:1.0-O) is the most stable surface composition at high temperatures and at 1 bar, as in

the case of HfO_2, we further compare the influence of the surface composition to stabilize the polar orthorhombic phase and as a function of the thickness. A plot the characteristic polar displacement of O across $Hf_{0.5}Zr_{0.5}O_2$ slabs of varying total thickness is shown in Figure 6.11(a) obtained in a similar fashion to the case of pure HfO_2.

Similar trends to HfO_2 are found for $Hf_{0.5}Zr_{0.5}O_2$. The average polar displacements at 11-layer thickness for an asymmetric P+:1.5-O/P-:1.0-O slab has a stable polarization larger than the bulk that increases with decreasing thicknesses (~11.8 % at 11-layer thickness to ~ 25.6 % at five-layer thickness) At a three-layer thickness, we find that an asymmetric $Hf_{0.5}Zr_{0.5}O_2$ slab also undergoes a transition to a rhombohedral-like structure, and polarization for a symmetric 1.0-O/1.0-O-terminated stoichiometric $Hf_{0.5}Zr_{0.5}O_2$ slab is also stable and retains its structural resemblance to the bulk orthorhombic phase [Figure 6.11(b)].

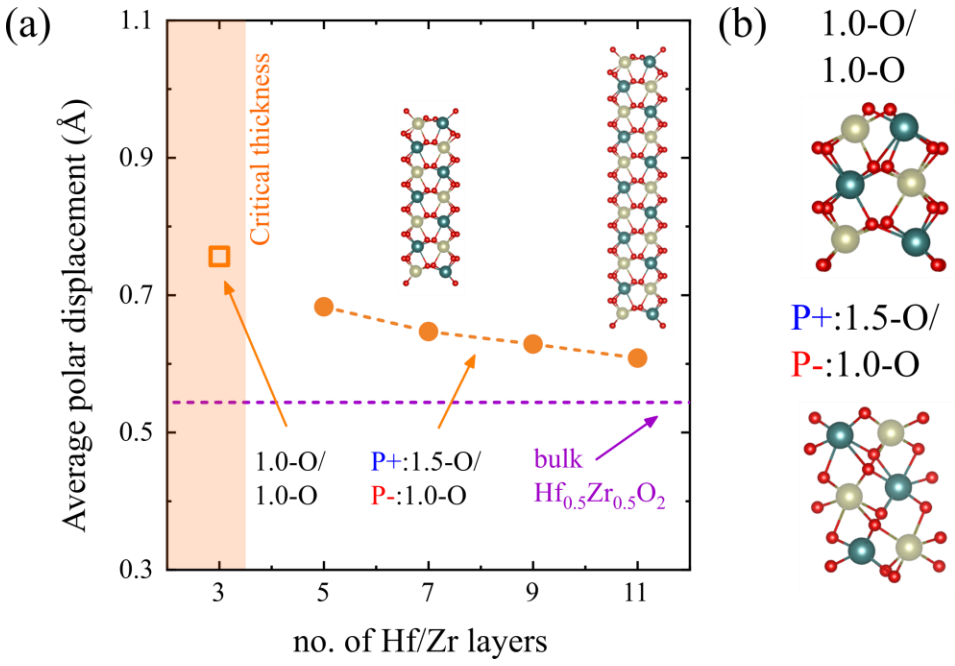

Figure 6.11: (a) Average value of the polar displacements of O for $Hf_{0.5}Zr_{0.5}O_2$ (a). Dashed purple line provides a comparison to the bulk polar displacement. Inset figures show profile view of 11- and seven-layer thick slabs (green spheres are Hf, dark cyan spheres are Zr, and red spheres are O). At three layers (labeled "critical

thickness") the asymmetric $Hf_{0.5}Zr_{0.5}O_2$ structure (shown in bottom panel (b)) deviates significantly from the bulk orthorhombic phase. Thus, as for the case of $Hf_{0.5}Zr_{0.5}O_2$, we do not plot its average O displacement. In its place, the average polar displacement is plotted for the symmetric slab (top panel (b)). Three-layer optimized structures for the symmetric (top panel) and asymmetric (bottom panel) $Hf_{0.5}Zr_{0.5}O_2$ slab structures.

We conclude by remarking that while ferroelectric HfO_2-based thin films down to ~1 nm thickness have been experimentally demonstrated (Cheema, Kwon et al. 2020, Cheema, Shanker et al. 2021), there is variation in experimental reports where the polarization may increase with decreasing thickness only to a certain point before decreasing or vanishing entirely, especially below 5 nm (Hyuk Park, Joon Kim et al. 2013, Migita, Ota et al. 2018, Tian, Shibayama et al. 2018, Lyu, Si et al. 2019, Cao, Shi et al. 2021). Given the variation in experimental reports of the ferroelectric polarization and performance with decreasing thickness, we emphasize the role that the surface or interface composition can play at the nanoscale to stabilize the polarization phase. For example, the work function of the electrodes will play a role in the effectiveness of screening the electrostatic potential and the chemical reactivity of the interface to form an interfacial layer that can degrade the performance adds further complexity.

Furthermore, we note that the stabilization of the orthorhombic phase does not thermodynamically favor the orthorhombic phase over the monoclinic phase at the nanoscale for both HfO_2 and $Hf_{0.5}Zr_{0.5}O_2$. Rather, it raises the energy barrier for the polar orthorhombic to nonpolar monoclinic transition. This is consistent with the current understanding of the kinetic model for stabilization of the orthorhombic phase (e.g., see Park *et al*. (Park, Lee et al. 2019) and Schroeder *et al*. (Schroeder, Park et al. 2022)) where it is the suppression of the transition to the nonpolar monoclinic phase through the optimal engineering of the synthesis and fabrication of HfO_2-based thin films that can achieve the stabilization of the polar phases.

6.4 Summary & outlook

It was found that the surface composition plays a critical role in the ferroelectric stability of orthorhombic HfO_2 and $Hf_{0.5}Zr_{0.5}O_2$ thin films, which can enable stable polarization without a critical thickness limit under an open-circuit boundary condition. At 11-layer thicknesses, surface polarization for stoichiometric HfO_2 and $Hf_{0.5}Zr_{0.5}O_2$ slabs with a symmetric surface composition (1.0-O/1.0-O) is unstable and they depolarize to monoclinic-like phase. In contrast, nonstoichiometric slabs with an O-rich positively polarized surface composition (P+:1.5-O/P−:1.0-O) can retain bulk-like ferroelectric displacements.

It was also found that the polarization increases as the thickness decreases for nonstoichiometric slabs, with five-layer thick slabs reaching ~26 % larger polarization than the bulk for both HfO_2 and $Hf_{0.5}Zr_{0.5}O_2$. The increasingly stronger polarization is enabled by the large band gap that can effectively screen the electrostatic potential of enhanced polarization at the nanoscale. Additionally, at a critical thickness of three layers, we predict that symmetric stoichiometric HfO_2 and $Hf_{0.5}Zr_{0.5}O_2$ slabs can sustain an unscreened ferroelectric polarization with a stable bulk-like orthorhombic phase while the asymmetric nonstoichiometric slabs undergo a phase transition to a polar rhombohedral *R*3-like phase.

The evolution of the polarization and polar distortions with decreasing thickness found here is consistent with recent experimentally reported behavior of ferroelectricity in HfO_2-based thin films (Cheema, Kwon et al. 2020). These results highlight the importance of the surface composition which plays a critical role at the ultrathin thickness limits. Control of the surface composition is a critical mechanism for optimizing the ferroelectric performance of HfO_2-based thin films toward next generation nanoscale applications, e.g., ferroelectric memory and logic devices.

Chapter 7 Summary

Multiferroic and magnetoelectric materials offer the promise of efficient control of magnetism at the nanoscale. The development of efficient composite magnetoelectric devices requires robust stability & performance at the nanoscale that can be a challenge from a materials point-of-view. In this work we discussed two key materials challenges of ferroelectric and ferromagnetic materials toward integration in composite magnetoelectric devices: development of ferromagnetic materials with strong magnetomechanical coupling and ferroelectric materials with robust ferroelectric properties at the nanoscale.

To address the former, we first investigated how the influence of an can be used to enhance the soft magnetic properties of FeGa. It was found that an ~82% decrease in coercivity and ~78% decrease in Gilbert damping coefficient for 100 nm of sputtered FeGa on Si can be achieved using an optimal NiFe underlayer. The underlayer serves to influence the microstructure of the FeGa films, resulting in an increased (110) polycrystalline texture, smaller grain size, and an increase in compressive film strain. We also observed that the saturation magnetostriction is maintained for the FeGa films. Furthermore, we explored a multilayering strategy that uses NiFe as an interlayer to form FeGa/NiFe bilayers was investigated to achieve a composite with a further decrease in coercivity and lower high frequency losses than a single FeGa film or FeGa (100 nm)/NiFe (2.5 nm) bilayer structure. Specifically, a multilayer consisting of a 10 bilayers of FeGa (10 nm) / NiFe (2.5 nm) multilayers yields a magnetic film with a coercivity of 10 Oe and retains a strong uniaxial anisotropy (normalized remnant magnetization of 0.97). Additionally, the 10 bilayer structure exhibits a gilbert damping coefficient of 0.0143 and inhomogeneous broadening linewidth of 73. The addition of Al_2O_3 insulating interlayers in the structure further reduces the coercivity to 6 Oe, and more critically, disrupts eddy currents at high frequency to yield a gilbert damping coefficient

of 0.0143. The multilayering strategy combined with an insulating interlayer is thus shown to be a useful strategy to achieve a composite that meets the necessary criteria of magnetic softness and low loss necessary for integration in magnetoelastic and high frequency antenna devices.

To address the latter, a strategy to control and tailor the stability of ferroelectricity in HfO_2 at the nanoscale was investigated using density functional theory. We found that the surface composition plays a critical role in the ferroelectric stability of orthorhombic HfO_2 thin films, which can enable stable polarization without a critical thickness limit under an open-circuit boundary condition. Surface polarization for a stoichiometric HfO_2 slab with a symmetric surface composition (1.0-O/1.0-O) is unstable and the slab undergoes a transition from an orthorhombic to monoclinic-like phase to depolarize at a thickness of 11-Hf-half-layers. In contrast, a nonstoichiometric HfO_2 slab with an asymmetric surface composition (P+:1.5-O/P−:1.0-O) retains bulk-like ferroelectric displacements at a thickness of 11-Hf-half-layers. The polarization increases as the thickness decreases, with a five-Hf-half-layer thick slab reaching ~ 26.3% larger polarization than the bulk. These results highlight the importance of the surface composition for the stability of ferroelectricity in HfO_2 and points towards control of the surface composition as a mechanism for optimizing the ferroelectric performance of HfO_2-based thin films toward next generation nanoscale applications of ferroelectric materials, e.g., toward multiferroic devices.

At the nanoscale, surfaces and interfaces play an outsized sole in the influence of the functional properties of materials. These results for both the FeGa/NiFe multilayer composite and HfO_2 system highlight the importance of controlling and tailoring the surfaces and interfaces for controlling their desired properties toward integration in magnetoelectric devices with robust and efficient performance.

Appendices

A. Operating procedures

A.1 ULVAC JSP 8000

A.1.1 Safety Precautions

Do not override or bypass any safety interlocks at any time. Only people who are certified or are in supervised training may operate this tool. Always handle hazardous materials carefully and safely.

A.1.2. Emergency shutdown

There is a red emergency switch is on the front of the control cabinet. Press this switch immediately in case of emergency. This will shut down the whole system.

A.1.3. Maintaining vacuum integrity

1. Never touch any part(s) inside the chamber or part(s) going into the chamber with ungloved hands or contaminated gloves.

2. Handle wafer and wafer piece carrier with appropriate vacuum tools or gloved hands.

3. Avoid unnecessary touching/handling of chamber parts and vacuum system tools, even with gloves on.

4. Clean any area or tool which will contact vacuum chamber parts by wiping with lint-free wipes and isopropyl alcohol.

5. The vacuum chamber should not be subjected to excessive atmospheric exposure; pre-

deposition preparation should be done in a timely manner to avoid such exposure.

6. A cleanroom mask must be worn while the chamber is open.

7. Load only clean substrates and clean substrate holder/fixtures into the vacuum chamber.

8. The system is designed to process semiconductor wafers with no films that outgas. Any non-standard substrate such as plastics or unbaked photoresist, must not be put in the system without the area engineer's approval.

A.1.4 Startup Checklist

1. Verify the previous experiments using the tool were successful.

2. Record the base pressure on the log sheet (should be $< 2 \times 10^{-6}$ torr before beginning an experiment, and if pumping down overnight it should be $< 1 \times 10^{-6}$ torr).

3. Verify the cooling water is on and that the tool is in AUTO mode.

A.1.5. Creating a recipe

1. Click the RECIPE tab to enter the recipe editing window

2. Click LOAD for a list of available recipes.

3. Select the appropriate recipe and edit the parameters as needed. The process parameters that will impact film quality directly are power, argon flow rate, and the substrate temperature. Generally, the plasma should be ignited with 50 sccm of argon flow and 100 W power by checking the "Cathode Discharge" box specific to the material during that step.

4. For insulating targets, the power should be ramped up slowly in 20 W increments to avoid thermal shock that may lead to cracking the target.

5. Ensure that substrate rotation is checked for every step of the process, or there will be an error.

6. Prior to each run, the target should be run with the shutter closed to remove the surface oxidation or cross-contamination from other targets. This time should be at least 15 minutes if the target has just been installed and 5 minutes otherwise.

7. Ensure that during the deposition step the corresponding cathode shutter box is checked.

A.1.6. Heated deposition

1. Heat in 25°C increments with a step length of 200 seconds.

2. Set the “Sub Heating Speed” to 10

3. On every step but the first heating step, check the “Sub Heating Temp Check” box so that the temperature setpoint will be reached.

4. After deposition, the substrates take 8 hours to cool.

5. When changes to the recipe are complete, save it. If modifying from another recipe, make sure to “Save As” a new file name.

A.1.7. Mounting a sample

1. The 8 inch substrate holder can hold up to four 4 inch wafers, but the most consistent uniformity is achieved when the samples are positioned halfway between the center and edge around the holder. Sample placement suggestions are shown below.

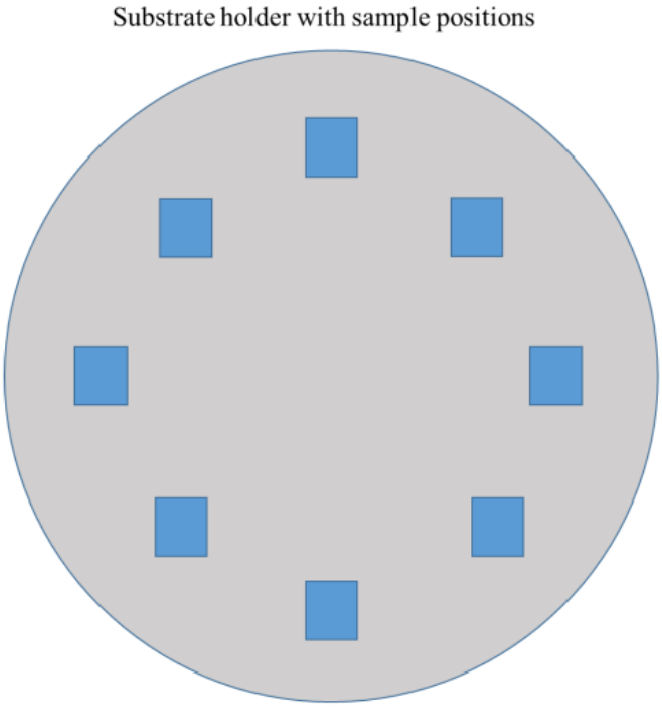

2. Mount the samples with Kapton tape for depositions below 150°C in the configuration shown above depending on the substrate.

3. If the substrate is flaking metal, it can be cleaned by carefully scraping the surface with a razor blade and vacuuming the particles with the CHA vacuum. Otherwise, contact the engineer in charge for help cleaning it.

5. If in situ magnetic biasing is desired, use the substrate located on the second to last shelf in the cabinet next to the sputtering table. It is a 6 inch aluminum plate that fits into the outer ring of the high temperature substrate holder. The samples can be positioned between the magnets in various positions to adjust the field from 50 Oe up to 1000 Oe. Verify the field with the magnetometer and position samples accordingly.

A.1.8. Loading the substrate

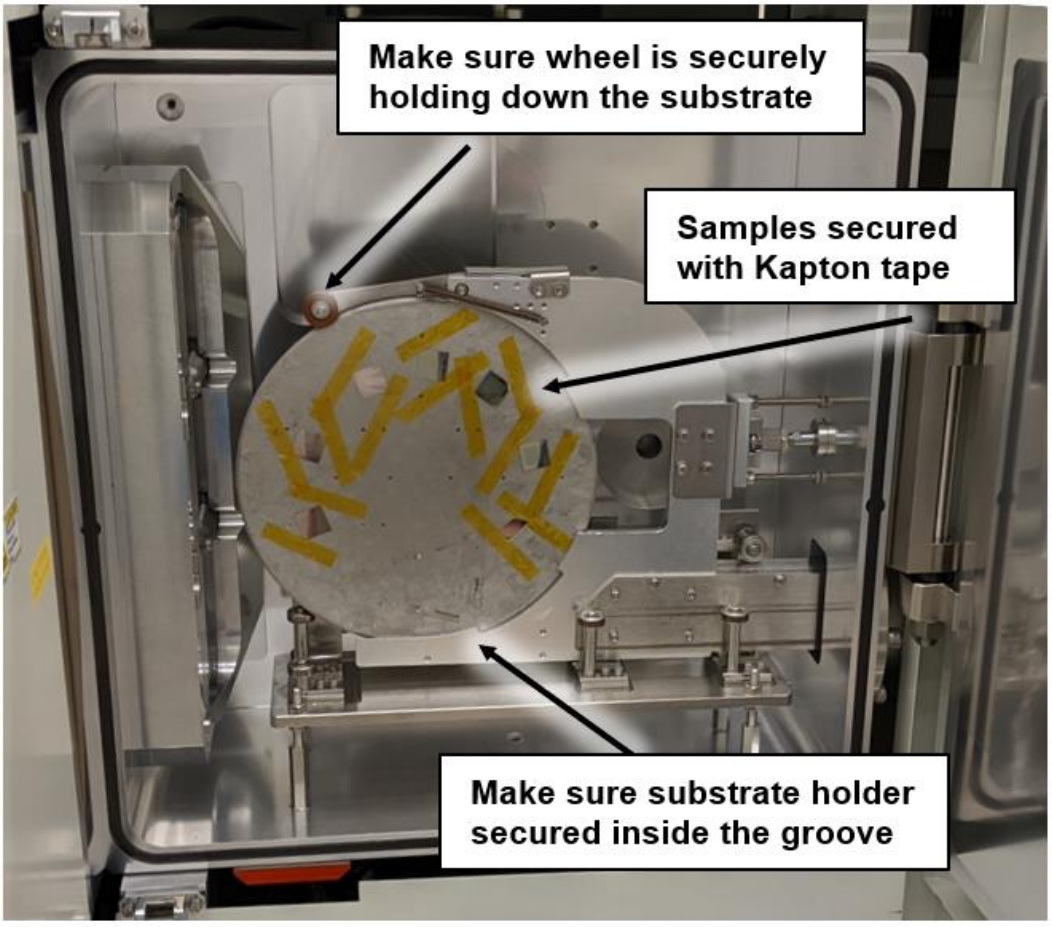

1. Sign in on Labrunner to disable the interlock, which will prevent the preparation chamber from fully venting

2. Select the MAIN tab, click PREP VENT then YES to the pop-up window

3. After the preparation chamber vents fully, indicated by the ATM PRESSURE sign, use the two latches to open the chamber.

4. Make sure the door does not swing closed, as this will require the interlock to be reset.

5. Remove the substrate holder and load the new one, making sure the wheel is down and that it fits securely into the transfer arm. If the wheel is not in place, the substrate will fall in the deposition chamber and will require the system to be vented.

6. Check the O-ring around the chamber door for debris and wipe if necessary

7. Close the door and secure the latches.

8. From the ALARM tab, click ALARM RESET, then YES in the pop-up

9. Ensure that the red warning has changed to black.

A.1.9. Deposition

1. Click the MAIN tab.

2. From the ALARM tab, click ALARM RESET, then YES in the pop-up.

3. Select TRANS MODE and VENT MODE.

4. TRANS MODE will dictate if the substrate holder will be transferred to the preparation chamber after. VENT MODE will dictate whether the preparation chamber

will vent once the substrate holder has been transferred to it. For overnight runs and air sensitive samples, turn off VENT MODE.

5. Click RECIPE SELECT and load the desired recipe. Listing the recipes by date modified will make this easier.

6. Verify the desired recipe by the NAME box.

7. Click RUN to begin the process.

8. The tool will pump down the preparation chamber (<100 mTorr), load the sample into the Deposition Chamber, pump down to the predeposition process base pressure (5×10^{-6} torr), deposit material, unload sample back to the Preparation Chamber and finally vent the Preparation Chamber.

9. Copy the deposition parameters in to the logbook. Verify that the shutters open fully by peering into the viewport on the left side of the chamber.

10. Once the deposition is completed and the preparation chamber is vented, open both latches and remove the substrate.

11. Replace with the empty substrate, close the door and latches, then reset the alarm.

12. On the MAIN tab, select PREP > EVAC then YES in the pop-up

13. Wait until pumpdown (< 100 mTorr) and for the EVAC field to turn red

14. Select DEPO > EVAC, then YES in the pop-up to resume pumping the deposition chamber.

A.1.10. Troubleshooting

1. Discharge Error Alarm

a) Recipe error: There is an incorrect value for power or pressure that makes the plasma unsustainable (generally very low values). Adjust this and try to rerun the recipe.

b) Shutter issue: When carrying out multilayer depositions, the shutters opening and closing can result in the plasma to cut out at very low deposition pressures. Adjust the pressure to make sure the targets ignite individually.

c) Power supply: It's possible that the power supply was switched off accidentally by a CHA user vacuuming their chamber. Check to make sure all are on and operational.

4) Electrical short: There is a short between the cathode and the target. This can be caused by a flake of metal attracted to the strong magnets behind the target. Verify the issue by restarting the run and looking at the current and voltage for each cathode. If the current goes very high (> 1 A), a short has occurred, the deposition chamber will need to be vented and the cathodes need to be inspected by ISNC technicians.

2. Sub Rotate Alarm

a) Recipe error: The simple case is that the substrate rotation box in the recipe isn't selected for one of the steps.

b) Contact ISNC technician if it's not a recipe error.

A.2 MPMS3 SQUID Magnetometer

A.2.1. Safety Precautions

1. Long pants and close-toed shoes are required to enter the SQUID room

2. Avoid the area marked with red tape as there is a small magnetic field that exists due to the electromagnet.

3. If refilling liquid He, ensure that insulated gloves are used to avoid cryogenic burns.

A.2.2. Startup

1. Take the system out of standby mode and set to the desired temperature.

2. If going to fields over 1 T, ensure that the He level is over 50%.

A.2.3. Preparing a sample

1. Cleave a piece of sample that is roughly 5 x 5 mm^2.

2. This size can be used for both in-plane (IP) and out-of-plane (OOP) measurements.

3. If only IP is needed, cleave a sample that is 5 x 6.5 mm, which can fit in the straw without any additional tape.

4. Cut a straw in half (use clear plastic drinking straws with no bend).

5. In-plane sample mounting:

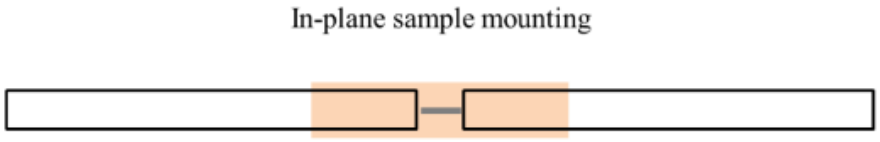

a) Take one straw half and rotate it so the cut end is away from the sample.

b) Cut a 6 cm piece of 1 cm wide Kapton™ tape and lay it with the adhesive side facing up.

c) Place the straw slightly less than halfway down the tape.

d) Place the sample on its edge so it is touching the edge of the straw.

e) Place the other half of the straw touching the other edge and then wrap the edges of the tape around.

f) Place another 6 cm piece of tape on the top of the sample and wrap the edges.

6. Out-of-plane sample mounting

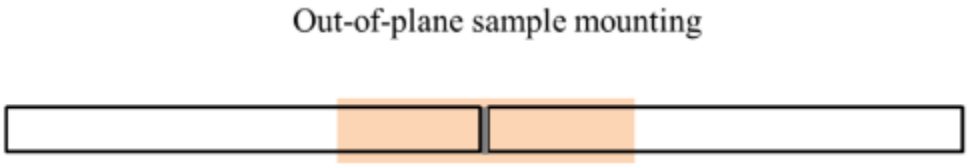

a) Take one straw half and rotate it so the cut end is away from the sample.

b) Cut a 6 cm piece of 1 cm wide Kapton™ tape and lay it with the adhesive side facing up.

c) Place the straw halfway down the tape.

d) Place the sample on its edge so its face is touching the edge of the straw.

e) Place the other half of the straw touching the back side and then wrap the edges of the tape around.

f) Place another 6 cm piece of tape on the top of the sample and wrap the edges.

A.2.4. Loading the sample

1. In the SQUID program window, select Sample > Remove. This will vent the sample space.

2. Remove the black cap and using the threaded top portion, remove the flexible sample rod.

3. If it has another users sample on it, place the sample by the keyboard of the computer

4. Fix the sample to the bottom of the sample rod and place the small black end piece on the end of the straw to prevent the sample from falling into the instrument.

5. Insert the sample rod into the chamber and then press the small black button.

A.2.5. Centering the sample

1. Set a saturating magnetic field.

2. Center the sample position by clicking Center > RSC.

3. Initialize the transport of the sample.

4. Run a centering scan. Based on the position of the sample described in the previous section, the center should be around 3.5 cm.

A.2.6. Running a scan

1. Input desired parameters for collecting data points in the sequence file.

2. Click on Play to start SQUID measurement.

A.3 MATLAB script to process raw data collected from VNA-stripline set-up shown in Figure 2.10

```
%% Load data, here you have to put the names of the files and substitute filename below
load('filename frequencyArray.mat')
load('filename magneticField.mat')
load('filename S11Mag.mat')

gamma = 28024.95164e6;
Meff = 513*(0.03)*(0.03)*(0.0000030);
fluxData = fluxData;
fkittel = (sqrt(fluxData.*(fluxData + Meff))).*gamma;

%% muclest transpose data to put frequency on the x-axis
fluxDataOe = 10000.*fluxData;
[X,Y] = meshgrid(freqArray,fluxDataOe); %meshgrid data
X = transpose(X);
Y = transpose(Y);
[m,n] = size(X); %get size of an array

%% Transform S parameters to absorption
S11abs = 100.*(1-10.^(S11MagData/10));
% wait until after this to subtract housing (use S11abs)
```

```
% Subtract background noise S11
% Remove high field background noise

S11_subtracted = zeros(m,n);
for j = 1:n
   for i = 1:m
      S11_subtracted(i,j) = S11abs(i,j) - S11backgroundMin(i);
   end
end

% Remove high field background once more
for j = 1:n
   for i = 1:m
      if S11_subtracted(i,j) < 0
         S11_subtracted(i,j) = S11_subtracted(i,j) - S11_subtracted(i,j);

      end
   end
end

%% Convert subtracted data back to dB
S11subtracteddB = S11_subtracted/100;
```

```
S11subtracteddB = 10.*log10(S11subtracteddB);


%% S11 plot
fig1 = figure(1);
ax = gca;
S11plot = surf(X,Y,S11_subtracted);
set(S11plot,'LineStyle','none');
title('S_1_1 absorption (%)');
x2 = xlabel('Frequency');
y2 = ylabel('Magnetic field (Oe)');
set(gcf,'numbertitle','off','name','S11 absorption (%)');
view(2);
% hold all;
% xlim([1e9,10e9]);
% plot(fkittel,fluxDataOe, 'k-','LineWidth',1 );
colorbar;
% caxis([0 1.0]); % this will depend on the range of your data collection


%% Mag plot
fig1 = figure(2);
ax = gca;
S11plot = surf(X,Y,S11MagData);
set(S11plot,'LineStyle','none');
```

```
title('S11 dB');
x2 = xlabel('Frequency');
y2 = ylabel('Magnetic field (Oe)');
set(gcf,'numbertitle','off','name','S11 dB');
view(2);
% hold all;
% xlim([1e9,10e9]); % this will depend on the range of your data collection
% plot(fkittel,fluxDataOe, 'k-','LineWidth',1 );
colorbar;


frequencies = 10^9*[6 7 8 9 10 11 12 13 14 15]; % this will depend on the range of your data
collection
for i = 1:length(frequencies)
    % find index of desired frequency
    index_freq(i) = sum(freqArray < frequencies(i));
end


S11_vsField = S11_subtracted(index_freq,:)';
save('S11_formatted','freqArray','S11_vsField');


%Plot S11_vsField
var1 = zeros(length(S11_vsField(1)));
for i = 1:length(S11_vsField)
```

```
    var1(i) = i*2;
end
plot(var1,S11_vsField)
xlabel('Magnetic Field (Oe)');
ylabel('Absorption (%)');
```

B. VASP DFT INCAR Scripts

B.1 Bulk HfO_2 models

```
System = bulk HfO2
 ISTART = 1         ! 0: scratch
 ICHARG = 1        ! initialize density
 NPAR   = 4          ! parallelize over bands
 NCORE  = 32       ! parallelize over FFT
Electronic parameters:
 INIWAV = 1        ! initialize wavefunction with random coefficients
 NELM   = 120        ! maximum SCF iterations
 NELMDL = -4     ! delay iterations during SCF
 NELMIN = 1        ! minimum number of SCF iterations at each ionic state
 ISMEAR = -5       ! Smearing: Gaussian (0), Tetrahedron method with Blochl correction (-5)
 SIGMA  = 0.01     ! width of smearing (in eV)
 ISYM   = 0          ! 0=no sym; 1=full sym; 2=fast sym (default)
 LREAL  = .FALSE.   ! projection operators done in real space
```

```
 LPLANE = .FALSE.

 ADDGRID = .FALSE.

 LASPH = .TRUE.

 GGA_COMPAT = .FALSE. ! no back compatibility when FALSE


Spin settings:

 ISPIN    = 2            ! spin-polarized calculation

 LMAXMIX  = 4       ! maximum l-quantum number passed to charge density mixer

 AMIX     = 0.1        ! linear mixing parameter

 BMIX     = 0.01       ! cutoff wave vector for Kerker mixing scheme

MAXMIX = 60


Electronic convergence settings:

 EDIFF  = 1e-07          ! electronic convergence criterion

 EDIFFG = -0.001        ! force convergence threshold

 PREC   = Accurate

 ENCUT  = 800           ! kinetic energy cutoff

 ALGO   = Fast          ! Blocked Davidson and then RMM-DIIS


Ionic convergence settings:

 IBRION = 1          ! Optimization method

 ISIF   = 3          ! 1 or 2 = relax atomic coordinates, 3 = relax atoms and V

 NSW    = 100        !  number of ionic steps
```

```
 POTIM  = 0.3


Output settings:
 LWAVE  = .TRUE.     ! write WAVECAR file
 LCHARG = .TRUE.    ! write CHGCAR file
! LVTOT  = .FALSE.
! LVHAR  = .TRUE.
 LORBIT = 11              ! calculate PDOS, see magnetic moments


! Dipole correction:
! IDIPOL = 3
! LDIPOL = .TRUE.       ! switch on dipole corrections
! DIPOL = 0 0 0            ! center of mass of the slab as a fraction of the slab
```

B.1 Slab HfO_2 models

```
System = HfO2 slab
 ISTART = 1           ! 0: scratch
 ICHARG = 1          ! initialize density
 NPAR   = 4           ! parallelize over bands
 NCORE  = 32         ! parallelize over FFT


Electronic parameters:
 INIWAV = 1            ! initialize wavefunction with random coefficients
```

```
 NELM   = 120          ! maximum SCF iterations
 NELMDL = -4           ! delay iterations during SCF
 NELMIN = 4            ! minimum number of SCF iterations at each ionic state
 ISMEAR = 0            ! Gaussian (0), Tetrahedron method with Blochl correction (-5)
 SIGMA  = 0.01         ! width of smearing (in eV)
 ISYM   = 2            ! 0=no sym; 1=full sym; 2=fast sym
 LREAL  = Auto         ! projection operators done in real space
 LPLANE = .FALSE.
 ADDGRID = .FALSE.
 LASPH = .TRUE.
 GGA_COMPAT = .FALSE. ! no back compatibility when FALSE


Spin settings:
 ISPIN    = 2                ! spin-polarized calculation
 LMAXMIX  = 4                ! maximum l-quantum number passed to charge density mixer
 AMIX     = 0.1              ! linear mixing parameter
 BMIX     = 0.01             ! cutoff wave vector for Kerker mixing scheme
 MAXMIX = 60


Electronic convergence settings:
 EDIFF  = 1e-06          ! electronic convergence criterion
 EDIFFG = -0.01          ! force convergence threshold
 PREC   = Accurate       ! ROPT 2.5E-4
```

```
 ENCUT  = 800          ! kinetic energy cutoff
 ALGO   = Fast         ! Blocked Davidson and then RMM-DIIS


Ionic convergence settings:
 IBRION = 2          ! Optimization method
 ISIF   = 1          ! 1 or 2 = relax atomic coordinates, 3 = relax atoms and V
 NSW    = 100        ! number of ionic steps
 POTIM  = 0.3


Output settings:
 LWAVE  = .TRUE.     ! write WAVECAR file
 LCHARG = .TRUE.     ! write CHGCAR file
LORBIT = 11          ! calculate PDOS, see magnetic moments


Dipole correction:
 IDIPOL = 3
 LDIPOL = .TRUE.      ! switch on dipole corrections
 DIPOL = 0 0 0.35     ! center of mass of the slab as a fraction of the slab
```

Bibliography

Abe, T., et al. (2018). "Fe-Al alloy single-crystal thin film preparation for basic magnetic measurements." AIP Advances **8**(4): 047710.

Acosta, A., et al. (2021). "Relationship between ferroelectric polarization and stoichiometry of HfO2 surfaces." Physical Review Materials **5**(12): 124417.

Aldridge, R. and S. Raeburn (1976). "The Hall effect of thin iron films." Physics Letters A **56**(3): 211-212.

Ariake, Y., et al. (2017). "The thickness dependence of soft magnetic properties of (FeCo)-Al alloy thin films." IEEE transactions on Magnetics **53**(11): 1-4.

Atulasimha, J. and A. B. Flatau (2011). "A review of magnetostrictive iron–gallium alloys." Smart Materials and Structures **20**(4): 043001.

Avery, A., et al. (2015). "Thermal and electrical conductivity of approximately 100-nm permalloy, Ni, Co, Al, and Cu films and examination of the Wiedemann-Franz Law." Physical Review B **92**(21): 214410.

Bader, R. (1990). "Atoms in Molecules: A Quantum Theory Oxford University." Press: Oxford,, nº UK.

Bailey, G. and C. Vittoria (1973). Temperature Dependence of the FMR Linewidth in Single Crystal Ni Platelets. AIP Conference Proceedings, AIP.

Blöchl, P. E. (1994). "Projector augmented-wave method." Physical Review B **50**(24): 17953.

Bogue, R. (2014). "Towards the trillion sensors market." Sensor Review **34**(2): 137-142.

Böscke, T., et al. (2011). "Ferroelectricity in hafnium oxide thin films." Applied Physics Letters **99**(10): 102903.

Buragohain, P., et al. (2018). "Nanoscopic studies of domain structure dynamics in ferroelectric La: HfO2 capacitors." Applied Physics Letters **112**(22): 222901.

Camley, R. E., et al. (2015). Magnetism of surfaces, interfaces, and nanoscale materials, Elsevier.

Cao, J., et al. (2021). "An overview of ferroelectric hafnia and epitaxial growth." physica status solidi (RRL)–Rapid Research Letters **15**(5): 2100025.

Chase, M. W. (1996). "NIST-JANAF thermochemical tables for oxygen fluorides." Journal of Physical and Chemical Reference Data **25**(2): 551-603.

Cheema, S. S., et al. (2020). "Enhanced ferroelectricity in ultrathin films grown directly on silicon." Nature **580**(7804): 478-482.

Cheema, S. S., et al. (2021). "One Nanometer HfO2-Based Ferroelectric Tunnel Junctions on Silicon." Advanced Electronic Materials: 2100499.

Cheng, Y., et al. (2018). "Recent development and status of magnetoelectric materials and devices." Physics Letters A **382**(41): 3018-3025.

Chu, Z., et al. (2018). "Review of multi-layered magnetoelectric composite materials and devices applications." Journal of Physics D: Applied Physics **51**(24): 243001.

Cimpoesu, D., et al. (2019). "doFORC tool for calculating first-order reversal curve diagrams of noisy scattered data." Journal of Applied Physics **125**(2): 023906.

Clark, A., et al. (1988). "Magnetostriction ‘‘jumps’’in twinned Tb0. 3Dy0. 7Fe1. 9." Journal of Applied Physics **63**(8): 3910-3912.

Clark, A. E., et al. (2001). "Effect of quenching on the magnetostriction on Fe/sub 1-x/Ga/sub x/(0.13 x< 0.21)." IEEE transactions on Magnetics **37**(4): 2678-2680.

Cohen, R. E. (1997). "Surface effects in ferroelectrics: Periodic slab computations for BaTiO3." Ferroelectrics **194**(1): 323-342.

Cook, B., et al. (2000). "Electrical and thermal properties of Tb 0.3 Dy 0.7 Fe 2− x." Journal of Applied Physics **87**(2): 776-780.

Cooke, M., et al. (2001). "Sputter deposition of compositional gradient magnetostrictive FeCo based thin films." Journal of Magnetism and Magnetic Materials **237**(2): 175-180.

Cramer, C. J., et al. (2003). "Variable character of O—O and M—O bonding in side-on (η2) 1: 1 metal complexes of O2." Proceedings of the National Academy of Sciences **100**(7): 3635-3640.

Danan, H., et al. (1968). "New determinations of the saturation magnetization of nickel and iron." Journal of Applied Physics **39**(2): 669-670.

Darwent, B. d. (1970). "Bond dissociation energies in simple molecules."

De Lacheisserie, E. d. T. and J. Peuzin (1994). "Magnetostriction and internal stresses in thin films: the cantilever method revisited." Journal of Magnetism and Magnetic Materials **136**(1-2): 189-196.

Díaz, J., et al. (2012). "Determination of the magnetostrictive atomic environments in FeCoB alloys." Physical Review B **85**(13): 134437.

Dmitriyeva, A., et al. (2021). "Magnetoelectric Coupling at the Ni/Hf0. 5Zr0. 5O2 Interface." ACS nano **15**(9): 14891-14902.

Eerenstein, W., et al. (2006). "Multiferroic and magnetoelectric materials." **442**(7104): 759.

Fiebig, M. J. (2005). "Revival of the magnetoelectric effect." Journal of Physics D: Applied Physics **38**(8): R123.

Fields, S. S., et al. (2021). "Metal Nitride Electrode Stress and Chemistry Effects on Phase and Polarization Response in Ferroelectric Hf0. 5Zr0. 5O2 Thin Films." Advanced Materials Interfaces: 2100018.

Fullerton, E. E., et al. (1999). "Hard/soft magnetic heterostructures: model exchange-spring magnets." Journal of Magnetism and Magnetic Materials **200**(1-3): 392-404.

Gao, J., et al. (2009). "The effect of boron addition on the atomic structure and microwave magnetic properties of FeGaB thin films." Journal of Applied Physics **105**(7): 07A323.

Gao, X., et al. (2008). "Magnetomechanical behaviors of giant magnetostrictive materials." Acta Mechanica Solida Sinica **21**(1): 15-18.

Garrity, K., et al. (2013). "Ferroelectric surface chemistry: First-principles study of the PbTiO 3 surface." Physical Review B **88**(4): 045401.

Gattinoni, C., et al. (2020). "Interface and surface stabilization of the polarization in ferroelectric thin films." Proceedings of the National Academy of Sciences **117**(46): 28589-28595.

Goniakowski, J., et al. (2007). "Prediction of uncompensated polarity in ultrathin films." Physical Review Letters **98**(20): 205701.

Gontarz, R., et al. (1964). "Magnetostriction of Thin Ni-Films." physica status solidi (b) **6**(3): 909-912.

Grössinger, R., et al. (2014). Materials with high magnetostriction. IOP Conference Series: Materials Science and Engineering, IOP Publishing.

Guyonnet, J. (2014). Ferroelectric Domain Walls: Statics, Dynamics, and Functionalities Revealed by Atomic Force Microscopy, Springer Science & Business Media.

Hamouda, W., et al. (2020). "Physical chemistry of the TiN/Hf0. 5Zr0. 5O2 interface." Journal of Applied Physics **127**(6): 064105.

He, J., et al. (2012). "Electronic surface compensation of polarization in PbTiO3 films." Journal of Applied Physics **112**(5): 054112.

Heavens, O. S. (1991). Optical properties of thin solid films, Courier Corporation.

Henkelman, G., et al. (2006). "A fast and robust algorithm for Bader decomposition of charge density." Computational Materials Science **36**(3): 354-360.

Hida, R., et al. (2018). "Nanolaminated FeCoB/FeCo and FeCoB/NiFe soft magnetic thin films with tailored magnetic properties deposited by magnetron sputtering." Journal of Magnetism and Magnetic Materials
453: 211-219.

Hoffmann, M., et al. (2015). "Stabilizing the ferroelectric phase in doped hafnium oxide." Journal of Applied Physics **118**(7): 072006.

Hohenberg, P. and W. Kohn (1964). "Inhomogeneous electron gas." Physical Review **136**(3B): B864.

Hsain, H. A., et al. (2020). "Compositional dependence of crystallization temperatures and phase evolution in hafnia-zirconia (HfxZr1− x) O2 thin films." Applied Physics Letters **116**(19): 192901.

Huan, T. D., et al. (2014). "Pathways towards ferroelectricity in hafnia." Physical Review B **90**(6): 064111.

Huang, B., et al. (2012). "Direct observation of ferroelectric polarization-modulated band bending at oxide interfaces." Applied Physics Letters **100**(12): 122903.

Hyuk Park, M., et al. (2013). "Evolution of phases and ferroelectric properties of thin Hf0. 5Zr0. 5O2 films according to the thickness and annealing temperature." Applied Physics Letters **102**(24): 242905.

Imran, S., et al. (2018). "FeGaB (25 nm)/Al2O3/FeGaB (25 nm) Multilayer Structures: Effects of Variation of Al2O3 Thickness on Static and Dynamic Magnetic Properties." Rare Metal Materials Engineering **47**(7): 1951-1957.

Ito, S., et al. (2005). "Fe–Co–B/[Ni–Fe/Si] soft magnetic underlayer with high anisotropy field along cross-track direction on disk substrate." Journal of Magnetism Magnetic Materials **287**: 281-286.

Jiang, P., et al. (2021). "Wake-Up Effect in HfO2-Based Ferroelectric Films." Advanced Electronic Materials **7**(1): 2000728.

Jung, H., et al. (2003). "Influence of underlayers on the soft properties of high magnetization FeCo films." Journal of Applied Physics **93**(10): 6462-6464.

Kalinin, S. V., et al. (2018). "Surface-screening mechanisms in ferroelectric thin films and their effect on polarization dynamics and domain structures." Reports on Progress in Physics **81**(3): 036502.

Kaufmann, M. (2006). "Electron Diffraction Studies of Unsupported Antimony Clusters."

Kim, I., et al. (2004). "Effects of boron contents on magnetic properties of Fe-Co-B thin films." IEEE transactions on Magnetics **40**(4): 2706-2708.

Kim, Y. and M. Oliveria (1993). "Magnetic properties of sputtered Fe thin films: Processing and thickness dependence." Journal of Applied Physics **74**(2): 1233-1241.

Klokholm, E. and J. Aboaf (1981). "The saturation magnetostriction of permalloy films." Journal of Applied Physics **52**(3): 2474-2476.

Kneller, E. F. and R. Hawig (1991). "The exchange-spring magnet: a new material principle for permanent magnets." IEEE Transactions on Magnetics **27**(4): 3588-3560.

Kohmoto, O., et al. (2004). "Ferromagnetic resonance in high-resistive soft-magnetic amorphous (CoFeB)–(SiO2) films." Journal of Materials Science Engineering: A **375**: 1069-1071.

Kohn, W. and L. J. Sham (1965). "Self-consistent equations including exchange and correlation effects." Physical Review **140**(4A): A1133.

Kresse, G. and J. Furthmüller (1996). "Efficient iterative schemes for ab initio total-energy calculations using a plane-wave basis set." Physical Review B **54**(16): 11169.

Kuanr, B. K., et al. (2004). "Relaxation in epitaxial Fe films measured by ferromagnetic resonance." Journal of applied physics **95**(11): 6610-6612.

Lafford, T., et al. (1994). "Magnetic, magnetostrictive and structural properties of iron-cobalt/silver multilayers." Journal of Magnetism & Magnetic Materials **132**(1-3): 89-94.

Lee, D., et al. (2009). "Mixed Bloch-Néel-Ising character of 180 ferroelectric domain walls." Physical Review B **80**(6): 060102.

Lee, H.-J., et al. (2020). "Scale-free ferroelectricity induced by flat phonon bands in HfO2." Science **369**(6509): 1343-1347.

Levchenko, S. V. and A. M. Rappe (2008). "Influence of ferroelectric polarization on the equilibrium stoichiometry of lithium niobate (0001) surfaces." Physical Review Letters **100**(25): 256101.

Liang, X., et al. (2018). "Soft magnetism, magnetostriction, and microwave properties of Fe-Ga-C alloy films." IEEE Magnetics Letters **10**: 1-5.

Liu, J., et al. (1998). "High energy products in rapidly annealed nanoscale Fe/Pt multilayers." Applied Physics Letters **72**(4): 483-485.

Lomenzo, P. D., et al. (2015). "TaN interface properties and electric field cycling effects on ferroelectric Si-doped HfO2 thin films." Journal of Applied Physics **117**(13): 134105.

Lou, J., et al. (2007). "Soft magnetism, magnetostriction, and microwave properties of FeGaB thin films." Applied Physics Letters **91**(18): 182504.

Lu-Ran, Z., et al. (2012). "Excellent soft magnetic properties realized in FeCoN thin films." Chinese Physics B **21**(3): 037502.

Lueken, H. (2012). "Superconducting Quantum Interference Device Magnetometry." Methods in Physical Chemistry: 763-795.

Lupu, N., et al. (2008). "Electrochemical deposition of Fe Ga∕Ni Fe magnetic multilayered films and nanowire arrays." Journal of Applied Physics **103**(7): 07B511.

Lyu, J., et al. (2020). "High polarization, endurance and retention in sub-5 nm Hf0.5Zr0.5 O2 films." Nanoscale **12**(20): 11280-11287.

Lyu, X., et al. (2019). Ferroelectric and anti-ferroelectric hafnium zirconium oxide: Scaling limit, switching speed and record high polarization density. 2019 Symposium on VLSI Technology, IEEE.

Materlik, R., et al. (2015). "The origin of ferroelectricity in Hf1− xZrxO2: A computational investigation and a surface energy model." Journal of Applied Physics **117**(13): 134109.

Mayadas, A., et al. (1974). "Resistivity of Permalloy thin films." Journal of Applied Physics **45**(6): 2780-2781.

Migita, S., et al. (2018). "Polarization switching behavior of Hf–Zr–O ferroelectric ultrathin films studied through coercive field characteristics." Japanese Journal of Applied Physics **57**(4S): 04FB01.

Mikolajick, T., et al. (2021). "Next generation ferroelectric materials for semiconductor process integration and their applications." Journal of Applied Physics **129**(10): 100901.

Mittmann, T., et al. (2019). "Origin of ferroelectric phase in undoped HfO2 films deposited by sputtering." Advanced Materials Interfaces **6**(11): 1900042.

Modreanu, M., et al. (2003). Optical characterization of high-k dielectrics HfO 2 thin films obtained by MOCVD. Opto-Ireland 2002: Optics and Photonics Technologies and Applications, International Society for Optics and Photonics.

Muller, J., et al. (2012). "Ferroelectricity in simple binary ZrO2 and HfO2." Nano Letters **12**(8): 4318-4323.

Nguyen, N. V., et al. (2005). "Optical band gaps and composition dependence of hafnium–aluminate thin films grown by atomic layer chemical vapor deposition." Journal of Vacuum Science & Technology A: Vacuum, Surfaces, and Films **23**(6): 1706-1713.

Noguera, C. and J. Goniakowski (2008). "Polarity in oxide ultrathin films." Journal of Physics: Condensed Matter **20**(26): 264003.

Nordlander, J., et al. (2018). "Probing ferroic states in oxide thin films using optical second harmonic generation." Applied Sciences **8**(4): 570.

Nukala, P., et al. (2020). "Guidelines for the stabilization of a polar rhombohedral phase in epitaxial Hf0. 5Zr0. 5O2 thin films." Ferroelectrics **569**(1): 148-163.

Panduranga, M. K., et al. (2018). "Polycrystalline Terfenol-D thin films grown at CMOS compatible temperature." AIP Advances **8**(5): 056404.

Park, M. H., et al. (2018). "Effect of Annealing Ferroelectric HfO2 Thin Films: In Situ, High Temperature X-Ray Diffraction." Advanced Electronic Materials **4**(7): 1800091.

Park, M. H., et al. (2016). "Effect of Zr content on the wake-up effect in Hf1–x Zr x O2 films." ACS Applied Materials & Interfaces **8**(24): 15466-15475.

Park, M. H., et al. (2019). "Thermodynamic and kinetic origins of ferroelectricity in fluorite structure oxides." Advanced Electronic Materials **5**(3): 1800522.

Perdew, J. P., et al. (1996). "Generalized gradient approximation made simple." Physical Review Letters **77**(18): 3865.

Platt, C. L., et al. (2001). "Magnetic and structural properties of FeCoB thin films." IEEE transactions on Magnetics **37**(4): 2302-2304.

Rementer, C. R., et al. (2017). "Tuning static and dynamic properties of FeGa/NiFe heterostructures." Applied Physics Letters **110**(24): 242403.

Rengarajan, S., et al. (1997). "Effect of intermixing on the magnetic properties of Co 50 Fe 50/Ni 80 Fe 20 multilayers." Journal of Applied Physics **81**(8): 4761-4763.

Reuter, K. and M. Scheffler (2001). "Composition, structure, and stability of RuO 2 (110) as a function of oxygen pressure." Physical Review B **65**(3): 035406.

Saidi, W. A., et al. (2014). "Strong reciprocal interaction between polarization and surface stoichiometry in oxide ferroelectrics." Nano letters **14**(11): 6711-6717.

Schenk, T., et al. (2015). "Complex internal bias fields in ferroelectric hafnium oxide." ACS applied materials & interfaces **7**(36): 20224-20233.

Schroeder, U., et al. (2022). "The fundamentals and applications of ferroelectric HfO2." Nature Reviews Materials: 1-17.

Setvin, M., et al. (2018). "Polarity compensation mechanisms on the perovskite surface KTaO3 (001)." Science **359**(6375): 572-575.

Shi, J., et al. (2019). "A study of high piezomagnetic (Fe-Ga/Fe-Ni) multilayers for magnetoelectric device." Journal of Alloys and Compounds **806**: 1465-1468.

Shibayama, S., et al. (2018). "Thermodynamic control of ferroelectric-phase formation in Hf x Zr1− x O2 and ZrO2." Journal of Applied Physics **124**(18): 184101.

Song, C., et al. (2017). "Recent progress in voltage control of magnetism: Materials, mechanisms, and performance." Progress in Materials Science **87**: 33-82.

Stengel, M. (2011). "Electrostatic stability of insulating surfaces: Theory and applications." Physical Review B **84**(20): 205432.

Sun, N. and S. Wang (2002). "Soft magnetism of Fe–Co–N thin films with a Permalloy underlayer." Journal of Applied Physics **92**(3): 1477-1482.

Sun, N., et al. (2000). "Microstructures and Soft Magnetic Properties of High Saturation Magnetization Fe-Co-N alloy Thin Films." MRS Online Proceedings Library Archive **614**.

Sun, N., et al. (2000). "Microstructures and Soft Magnetic Properties of High Saturation Magnetization Fe-Co-N alloy Thin Films." MRS Online Proceedings Library Archive **614**.

Szyjka, T., et al. (2020). "Enhanced ferroelectric polarization in TiN/HfO2/TiN capacitors by interface design." ACS Applied Electronic Materials **2**(10): 3152-3159.

Takakura, W., et al. (2001). "Electrical resistance in Fe/Al2O3 multilayered films prepared by an electron beam evaporation method." Materials Transactions **42**(5): 881-885.

Tasker, P. (1979). "The stability of ionic crystal surfaces." Journal of Physics C: Solid State Physics **12**(22): 4977.

Tian, X., et al. (2018). "Evolution of ferroelectric HfO2 in ultrathin region down to 3 nm." Applied Physics Letters **112**(10): 102902.

Vaz, C. A. (2012). "Electric field control of magnetism in multiferroic heterostructures." J Phys Condens Matter **24**(33): 333201.

Vermeulen, B. F., et al. (2019). "Ferroelectric Control of Magnetism in Ultrathin HfO2\Co\Pt Layers." ACS Applied Materials Interfaces **11**(37): 34385-34393.

Wang, B., et al. (2010). "Effect of fabrication parameters on the microstructure, in-plane anisotropy and magnetostriction of Fe-Ga thin films." Rare Metals **29**(6): 583-588.

Wang, Y., et al. (2010). "Multiferroic magnetoelectric composite nanostructures." NPG Asia Materials **2**(2): 61.

Wang, Z., et al. (2020). "Static and Dynamic Magnetic Properties of FeGa/FeNi (FeNi/FeGa) Bilayer Structures." Coatings **10**(4): 383.

Wei, Y., et al. (2018). "A rhombohedral ferroelectric phase in epitaxially strained Hf 0.5 Zr 0.5 O 2 thin films." Nature Materials **17**(12): 1095-1100.

Woo, J., et al. (2019). "Improved Ferroelectric Switching in Sputtered HfZrO x Device Enabled by High Pressure Annealing." IEEE Electron Device Letters **41**(2): 232-235.

Xing, X., et al. (2011). "RF magnetic properties of FeCoB/Al2O3/FeCoB structure with varied Al2O3 thickness." IEEE Transactions on Magnetics **47**(10): 3104-3107.

Xu, J., et al. (2015). "Electromagnetic and microwave properties of NiFe/NiFeO multilayer thin films." Journal of Materials Science: Materials in Electronics **26**(5): 2931-2936.

Yadav, M., et al. (2021). "High polarization and wake-up free ferroelectric characteristics in ultrathin Hf0. 5Zr0. 5O2 devices by control of oxygen-deficient layer." Nanotechnology.

Yang, Q., et al. (2019). "Magnetoelectric Effect at the Ni/Hf O 2 Interface Induced by Ferroelectric Polarization." Physical Review Applied **12**(2): 024044.

Yu, H., et al. (2002). "Energy gap and band alignment for (HfO 2) x (Al 2 O 3) 1− x on (100) Si." Applied Physics Letters **81**(2): 376-378.

Zhang, B., et al. (2021). "Ferroelectric control of the perpendicular magnetic anisotropy in PtCoRu/Hf0. 5Zr0. 5O2 heterostructure." Applied Physics Letters **119**(2): 022405.

Zhou, D., et al. (2013). "Wake-up effects in Si-doped hafnium oxide ferroelectric thin films." Applied Physics Letters **103**(19): 192904.

Zhu, W., et al. (2002). "Effect of Al inclusion in HfO 2 on the physical and electrical properties of the dielectrics." IEEE Electron Device Letters **23**(11): 649-651.